Università degli Studi di Ferrara

DOCTORAL COURSE IN PHYSICS

CYCLE XXXII

DIRECTOR Prof. Luppi Eleonora

2D materials for room-temperature chemoresistive gas sensing

Scientific/Disciplinary Sector (SDS) FIS/01

Candidate
Valt Matteo

Supervisor
Prof. Guidi Vincenzo

External Supervisor
Prof. Mantovani Fabio

Years 2016/2019

Activity report and list of Pubblications

The research activity carried out by the PhD student involved all the key aspects regarding the study and the realization of solid state devices for gas sensing. The work was mainly devoted to the production of chemoresistive gas sensors based on innovative nanostructures, such as two dimensional materials, and to the deepening of the understanding of the properties of the well-known metal-oxides in diverse field of applications; In parallel with the work presented in this thesis some other project have been followed. In particular, during the first two years of PhD period the research was also dedicated to the development and validation of a technology platform consisting of a hardware for monitoring gaseous emissions, such as Volatile Organic Compounds (VOCs), from the soil-plant-atmosphere system of intensive crops, i.e., tomato and maize, in order to evaluate the water content of these systems. We have analyzed experimental data acquired in-situ by portable sensing units based on metal-oxide gas sensors, thus comparing the results with meteo-sat data and farming operations (e.g. irrigations, rainfalls or pesticide based treatments). The experimentation has proved a dependence of gaseous emissions on the hydric/metabolic status of the plants together with a correlation between sensor signals collected and significant events for the crops. In addition, a contribution was given in developing a micro-electromechanical sensors (MEMS) for gas measurement based on metal oxide semiconductor film using back-end-of-line (BEOL) compatible inter-metal dielectric films deposited by Plasma Enhanced Chemical Vapour Deposition (PECVD). Articles and proceeding published during the PhD alongside with national and international conference contributions are listed to follow.

1. **Journal**:

   (a) A. Gaiardo, B. Fabbri, A. Giberti, G. Zonta, Gherardi, V. Guidi, P. Bellutti, A. Martucci, C. Malagù, M. Sturaro, M. Valt, N. Landini, ZnO and ZnO/Au thin films: room-temperature chemoresistive properties for gas sensing applications, Sensors & Actuators B (doi: 10.1016/j.snb.2016.07.134), 2016.

   (b) M. Valt, B. Fabbri, A. Gaiardo, S. Gherardi, D. Casotti, G. Cruciani, C. Malagù, G. Pepponi, L. Vanzetti, E. Iacob, P. Bellutti and V. Guidi, Aza-crown-ether functionalized graphene oxide for gas sensing and cation trapping applications, Mater. Res. Express (doi: 10.1088/2053-1591/ab11fb), 2019.

   (c) A. Bagolini, A.Gaiardo, M. Crivellari, E. Demenev, R. Bartali, A. Picciotto, M. Valt, V. Guidi, P. Bellutti, Development of MEMS Gas Sensors with CMOS compatible PECVD intermetal passivation, Sensors & Actuators: B. Chemical (doi: 10.1016/j.snb.2019.04.116), 2019.

   (d) B. Fabbri, M. Valt, C. Parretta, S. Gherardi, A. Gaiardo, C. Malagù, F. Mantovani, V.Strati, V. Guidi, Correlation of Gaseous Emissions to Water Stress in Tomato and Maize Crops: from field to laboratory and back. Sensors & Actuators: B. Chemical (https://doi.org/10.1016/j.snb.2019.127227), 2019.

   (e) G.Zonta, M.Astolfi, D. Casotti, G.Cruciani, B.Fabbri, A.Gaiardo, S.Gherardi, V.Guidi, N.Landini, M.Valt, C.Malagù, Reproducibility tests with zinc oxide thick-film sensors, Volume 46, Issue 5, Ceramics International, (https://doi.org/10.1016/j.ceramint.2019.11.178), 2019.

   (f) A. Gaiardo, B. Fabbri, A. Giberti, M. Valt, S. Gherardi, V. Guidi, C. Malagù, P. Bellutti, G. Pepponi, D. Casotti, G. Cruciani, G. Zonta, N. Landini, M. Barozzi, S. Morandi, L. Vanzetti, R. Canteri, M. Della Ciana, A. Migliori, E. Demenev. Tunable formation of nanostructured SiC/SiOC core-shell for selective detection of SO_2. Just accepted on Sensors & Actuators: B. Chemical, 2019.

2. **Proceedings**:

   (a) Gaiardo, A., Bellutti, P., Fabbri, B., Gherardi, S., Giberti, A., Guidi, V., Landini, N., Malagù, C., Pepponi, G., Valt, M., Zonta, G. Chemoresistive Gas Sensor based on SiC Thick Film: Possible Distinctive Sensing Properties between H_2S and SO_2, Procedia Engineering, 168, pp. 276-279 (doi: 10.1016/j.proeng.2016.11.191).

   (b) N. Landini, B. Fabbri, A. Gaiardo, S. Gherardi, V. Guidi, G. Rispoli, M. Valt, G. Zonta, C. Malagù, Detection of Tumor Markers and Cell Metabolites in Cell Cultures, Using Nanostructured Chemoresistive Sensors, AISEM 2017, Lecce (Italy), February 21-23 2017 Lecture Notes in Electrical Engineering 457, 51-58, (doi:10.1007/978-3-319-66802-4_8),

   (c) A. Gaiardo, B. Fabbri, M. Valt, V. Guidi, C. Malagù, P. Bellutti. "Silicon Carbide: a Gas Sensing Material for Selective Detection of SO_2" Proceedings 2017, 1, 745; (doi:10.3390/proceedings1080745).

   (d) M. Valt, B. Fabbri, A. Gaiardo, S. Gherardi, C. Malagù, G. Zonta, N. Landini and V. Guidi, Room Temperature Chemoresistive Gas Sensor Based on Organic-Functionalized Graphene Oxide, Proceedings 2017, 1, 805; (doi:10.3390/proceedings1080805)

   (e) B. Fabbri, M. Valt, V. Strati, A. Gaiardo, F. Mantovani, C. Malagù, S. Gherardi, V. Guidi. "Sustainable Water Management: Sensors for Precision Farming" Proceedings 2017, 1, 780; (doi:10.3390/proceedings1080780)

   (f) A. Gaiardo, B. Fabbri, M. Valt, P. Bellutti, V. Guidi, M. Crivellari, A. Bagolini. "On the Optimization of a MEMS Device for Chemoresistive Gas Sensors" Proceedings 2017, 1, 746; (doi:10.3390/proceedings1080746)

   (g) B. Fabbri, M. Valt, S. Gherardi, A. Gaiardo, C. Malagù, V. Guidi. Soil-Plant-Atmosphere System in Tomato and Maize Crops: Correlation of Gaseous Emissions to Water Stress, Proceedings of the 17th International Meeting on Chemical Sensors (doi: 10.5162/IMCS2018/P1AP.12)

   (h) M. Astolfi, G. Anania, M. Benedusi, S. Gherardi, V. Guidi, N. Landini, C. Palmonari, G. Rispoli, P. Secchiero, V. Tisato, S. Gallo, M. Valt, G. Zonta,

C. Malagù Chemoresistive Sensors for Cancer Pre-Screening in Human Tissue, Proceedings of the 17th International Meeting on Chemical Sensors (doi: 10.5162/IMCS2018/P1DH.7)

(i) A. Gaiardo, P. Bellutti, M. Crivellari, V. Guidi, A. Bagolini, C. Malagu, B. Fabbri, M. Valt Optimization of Silicon and Quartz MEMS Microheater for Chemoresistive Gas Sensors, Proceedings of the 17th International Meeting on Chemical Sensors - IMCS 2018 (doi: 10.5162/IMCS2018/P1MM.5)

(j) A. Gaiardo, B. Fabbri, M. Valt, G. Pepponi, C. Malagù, A. Giberti, P. Bellutti, V. Guidi, Sensing Properties of Nanocrystalline Silicon Carbide in Wet Condition, Proceedings of the 17th International Meeting on Chemical Sensors - IMCS 2018, (doi: 10.5162/IMCS2018/P1NM.18)

(k) B. Fabbri, M. Valt, A. Gaiardo, S. Gherardi, C. Malagù, V. Guidi, Glyphosate detection: an innovative approach by using chemoresistive gas sensors, Proceedings 2018, 2, 910; (doi:10.3390/proceedings2130910)

(l) A. Gaiardo, N. Laidani, H. Ullah, G. Pepponi, M. Fedrizzi, V. Guidi, P. Bellutti, B. Fabbri, C. Malagù, G. Zonta, N. Landini, S. Krik, R. Bartali., F. Marchetti. and M. Valt, A new method to prepare few-layers of nanoclusters decorated graphene: Nb2O5/graphene and its gas sensing properties, Proceedings 2018, 2, 1047; (doi:10.3390/proceedings2131047)

(m) N. Landini, G. Anania, M. Astolfi, B. Fabbri, A. Gaiardo, S. Gherardi, A. Giberti, V. Guidi, G. Rispoli, L. Scagliarini, M. Valt, G. Zonta and C. Malagù, Nanostructured Chemoresistive Sensors for Oncological Screening: Preliminary Study with Single Sensor Approach on Human Blood Samples, Proceedings 2019, 14, 34; (doi:10.3390/proceedings2019014034)

(n) Z. Essalhi, S. Krik, B. Hartiti, A. Gaiardo, A. Lfakir, M. Valt, S. Fadili, B. Fabbri, M. Siadat, V. Guidi and P. Thevenin, Elaboration and Characterization of SnO_2 Doped TiO_2 Gas Sensors Deposited through Dip and Spin Coating Methods, Proceedings 2019, 14, 23; (doi:10.3390/proceedings2019014023)

(o) S. Krik, A. Gaiardo, M. Valt, B. Fabbri, C. Malagù, P. Bellutti and V. Guidi, Influence of Oxygen Vacancies in Gas Sensor Based on Tin Diox-

ide Nanostructure: A First Principles Study, Proceedings 2019, 14, 14; (doi:10.3390/proceedings2019014014)

3. **Oral/poster contribution in conference/workshop**

   (a) A. Gaiardo, A. Giberti, B. Fabbri, V. Guidi, C. Malagù, P. Bellutti, M. Valt, G. Pepponi, S. Gherardi, G. Zonta, N. Landini Silicon Carbide: a Gas Sensing Material for Selective Detection of SO_2, IMCS 2016 (Korea), 10-13 July 2016, presentazione orale (A. Gaiardo)

   (b) A. Gaiardo, B. Fabbri, A. Giberti, G. Zonta, Gherardi, V. Guidi, P. Bellutti, A. Martucci, C. Malagù, M. Sturaro, M. Valt, N. Landini, ZnO vs ZnO/Au thin films: gas sensing properties in photo-activation mode, Convegno Nazionale Sensori 2016 (Roma), 23-25 Febbraio 2016, Oral presentation (A. Gaiardo)

   (c) A. Gaiardo, V. Guidi, P. Bellutti, B. Fabbri, C. Malagù, G. Zonta, S. Gherardi, N. Landini, M. Valt, Silicon Carbide: a Gas Sensing Material for Selective Detection of SO_2, Eurosensors 2016 (Budapest), 4-7 September 2016, poster

   (d) N. Landini, B. Fabbri, A. Gaiardo, S. Gherardi, V. Guidi, C. Malagù, G. Rispoli, M. Valt, G. Zonta. "Detection of tumor markers and cell metabolites in cell cultures using nanostructured chemoresistive sensors" XIX AISEM 2017 (Lecce), 21-23 February 2017, Oral presentation (N. Landini)

   (e) B. Fabbri, V. Guidi, V. Strati, F. Mantovani, A. Gaiardo, M. Valt, C. Malagù, S. Gherardi, G. Zonta, N. Landini. "Hydro-intelligent agroalimentray: sensors for precision farming" XIX AISEM 2017 (Lecce), 21-23 February 2017, Oral presentation (N. Landini)

   (f) A. Gaiardo, A. Giberti, B. Fabbri, V. Guidi, C. Malagù, P. Bellutti, M. Valt, G. Pepponi, S. Gherardi, G. Zonta, N. Landini. "Silicon carbide: a gas sensing material for selective detection of SO_2" XIX AISEM 2017 (Lecce), 21-23 February 2017, Oral presentation (A. Gaiardo)

   (g) M. Valt, A. Gaiardo, B. Fabbri, S. Gheradi, N. Landini, C. Malagù, G. Zonta, P. Bellutti, V. Guidi. "Room temperature chemoresistive gas sensor

based on organic functionalized graphene oxide" XIX AISEM 2017 (Lecce), 21-23 February 2017, poster

(h) M. Valt, A. Gaiardo, B. Fabbri, S. Gheradi, N. Landini, C. Malagù, G. Zonta, P. Bellutti, V. Guidi. "Functionalization of Graphene Oxide for Gas Sensing and Cation Trapping" HYMA 2017 (Lisbona), 6-10 March 2017, poster

(i) V. Guidi, B. Fabbri, A. Gaiardo, M. Valt, C. Malagù, S. Gherardi, G. Zonta, N. Landini. "Gas sensing via chemoresistive effect in nanostructured semiconductors" XXXVI DyProSo 2017 (Cracovia), 27-31 August 2017, Invited oral presentation (V. Guidi)

(j) M. Valt, A. Gaiardo, B. Fabbri, S. Gheradi, N. Landini, C. Malagù, G. Zonta, P. Bellutti, V. Guidi. "Room Temperature Chemoresistive Gas Sensor Based on Organic-Functionalized Graphene Oxide" I3S 2017 (Barcellona), 27-29 September 2017, Oral presentation (M. Valt)

(k) A. Gaiardo, B. Fabbri, M. Valt, V. Guidi, C. Malagù, P. Bellutti. "Silicon Carbide: a Gas Sensing Material for Selective Detection of SO_2" I3S 2017 (Barcelona), 27-29 September 2017, Oral presentation (A. Gaiardo)

(l) B. Fabbri, M. Valt, V. Strati, A. Gaiardo, F. Mantovani, C. Malagù, S. Gherardi, V. Guidi. "Sustainable Water Management: Sensors for Precision Farming", I3S 2017 (Barcellona), 27-29 September 2017, poster

(m) A. Gaiardo, B. Fabbri, M. Valt, P. Bellutti, V. Guidi, M. Crivellari, A. Bagolini. "On the Optimization of a MEMS Device for Chemoresistive Gas Sensors" I3S 2017 (Barcellona), 27-29 September 2017, poster

(n) Fabbri, V. Guidi, V. Strati, F. Mantovani, A. Gaiardo, M. Valt, C. Malagù, S. Gherardi, Sustainable Water Management through Crops Growth Monitoring, Labirinto d'acque 2018 (Parma), 21 March 2018, Oral presentation (B. Fabbri)

(o) B. Fabbri, M. Valt, S. Gherardi, A. Gaiardo, C. Malagù, V. Guidi. Soil-Plant-Atmosphere System in Tomato and Maize Crops: Correlation of Gaseous Emissions to Water Stress, 17th International Meeting on Chemical Sensors - IMCS 2018 (Wien) 15-19 July 2018, poster

(p) M. Astolfi, G. Anania, M. Benedusi, S. Gherardi, V. Guidi, N. Landini, C. Palmonari, G. Rispoli, P. Secchiero, V. Tisato, S. Gallo, M. Valt, G. Zonta, C. Malagù Chemoresistive Sensors for Cancer Pre-Screening in Human Tissue, 17th International Meeting on Chemical Sensors - IMCS 2018 (Wien) 15-19 July 2018, poster

(q) A. Gaiardo, P. Bellutti, M. Crivellari, V. Guidi, A. Bagolini, C. Malagù, B. Fabbri, M. Valt Optimization of Silicon and Quartz MEMS Microheater for Chemoresistive Gas Sensors, 17th International Meeting on Chemical Sensors - IMCS 2018 (Vienna), 15-19 July 2018, poster

(r) A. Gaiardo, B. Fabbri, M. Valt, G. Pepponi, C. Malagù, A. Giberti, P. Bellutti, V. Guidi, Sensing Properties of Nanocrystalline Silicon Carbide in Wet Condition, 17th International Meeting on Chemical Sensors - IMCS 2018, (Wien) 15-19 July 2018, poster

(s) A. Gaiardo, N. Laidani, H. Ullah, G. Pepponi, M. Fedrizzi, V. Guidi, P. Bellutti, B. Fabbri, C. Malagù, G. Zonta, N. Landini, S. Krik, R. Bartali., Francesca Marchetti. and M. Valt, A new Nb_2O_5/graphene and its gas sensing properties, Eurosensor 2018 (Graz) 9-12 September 2018, poster

(t) B. Fabbri, M. Valt, A. Gaiardo, S. Gherardi, C. Malagù, V. Guidi, Glyphosate detection: an innovative approach by using chemoresistive gas sensors, Eurosensor 2018 (Graz), 9-12 September 2018, poster

(u) M. Valt, B. Fabbri, A. Gaiardo, S. Gherardi, D. Casotti, G. Cruciani, C. Malagù, G. Pepponi, L. Vanzetti, E. Iacob, P. Bellutti and V. Guidi, Aza-crown ether functionalized graphene oxide as multifunctional material for gas sensing and cation trapping, Italian National Conference on Materials Science and Technology Bologna, 22-26 October 2018, Oral presentation (M. Valt)

(v) V. Guidi, M. Valt, B. Fabbri, A. Gaiardo "Graphene-based composites for gas sensing and cation trapping applications" EMRS Spring meeting 2019, 29 May 2019 Nice, presentazione orale su invito (V. Guidi)

(w) N. Landini, G. Anania, M. Astolfi, B. Fabbri, A. Gaiardo, S. Gherardi, A. Giberti, V. Guidi, G. Rispoli, L. Scagliarini, M. Valt, G. Zonta and C. Malagù, Nanostructured Chemoresistive Sensors for Oncological Screening:

Preliminary Study with Single Sensor Approach on Human Blood Samples, 8th GOSPEL Workshop. Gas sensors based on semiconducting metal oxides: basic understanding & application fields, 20-21 June, 2019, Ferrara, Poster

(x) Z. Essalhi, S. Krik, B. Hartiti, A. Gaiardo, A. Lfakir, M. Valt, S. Fadili, B. Fabbri, M. Siadat, V. Guidi and P. Thevenin, Elaboration and Characterization of SnO_2 Doped TiO_2 Gas Sensors Deposited through Dip and Spin Coating Methods, 8th GOSPEL Workshop. Gas sensors based on semiconducting metal oxides: basic understanding & application fields, 20-21 June 2019, Ferrara, poster

(y) S. Krik, A. Gaiardo, M. Valt, B. Fabbri, C. Malagù, P. Bellutti and V. Guidi, Influence of Oxygen Vacancies in Gas Sensors Based on Tin Dioxide Nanostructure: A First Principles Study, 8th GOSPEL Workshop. Gas sensors based on semiconducting metal oxides: basic understanding & application fields, 20-21 June 2019, Ferrara, poster

(z) M. Caporali, M. Valt, B. Fabbri, A. Gaiardo, C. Malagù, M. Serrano-Ruiz, V. Guidi, M. Peruzzini, Nickel-decorated black phosphorus for sub-ppm NO_2 detection at room temperature, 8th GOSPEL Workshop. Gas sensors based on semiconducting metal oxides: basic understanding & application fields, 20-21 June 2019, Ferrara, poster

Introduction

In 1938, Wagner and Hauffe discovered that atoms and molecules adsorbed onto the surface of a semiconductor influences its electrical properties (1). Brattain and Bardeen have extended this knowledge with their study about germanium properties when exposed to electrolytes and gaseous molecules (2). Afterwards, studies provided by Heiland (3), Bielanski et al. (4) and Seiyama et al. (5) about reaction effects between metal oxides and gaseous analytes, laid the basis to a possible development of a commercial device. Thus, the decisive step was taken when Taguchi introduced chemoresistive sensors based on metal-oxide semiconductors in an industrial product (Sajama-Taguchi sensors (6)). From then on, research about chemoresistive sensors and, more generally, solid-state gas sensors has been increased. This growing interest has been enhanced by an increased awareness about substances that are hazardous to health resulting in pollution (7). Indeed, in the last years, air pollution has revealed to be a major concern caused by many inhaled substances that are known to have adverse effects on our long-term health. The known effects of air pollution have further highlighted hazards in industrial environments (e.g. mining, chemical and manufacturing industries) and in urban/domestic environments (8), which has led to extensive research to determine the recommended safe levels of known airborne hazardous substances (9). Legislation has implemented some important constrains regarding industrial activities introducing gas exposure parameters, such as Threshold Limit Value (TLV) and Short-Term Exposure Limit (STEL) as law references for human safety (10). Hence, there has been a sudden growth in the number of applications requiring accurate detection of a wide variety of gases and vapours. In many cases, suitable methods to control or monitor these atmospheres were limited by sensor technology or high costs of analysis methods. For this reason, companies and researchers paid special attention about chemoresistive gas sensors and their peculiar advantages, such as very low detection limit (in the range

of ppb-ppm of gas concentrations), low manufacturing costs, small size and simple implementation on portable devices (11). These advantages allowed chemoresistive gas sensors to get a market share, despite the existing higher performance sensors such as optical sensors, which, anyway, are very expensive, bulky and technologically complex. Nowadays, there are many companies offering this type of sensors, such as Figaro, FIS, MICS, UST, CityTech, AppliedSensors, NewCosmos, Alphasense, Sensirion etc. (12). Over the years, the chemoresistive gas sensor technology focused mainly on the development of devices provided with a Metal OXides (MOX) semiconductors as receptor/sensing material and alumina substrates as mechanical support. Indeed, this coupling allows to develop sensors with excellent properties, i.e. high sensitivity, fast response and recovery time, robustness, easy and relatively low-cost production (13, 14). The research about chemoresistive gas sensors allowed broadening knowledge of the capabilities of these devices, thus leading to an increase of their properties control and a refinement of the production process. Moreover, the ever-greater awareness of the sensing worth of these devices allowed the development of increasingly technologically advanced systems, such as the electronic nose, which let extended application fields of the chemoresistive gas sensors from the environmental monitoring, to safety and security, quality control of food production and medical diagnosis (15, 16, 17). However, despite such great advantages, the in-depth study of these devices has highlighted some important unsolved drawbacks that still limit their use in many application fields. Among these disadvantages, the incomplete selectivity and lack of stability sometimes result in unreliable responses (18, 19). Moreover, these devices often need a significant amount of energy to support chemical reactions at the MOX surface, activated at high temperatures (20).

The need to overcome these limits give us the opportunity to expand knowledge on chemoresistive gas sensors and to explore new frontiers about technological development of this device, introducing studies about new kind of substrates and sensing materials. In this sense, two-dimensional (2D) materials have attracted great scientific attention due to their unusual and fascinating properties for use in electronics, spintronics, photovoltaics and medicine. Graphene, transition metal dichalcogenides (TMD), phosphorene, etc., have shown great promise for gas sensing applications due to their tunable band gap, high surface-to-volume ratio, room temperature operations (RT), low noise and sensitivity of electronic properties to the changes in the surroundings.

The aim of this thesis is to contribute to the innovation of chemoresistive gas sensors with the employment of novel 2D materials. Different approaches are exploited to face the challenge, including studies of not conventional semiconductors sensing materials such as graphene, graphene oxide and exfoliated black phosphorous analysing their performance as pristine material and as a starting point for the synthesis of new nanocomposites in conjunction with different classes of chemical compounds like metals, metal oxides and organic functional groups.

An introduction to the generalities of 2D materials, including the gas-sensing mechanisms known so far and a description of their operational principles, as well as the main factors influencing their performance, are given in Chapter 1. Moreover, advantages in using 2D materials instead of traditionally employed MOX semiconductors as chemoresistive gas sensing materials are explained.

In Chapter 2 materials and methods employed for chemical, structural, morphological characterization of prepared 2D materials are reported. Afterwards, electrical characterization at RT of sensing materials used are showed and discussed.

Graphene and Graphene Oxide based sensing films are presented in Chapter 3 with materials and electrical characterizations of Niobium doped Graphene and aza-crown ethers functionalized graphene oxide.

In Chapter 4 Nickel decorated black Phosphorus is introduced as potential candidate for sensing NO_2 at RT. After a brief introduction, material and electrical characterization are described.

The main conclusions of every single study are presented, as well as the outlooks for future projects, are summarized in the last chapter, Conclusions and Outlook.

Contents

Chapter 1

2D materials in gas sensing

1.1 State of the art

An atom-thick layer of sp^2 carbon atoms, named graphene, was firstly conceptualized in 1947 (21) and synthesized in 2004 (22). Its outstanding morphological characteristics and its excellence electronic properties such as zero band-gap, high room-temperature carrier mobility (200,000 $cm^2V^{-1}s^{-1}$), a high carrier density of $\sim 10^{12}$ cm^{-2}, and it has low resistivity at room temperature immediately attract the attention of the researchers worldwide (23, 24, 25). A small concentration of gas adsorption on a graphene sheet can cause a sensible change in resistance, which suggested its use as sensitive material for various gas detection applications. Therefore, graphene, graphene oxide (GO), reduced graphene oxide (rGO), and their functionalized materials have been widely used for gas-sensing applications.

The easy exfoliation routes to obtain graphene sheets leads to the wide use for fabrication of gas sensing devices. Recently, the layered inorganic analogues of graphene, such as transition metal dichalcogenides (TMDs) including MoS_2, WS_2, $MoSe_2$, WSe_2, ReS_2, and $ReSe_2$, as well as layered metal oxides (MoO_3 and SnO_2), layered group III–VI semiconductors (GaS, GaSe, and SnS_2), phosphorene, h-BN, etc., have also attracted attention due to their thickness-dependent physical and chemical properties.

Their 3D counterparts of the aforementioned materials are formed by many layers, weakly bonded by van der Waals forces, allowing an easy mechanical or wet chemical exfoliation. The 2D materials field is now one of the main topic in the material science, physics of matter, chemical engineering and sensing.

In Figure 1.1, the number of published papers with the word "graphene oxide", "MoS_2", WS_2" and "phosphorene" or "exfoliated black phosphorus" is reported. In the last decade, it can be observed a dramatic increase of interest.

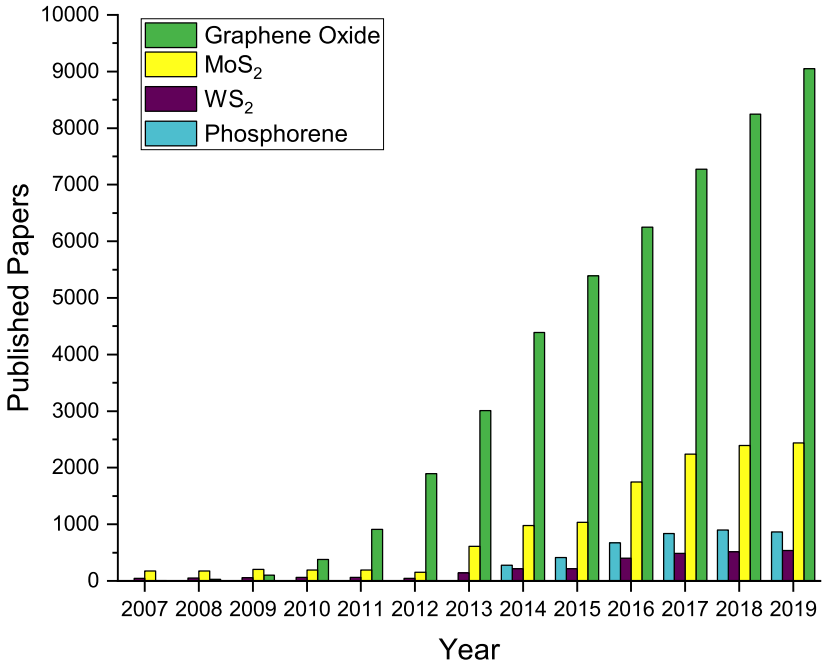

Figure 1.1: Number of published papers vs. year of publication for "graphene oxide", "MoS_2", "WS_2" and "phosphorene" or "exfoliated black phosphorus". (Source: Scopus, November 2019).

Due to their morphological properties, 2D materials appear soon as promising candidates for gas sensors, having an intrinsically high surface-to-volume ratio. In addition to having a large surface- to-volume ratio like graphene, these layered inorganic analogues also have semiconducting properties with an appropriate band gap, which is attractive for modulating the transport characteristics to enhance the sensing performance (26).

Graphene oxide has been the first graphene-like 2D material investigated and the research on its gas sensing properties and performances had a tremendous increase in the last years.

1.2 Chemoresistors

Chemoresistor constitutes one of the most investigated gas sensing devices; its operating mechanism is that the gas molecules adsorbed on the surfaces of the gas sensing material induce a change of its electrical conductance, and by measuring this conductance change, the sensitive gases can be effectively detected. Chemoresistors have their own advantages, such as simplicity of operation and fabrication, low cost and power consumption, ability to reuse and also offer advances in miniaturization (27). The sensitive layer is deposited between two or more interdigitated metal electrodes on an insulating substrate (alumina, silicon dioxide, quartz, etc.) Figure 1.2. supported by an inert substrate and two metallic electrodes or interdigitated electrodes. These sensors are widely used also for metal oxide semiconductors based layers, which need high operating temperatures to operate , therefore many chemoresistors are equipped with a heater (usually a metal coil exploiting the Joule's effect) or the sensing layers are deposited on a micro-hot plate to heat the device up to the optimal operating temperature.

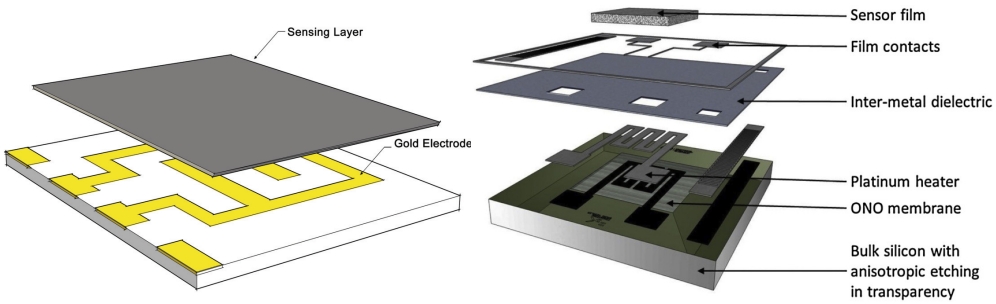

Figure 1.2: Schematic representation of alumina (left) and silicon (right) substrates produced respectively at University of Ferrara and Bruno Kessler Foundation in Trento, silicon substrates figure reprinted with permission from (28).

1.3 Gas-sensing mechanisms

1.3.1 Surface adsorbed oxygen ions mechanism

In conventional metal oxide based gas sensors (ZnO, SnO_2, etc.), the sensing mechanism is related to their surface adsorbed oxygen ions. In the normal operating temperature range (200 °C - 500 °C), oxygen negative ions such as are adsorbed on the surface of metal oxides, charging them negatively (29). Various gases adsorbing on metal oxides will interact with the oxygen negative ions, and change the conductivity of the metal oxides. After exposing to a reducing gas, it releases a negative charge due to the oxidation, increasing the conductivity of metal oxides. Taking reducing CO as an example (30).

$$\mathrm{CO\,(g) + O^-(ads) \longrightarrow CO_2(g) + e^-}$$

$$\mathrm{CO + 2\,O^- \longrightarrow {CO_3}^{2-} + e^- \longrightarrow CO_2 + \tfrac{1}{2}\,O_2 + 2\,e^-}$$

If an electron-accepted gas is present, it will accept the charge, which decreases the conductivity of metal oxides. For example,

$$\mathrm{NO_2(ads) + e^- \longrightarrow {NO_2}^-(ads)}$$

1.3.2 Charge transfer mechanism

The gas sensing mechanism of 2D layered inorganic analogues of graphene is mainly based on the charge transfer processes, in which the sensing materials act as acceptors or donors for charge carrier. When exposing to target gases, the charge transfer reaction occurs between the materials and adsorbed gases at surface, accompanied by different transfer directions and quantities of charges, which leads to a change in conductance of the material. If the sensing materials are re-exposed to air, desorption of gas molecules can occur, causing the sensing MoS_2, and the adsorbed gas molecules include O_2, H_2O, NH_3, NO, NO_2, CO, etc. shows the charge density difference images for the aforementioned gases interacting with monolayer MoS_2, the red region represents the charge accumulation, while the green region is the charge depletion. (32)

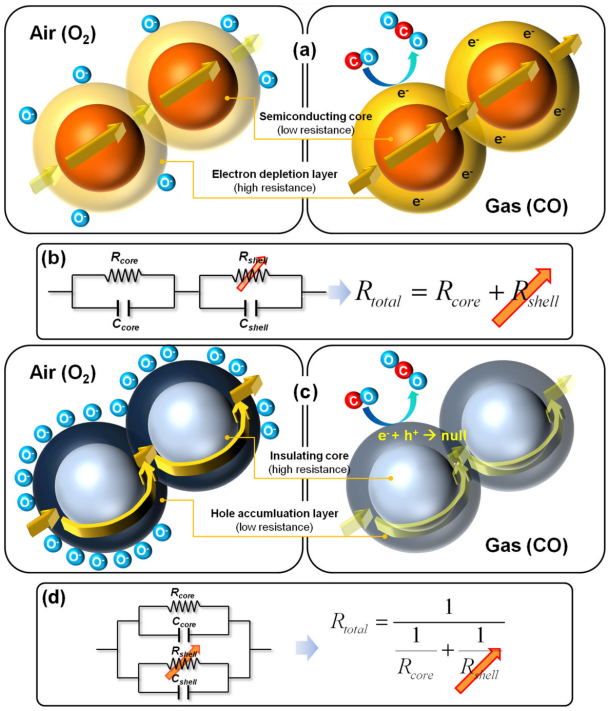

Figure 1.3: Schematic representation of the gas sensing mechanisms of (a and b) n-type MOX and (c and d) p-type MOX. Reprinted with permission from (31). Copyright 2014 Elsevier.

1.4 Advantages of Two-Dimensional Materials for Gas Sensing

Two-dimensional materials, other than graphene, have a band gap that can be tunable by thickness, which makes them ideal channel materials for sensing. Capabilities of sensitive material such as high carrier mobility and high on/off ratio are also important for the implementation of gas sensors. The number of layers of the two-dimensional material is directly associated with the stability and it is inversely proportional to the response time. The main gas sensing mechanism is the charge transfer reaction between the gaseous species and the two-dimensional material. Other advantages that two-dimensional materials offer in gas sensing are higher thermal stability and wider operation temperature range.

2D nanostructures can provide some additional advantages including more active sites, facile surface functionalization, good compatibility with device integration, pos-

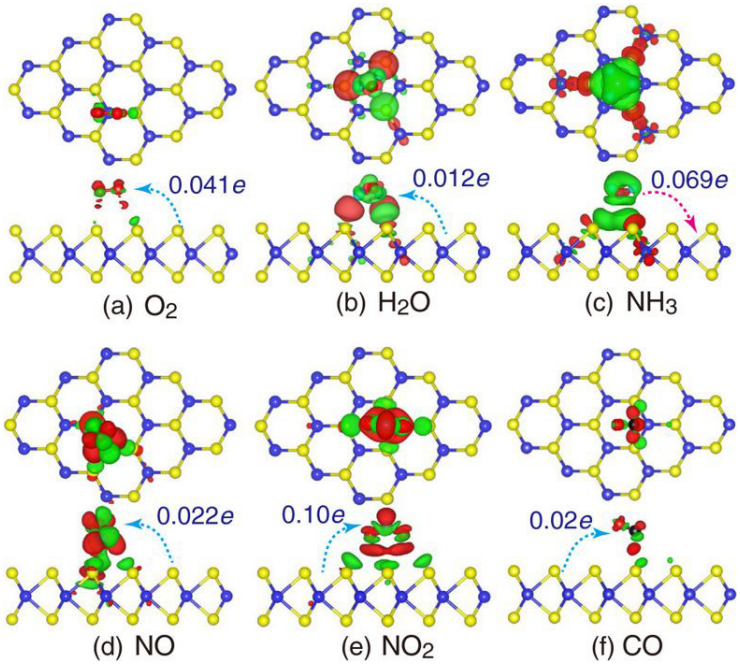

Figure 1.4: Charge transfer process and density difference plots for (a) O_2, (b) H_2O, (c) NH_3, (d) NO, (e) NO_2, and (f) CO interacting with monolayer MoS_2. Reproduced with permission from Yue et al., Nanoscale Res. Lett. 8, 425 (2013). licensee Springer. 2013.

sibility to be assembled into 3D architectures, etc. which are critically important for developing high performance gas sensors. Further, hybrid structures based on two-dimensional materials can be designed to optimize the performance of the gas sensors. Gas sensors based on heterostructures overcome the inherent disadvantages of gas sensors based on simple materials such as poor selectivity and insensitivity to the low concentration of the gas to be detected. Moreover, 2D materials can be easily fabricated as chemoresistive field effect transistors (FETs) that consume less power and offer good safety. Thanks to these last capabilities, the two-dimensional materials are distinguished from conventional metal oxides in that they offer an excessively sensitive platform and ideal for portable applications due to the reduced power consumption.

1.5 Factors Influencing the Gas Sensing Characteristics of 2D Nanostructures

The performance parameters of gas sensors can be influenced by several factors, such as properties of sensing materials, working temperature, humidity, gas flow rate, length-to width of sensing materials, etc. Temperature is an important factor for gas sensors. For example, some chemoresistor gas sensors usually operate at temperatures higher than 200°C, which accelerates the adsorption/desorption processes of gases and increases reactivity between sensing materials and gaseous molecules. However, work capability of gas sensors at lower or room temperatures is required in some applications, such as explosive and harsh environments. These room-temperature sensors do not need a heater and can be easily integrated into other structures to realize low-cost sensing units. Thus, it is important to find a way to reduce the operating temperature of gas sensors. Humidity is another important factor influencing the performance of gas sensors. The sensitivity of gas sensors will be significantly affected in the presence of water vapours, complicating the detection of target gases under exposure to high levels of water vapour. Therefore, minimizing the impact of humidity is a key aim in developing gas sensors. It is important to design gas sensors which have very low response to water vapour, such as water-insensitive chemoresistors. Alternatively, when the humidity levels are not determined, an ambient air can be chosen as a reference, or if the level is relatively constant, some solutions can be used to remove humidity (33).

The total flow rate also has a significant effect on the sensing performances of sensors to target gases. For example, Zhou et al. investigated the gas-sensing mechanism of chemoresistors based on rGO which was airbrushed onto interdigital electrodes. The sensitive performances of rGO chemoresistors showed that the total flow rate had a significant effect on their initial electric resistance and their sensing responses to target gases. The electric resistance of the rGO film decreased at a larger total flow rate and increased at smaller one (34).

In gas sensing applications, dimensionality of the nanostructure undoubtedly plays a key role for efficient monitoring. Many factors associated with the general characteristics of thin 2D nanostructures. are responsible for this. The ultrahigh thickness and its very high associated surface area is one of the most important factors that helps to enhance the gas sensing performance of thin 2D nanostructures (Figure 1.5).

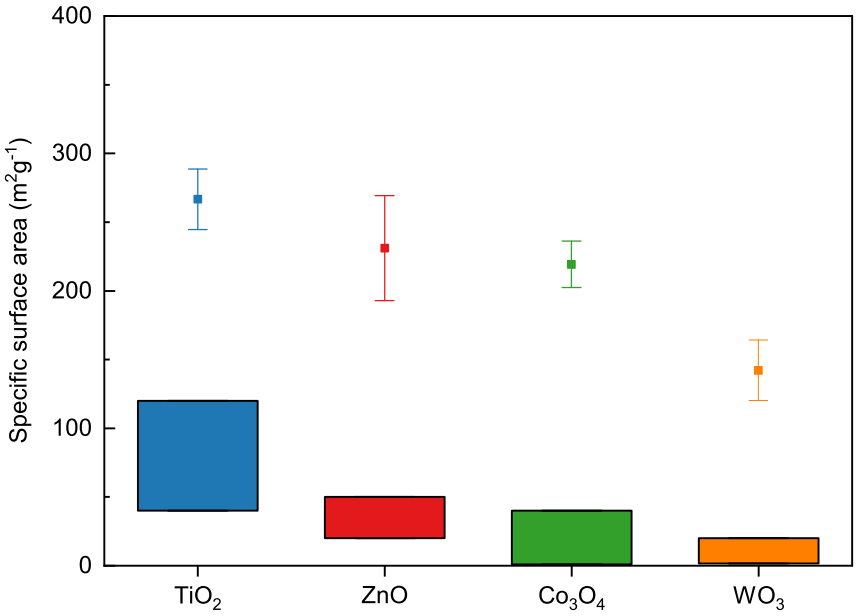

Figure 1.5: Specific surface areas of 2D metal oxide nanosheets. Specific surface areas of the 2D metal oxide nanosheets (individual symbols with error bars) together with the reported specific surface areas (individual bars with numbers) of the conventional metal oxide nanoparticles.

The high surface area makes them highly sensitive to the adsorption of gaseous molecules on the surface (35). In the case of monolayer 2D nanostructures, the whole surface is theoretically exposed to the gas influence and it is potentially promising for ultra-high sensitivities. Furthermore, on their surfaces, the atoms are unsaturated due to the lower coordination number. Because the adsorption of gaseous species on solid surfaces usually occurs on the low coordinated steps, edges, terraces, kinks, and corner atoms, the number of chemisorbed gaseous molecules will be high. In the atomically-thin two-dimensional sheets, owing to their high fraction of these sites with highly reactive sites, an improvement of the sensing performance can be expected with respect to their higher dimensional material counterparts (36). The sensing properties of thin 2D-sheets of inorganic materials derive also from their unique electronic structures. It is expected that the electrical properties of these materials differ substantially from

that of their bulk counterparts. The essential factors of a material for gas sensing applications include high charge carrier mobility, high conductivity, and a suitable band gap energy. Compared to graphene, which has high charge carrier mobility and conductivity but presents some limitations because of the lack of an intrinsic band gap, thin 2D inorganic layered materials appear to be the most promising due to an appropriate band gap (Figure 1.6).

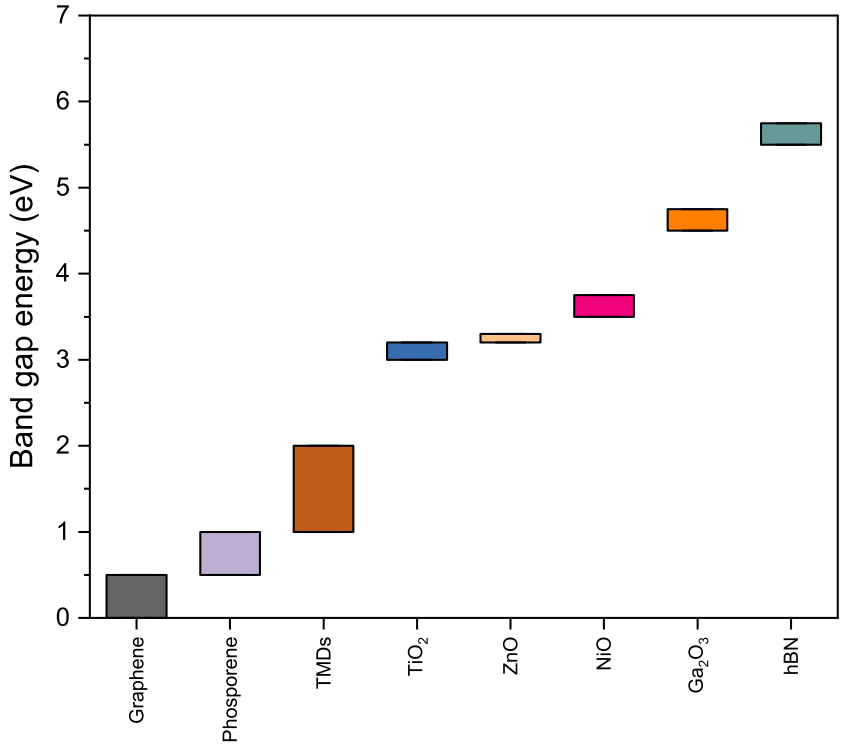

Figure 1.6: Intrinsic band gap of graphene-like thin 2D inorganic layered materials. Comparing all these 2D materials, it can be noted that graphene is characterized by zero intrinsic band gap energy, whereas regarding the other thin 2D inorganic layered materials of interest for gas sensing (TMDs and MOX), they exhibit an increasing band gap going from TDMs to MOX.

Interestingly, the band gap can be modulated by tuning the layer numbers. As an example, referring to bulk and few- to mono-layer MoS_2, a group 6 TMDs with a trigonal prismatic structure, the bulk material is an indirect-gap semiconductor having a band gap of $\approx$1 eV. In contrast, an isolated monolayer of the same material is a direct-

gap semiconductor. In addition, there is an indirect-to-direct band gap transition going from a bulk to a monolayer material which arises from quantum confinement effects, as probed by high photoluminescence in the monolayers of MoS_2, whereas only a weak emission is observed in the multilayered form. In general, in the case of group 6 TMDs, the monolayer band gap is typically 50% larger than that of the bulk materials (37). Thus, the electrical characteristics of practical gas conductometric sensors can be tuned up by the appropriate modulation of the number/thickness of the two-dimensional sensing layer.

Furthermore, by examining the electronic structures of such thin 2D materials, such as the density of states (DOS), important information can be acquired which is essential to understand their intrinsic charge transporting characteristics. It has been demonstrated that changes in interlayer coupling, the degree of quantum confinement, and symmetry elements lead to dramatic differences in the electronic structure of single-layer materials, i.e., increases at the valence band edge with respect to the bulk material (38). The electronic structure of single-layer material is furthermore strongly influenced by adsorbed species.

1.6 Electronic Band Structure for 2D Materials

The electrical properties of a solid are determined basically through its electronic band structure, which establishes the range of energy states that electrons may or may not have within their crystalline structure. The allowed electronic states are represented by the valence band (states within the atom) and the conduction band (stable states with freedom of movement). Between the valence band and the conducting band, there is a set of electronic states that are not allowed or prohibited for electrons, since these are intermediate and unstable. The electronic band theory predicts these bands by solving the Schrödinger equation for a periodic crystal structure making use of the quantum mechanical wave functions or Bloch functions of the electrons. Particularly, solid state devices based on semiconductor materials owe their electronic behaviour to the exploitation of these electronic bands. A summary describing the design process of a gas sensor through the electrical properties of the sensing material is illustrated in Figure 1.7

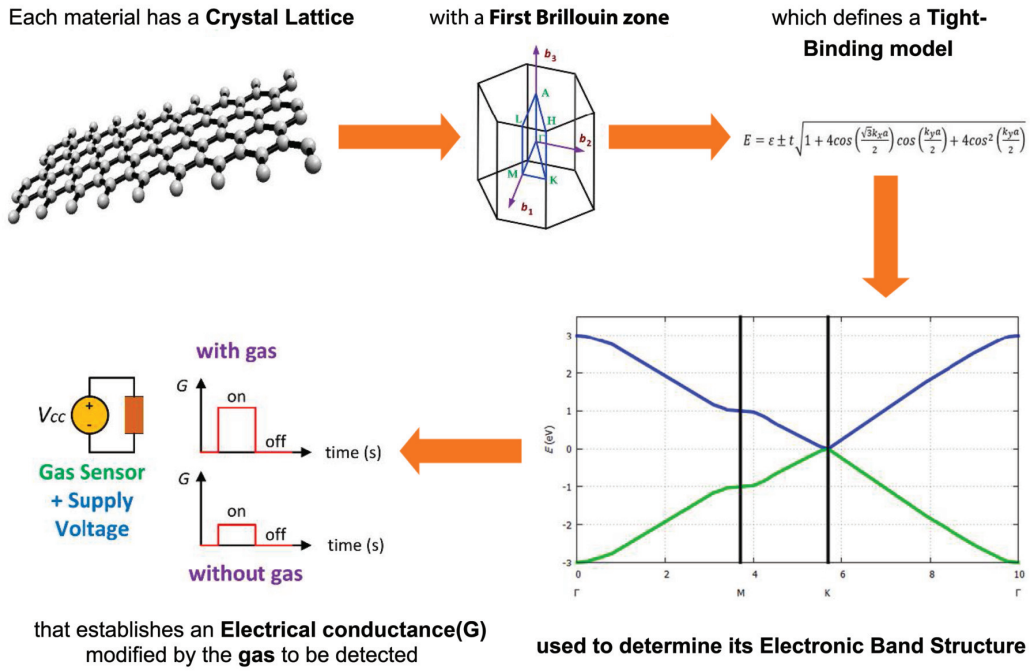

Figure 1.7: Design process of a gas sensor through the electrical properties.

The solution of the Schrödinger equation, in addition to describing the changes in the time of the behaviour of electrons, also relates the state vector of its quantum system (ψ), its position vector (r), and the periodicity function of the crystal (u). This can be mathematically expressed as:

$$\psi_{nk}(r) = e^{ikr} u_{nk}(r)$$

where k is called the wave vector and n represents a band index. Therefore, its multiple solutions $E_n(k)$ represent the n energy bands evaluated for each wave vector k that establish the energy dispersion relationships of the electrons in the crystal lattice. According to the crystalline establishes the states within the electronic band structure.

1.7 Correlation between Gas Sensing Characteristics and Electronic Band Structure

Since the selectivity of a gas sensor is related to its ability to respond to a gas in the presence of others, then the design of a gas sensor implies that the gas to be detected

must be adsorbed by the sensing material, exclusively, and this is achieved, if the necessary catalysts are added to this material. The catalytic materials must be based on metallic nanoparticles. These materials modify the band gap and, in this way, only those gases with ionization energy like the band can be adsorbed. The adsorption energy (E_a) of the gases is calculated using the following mathematical expression (39):

$$E_a = E_{sensing\ material+gas} - (E_{sensing\ material} + E_{gas})$$

where $E_{sensing\ material+gas}$ implies the total energy of the system formed by the sensing material and the sensed gas. On the other hand, $E_{sensing\ material}$ and E_{gas} represent the punctual energy of the two-dimensional material based system and gas molecules, respectively. Since the sensitivity of a gas sensor expresses the change in the output signal per unit gas concentration, it is necessary to design a material capable of detecting levels up to below parts per billion of gas present in the sensing material. Two-dimensional materials have a high sensitivity due to their high surface-to-volume ratio and their semiconductor properties. Both the dimensions of the sensing material and the semiconductor properties of the material can be tuned; in this way, the sensitivity of a gas sensor based on two-dimensional materials can be designed. The band gap of the sensing material plays a major role in adjusting the sensitivity of the gas sensor. Besides, the doped two-dimensional materials show higher selectivity and sensitivity toward gas molecules compared to pure two-dimensional materials (39). The sensitivity and selectivity of a semiconductor two-dimensional material based gas sensor depend on any change in its electronic properties. Another of the important performance parameters of gas sensors is reversibility, which implies that the sensor must be capable of being used during a cyclic operation without qualitatively or quantitatively modifying its response to the target gas (40). This is committed to selectivity, since when the latter is high; the reversibility is low due to the high bond energies involved. Therefore, complete reversibility is achieved when weak interactions between the gas and the sensing material are present (41). Then, a two-dimensional material with a band gap without catalysts may have better reversibility. This can be appreciated when there are no intermediate bands or levels between the valence band and the conduction band. Gas sensors require a response time to react to the presence of the target gas whose concentration changes from zero to a certain concentration value (40). This response time is directly related to the type of band gap that the two-dimensional material has,

since being a direct band gap would be expected to have a shorter response time than a material with an indirect band gap. Although the path between the valence band and the conduction band that the electron should travel energetically was straight, the magnitude of the band gap should be short to reduce the response time. A small response time is directly associated with a high sensitivity of the gas sensor, which is linked to a reduced band gap (42). In any physicochemical process such as gas sensing, stability represents the ability of the sensor to keep reproducible its performance, in a specific period of time, before various physicochemical variables (40). Since gas sensors are susceptible to being modified by various variables such as temperature, then the band gap of the two-dimensional material must remain stable before any event presented. Some gas molecules in contact with the sensing material tend to dissociate and chemically absorb into it. Other gases tend to be physically absorbed stably on the sensing material, which leads to different interaction strengths. These latter molecules induce different modifications in the forbidden band of the material, which can be observed in the energy band diagram (43). Key performance scores for gas sensors based on two-dimensional materials are illustrated in Figure 1.8.

1.8 Sensitization

The effects that cause increased sensor response are often grouped into two categories: electronic sensitization and chemical sensitization. In electronic sensitization, the charge carrier concentration is altered this modifies the position of the Fermi level. In chemical sensitization, gas adsorption and dissociation onto the sensor surface is enhanced. These concepts are closely linked, and they may both happen simultaneously. Both doping and heterojunctions from noble metals and transition metals can cause these effects. Understanding how these sensitization processes cause resistance modulation requires knowledge on charge transfer in semiconducting materials because charge transfer occurs between the sensor and analyte gas as well as across a heterojunction. A concept known as “Debye length” is used to describe charge transfer depth and indicates how this charge redistribution might affect sensing.

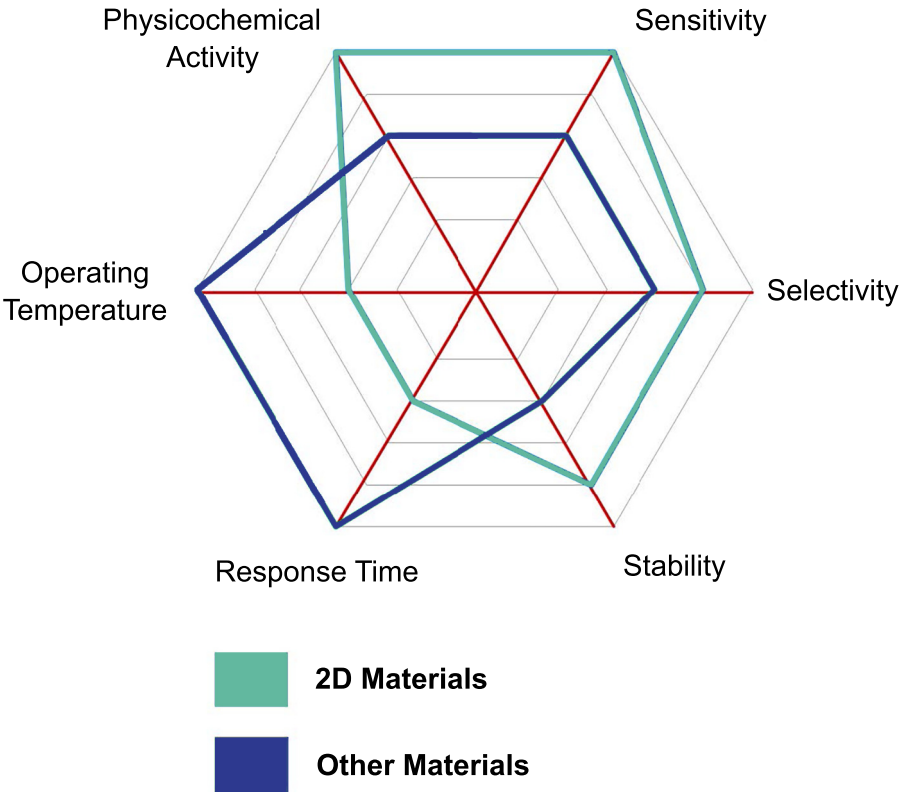

Figure 1.8: Key performance scores spider chart comparing the performance of gas sensors based on 2D materials and those based on other materials.

1.8.1 Debye length

When materials with different Fermi levels are in contact, electrons will transfer from the material with the higher Fermi level to the material with the lower Fermi level. This process will create a net positive charge in the material that has lost electrons and a net negative charge in the material that has gained electrons. The electron transfer will continue until the negative charge buildup raises the energy of the electrons to prevent further electron transfer. This process is what controls Fermi level equilibration. The ability of a material to hold the resulting electric field depends on the carrier concentration. When a material contains a large number of mobile charge carriers, these will move to balance electrostatic charges in the material. Therefore, the penetration depth of this charge gradient will be inversely related to the number of charge carriers because mobile electrons will move to areas with positive charge and vice versa for holes. In covalent semiconductors, such as silicon and germanium, donors and accep-

tors are added to increases the concentration of electrons and holes, respectively. In oxide semiconductors, dopants can also be added to increase the carrier concentration. However, oxygen vacancies and cation vacancies are the primary source of conducting electrons and holes. The Debye length is a property that indicates the penetration depth of charge carrier redistribution. The Debye length may be calculated as follows.

$$L_D = \sqrt{\frac{\varepsilon kT}{q^2 N_d}}$$

As shown in the above equation, the Debye length varies directly with a material's dielectric constant, ε, and temperature and varies inversely with the number of mobile carriers. The dielectric constant of a material describes how well charge separation can occur in a given material. For this reason, the Debye length will increase as a material's ability to hold higher electric field increases. As discussed above, the donor concentration, N_d, varies inversely with the Debye length because as the number of mobile charger carriers increases, dielectric screening from these mobile charge carriers will act to compensate the electric field and decrease the depth of the accumulation or depletion. This accumulation or depletion layer width can be calculated as follows:

$$x = 2L_D\sqrt{\frac{qV_s}{kT}}$$

where V_s is the potential barrier height due to the electric field created at the interface. In terms of gas sensing, the Debye length is used to describe charge carrier transfer between base materials and heterostructure materials as well as the charge carrier transfer between sensor materials and adsorbed gas species. While improved sensing due to heterostructure formation has been attributed to many mechanisms covered in this review, depletion layer formation is one of the most useful and well-studied of these effects in terms of gas sensing. This concept has been successfully utilized by decorating lower Fermi energy level materials onto higher Fermi energy level materials. In core-shell structures, these effects can be utilized by adjusting the radius of the core to be approximately equal to the Debye length One way of increasing sensitivity to reducing gasses of a core-shell structure is choosing n-type materials so that charge carriers transfer from the shell layer to the core layer. This reduction in charge carrier concentration allows for adsorbed oxygen to completely deplete the remaining carriers in the shell layer and cause a large change in sensor resistance when reducing gasses

are introduced. The optimal thickness for these core-shell type sensors must be found based on the Debye length of the two materials. The concept of the Debye length is important to explain electronic sensitization since a heterostructure's ability to alter conduction in the base material is a function of the Debye length.

1.8.2 Electronic sensitization

Electronic sensitization occurs when the number of charge carriers available for conduction is altered, as a result, the Fermi level will also be altered. This phenomenon has also been referred to as "Fermi level pinning" because if one material has a significantly larger number of carriers (such as a metal-oxide heterojunction) the Fermi level will be fixed at the level of the material with the larger number of charge carriers. As discussed above, charge transfer from a heterojunction material to a base material can cause this redistribution of charge carriers. Restriction of the number of mobile charge carriers in the major conducting channel backbone can benefit gas sensing because when fewer carriers are present, gas adsorption will localize the few remaining charge carriers near the surface and the bulk resistance will change dramatically. In turn, this charge carrier redistribution increases the charge carrier density in the heterostructure material. The synergistic relationship between increased resistance modulation from electron depletion in the backbone material and increased surface activity in the heterostructure material allows for improvement opportunities in both sensitivity and selectivity.

1.8.3 Chemical sensitization

The buildup of negative charge that occurs when electrons flow from the metal oxide to the noble metal causes a local negative charge in the noble metal. Oxygen can then adsorb on the noble metal, dissociate into chemisorbed monatomic oxygen and "spill-over" onto the base metal oxide surface. This process is known as "the spill-over effect". In some cases, this effect is specifically attributed to increased adsorption of oxygen, however this effect has been used in literature to explain increased adsorption for many analyte gasses. In either case, increased coverage of adsorbed gasses can facilitate measurable changes in captured charge at the surface which, for nanoscale materials, controls bulk conduction.

The synergistic effect of the chemical sensitization from these adsorption processes and the electronic sensitization from electron depletion in the base material worked

together to increase selectivity and sensitivity, respectively. In this case, chemical sensitization involved desorption of reaction products and sequestration of interfering gasses which allowed for more surface activity of the desired analyte gas. The ability to organize and predict the relationship between these factors remains a huge challenge for creating a bottom-up approach for sensor design; the addition of platinum has been utilized in many studies that did not find similar results in selectivity improvements.

1.9 Pristine graphene

Graphene has been widely applied for gas-sensing applications mainly due to its high specific surface area, fast electron transport, and high conductivity. In addition, the low electrical noise of graphene makes it exhibit very high gas adsorption performance. In 2007, Schedin et al. used mechanically stripped graphene for the detection of individual gas molecules (44) . In the experiment, the response of graphene to 1 ppm of ammonia (NH_3), carbon monoxide (CO), nitric oxide (NO) and water vapor was measured and the change of resistance was recorded. The electron transfer to the graphene material from the gas molecules adsorbed on the surface of graphene resulted in reduced conductivity, which increased resistance, for NH_3, CO and NO. The opposite happened after the injection of oxidizing gases such as water vapor and nitrogen dioxide (NO_2). In 2012, Hwang et al. from Yonsei University studied the response of graphene to NH_3 with different layer number and length-to-width (l/w) ratio (45). The graphene was prepared from highly oriented pyrolytic graphite (HOPG) through mechanical cleavage in order to produce graphene with high crystal quality. Different layers of graphene have similar responses to NH_3, indicating that the graphene layer (mono-, bi- and tri-layer) has does not impact on the sensitivity of the gas sensing film. Moreover, they find out that response time and response intensity changes with the change of L/w. To sum up, the key factor that affects the sensing behaviour of graphene towards NH_3 is the aspect ratio of the sheets rather than the number layers. Micro-mechanical exfoliation method is inefficient, time-consuming, and cannot meet the requirements of wholesale industrialization. chemical vapour deposition can fill this gap and achieve relatively large area preparation of high quality graphene. Following this route, in 2012, Fazel Yavari et al. detected trace amounts of NO_2 and NH_3 at room temperature and using graphene films synthesized by CVD (46). The LOD were 100 parts-per-billion

(ppb) for NO_2 and 500 ppb for NH_3, which were markedly superior to commercially available NO_2 and NH_3 detectors. It is observed that the pristine graphene has rapid response and low detection limit to NO_2, NH_3 and some organic gas. Theoretically, even a single molecules can be detected. However, the sensitivity is not high, and it must be accurately detected by precision instrument. There are a few structures of gas sensor being proposed, such as wearable gas sensor, gas sensor based on micro-heater and so on, which brings some limitations to the application of graphene in carious field. Above all, shortening the adsorption process is difficult and this is also one direction to enhance gas sensor performance in the future.

1.10 Graphene oxide and reduced graphene oxide

Graphene Oxide features diverse functional groups that make its chemical and physical properties largely different from those of pure graphene. These properties, such as high-carrier mobility, tunable band gap, high mechanical strength and thermal conductivity, have naturally attracted the interest of the researchers, allowing extensive application in the field of nanoelectronics, supercapacitors, sensors, H_2 storage, drug delivery, fuel cells, transistors, and polymer nanocomposites (47, 48, 49, 50, 51, 52, 53, 54). GO-based gas sensors have been widely investigated by researchers and the number of publications has increased considerably over the last years. Indeed, its large specific surface area makes GO a promising material for applications where functionality is magnified by the extension of the surface exposed for interaction with the environment. At the same time, the high charge-carrier mobility enhances the transduction of the chemo-physical conditions variation, e.g. as occurs in chemoresistive gas sensors. Contrary to graphene and reduced graphene oxide, widely used for gas sensing applications both as pristine material and in functionalized arrangements (55), GO is proton conductive and hydrophilic, which makes it a promising material for moisture sensing (56, 57). The interaction with certain gases, e.g. water vapour, NO_2 and H_2 (58), can be controlled by tuning the physical properties of GO sheets by reduction and/or chemical functionalization approaches (59). By removal of oxygen and recovery of aromatic double bonded carbons in GO using a reducing agent, the conductivity can be recovered to several orders of magnitude. Even so, instead of using pristine graphene, some remaining oxygen groups may be present after long exposure to reducing agents; simultaneously, some

vacancies and structural defects can be introduced as well. Therefore, rGO is highly conductive and has chemically active defect sites, making it a promising candidate for gas sensing. Hydrazine is the most commonly used reducing agent for reducing GO. Robinson et al. reported the molecular sensors based on hydrazine-reduced GO thin-film networks.(60) The specific fabrication process was as follows: First, GO powder was resuspended in a solution of methanol and water and then cast onto a SiO2/Si substrate to form GO thin films. . Subsequently, the device was reduced by exposing to a hydrazine hydrate vapour. The reduction process can be tuned by varying the exposure time to hydrazine hydrate vapour; thereby, the oxygen defect density can be changed. Recently, Sodium borohydride ($NaBH_4$) was demonstrated to function more effectively than hydrazine as a reductant of graphene oxide. Though $NaBH_4$ is slowly hydrolyzed by water, this process is kinetically slow enough that freshly prepared solutions, having a large excess of reducing agent, still function effectively as reductants of graphene oxide. The scalability of such an approach, given its inherent inefficiencies, remains uncertain, however. The use of borohydride has the additional advantage of introducing few, if any, heteroatoms to the graphene structure following reduction. Consistent with its demonstrated reactivity in other organic reactions, $NaBH_4$ is most effective at reducing C=O species, while having low to moderate efficacy in the reduction of epoxides and carboxylic acids. Additional alcohols are the principal impurities that are generated during this reductive process (as a result of the hydrolysis of the boronic ester). This is reflected in the relatively high heteroatom content of the C 1s peak in the XPS spectrum (13.4% for $NaBH_4$; 14.5% for hydrazine). The very low sheet resistance of these products suggests that heteroatom content may be a minor concern in producing useful graphene samples, however. For graphene structures that are contaminated with large amounts of alcohols (such as those obtained after borohydride reduction), this is a particularly useful workup procedure. The use of multiple chemical reductants has also been demonstrated as a route to rigorously reduced graphene, though the benefit of this approach appears limited given the effectiveness of hydrazine and $NaBH_4$ on their own. Guha et al. developed the $NaBH_4$ reduced GO based gas sensors on ceramic substrates and reported their performance for NH3 detection at room temperature.(61) The reduction time of GO can optimize the sensing response to NH_3, along with the response and recovery time. The response of rGO sensors lay between 5.5% at 200 ppm and 23% at 2800 ppm of NH_3, and the resistance recovered

quickly without heating. Moreover, the rGO sensor exhibited high selectivity for NH_3. Ascorbic acid (Vitamin C) is another nontoxic reducing agent and its efficiency in the reduction of GO is matched by hydrazine (62). Reduction with vitamin C can be carried out in water and some common organic solvents. Therefore, vitamin C is an ideal substitute for hydrazine in the large-scale production of rGO. For example, Manohar et al. developed a flexible sensor based on rGO reduced by vitamin C, which was fabricated through using the inkjet printing technique on the poly(ethylene terephthalate) (PET) substrate (63). The rGO sensor can be used to reversibly detect NO_2 and Cl_2 vapours adopting an air sample at room temperature. Other reductants have been used for the chemical formation of graphene including hydroquinone, gaseous hydrogen (after thermal expansion), and strongly alkaline solutions.Reduction by hydrogen proved to be effective (C:O ratio of 10.8-14.9:1), while hydroquinone and alkaline solutions tend to be inferior to stronger reductants, such as hydrazine and sodium borohydride, based on semiquantitative results. Sulfuric acid or other strong acids can also be used to facilitate dehydration of the graphene surface (64).

Except for chemical reduction of GO to rGO using a reducing agent, GO can be reduced through other methods, such as thermal reduction or laser reduction. For example, Sinitskii et al. demonstrated an array of thermally reduced GO-based integrated sensors, where each rGO sensor had a unique response due to the irregular structure of rGO films ranging from nanoscale to macroscale (65). Laser irradiation can also directly reduce and pattern GO films, which is a mask free method to large-area fabricate rGO. For example, Kaner et al. reported all-carbon gas sensors fabricated directly by laser reducing and patterning of GO on various flexible substrates (66). This laser ascribed GO sensor showed good, reversible sensing for NO_2, and the easy fabrication process made it quite advantageous for gas-sensing systems. In another report, the laser reduced and patterned GO was used to produce a flexible humidity sensor (67). Hierarchical rGO nanostructures introduced through the laser reduction held great promise for gas adsorption and increased their sensing performance. The oxygen functional groups could be changed by tuning the laser reduction degree, and subsequently, the conductivity of the rGO film could also be changed. As a result, the laser-reduced GO sensor showed not only excellent sensitivity to humidity at room temperature but also a fast and tunable response/recovery time.

1.11 Chemical modification of graphene oxide and reduced graphene oxide

As proposed by the Lerf-Klinowski model (68), GO nanosheets have chemically reactive oxygen-based functionality groups, such as carboxylic acid on the edge, hydroxyl and epoxy groups on the surface. An ideal approach to the chemical modification of graphene oxide would utilize reactions of these groups to selectively functionalize one site over another (69, 70). chemical modification of rGO can introduce some foreign groups or atoms to change the surface properties of to change the surface properties of rGO, and the chemically modified graphene (CMG) showed enhanced sensing performances. As an example, Yuan et al. reported optical NO_2 gas sensors using sulfo group-modified high-temperature-reduced GO (S-hrGO). (71) The S-h-rGO sensor exhibited excellent NO_2 sensing performance due to the polarization absorption effect of graphene, including high sensitivity and low detection limit with fast response, good linearity, and reversibility. Recently, we have proposed a humidity sensing mechanism based on H-bond interaction between the film and water molecules. The sensing unit holds all the fundamental properties for a good-quality gas sensor. Furthermore, We have also demonstrated significant enhancement in performance vs. pure graphene oxide (72).

1.12 Metal decorated graphene

Compared to pristine graphene or GO and rGO, gas sensors based on metal decorated graphene have demonstrated high sensitivity and selectivity, which was attributed to the large changes in the electronic properties of graphene/rGO upon exposure to gases due to the diverse functionalities and synergistic effects of metal and graphene (73). Metal nanoparticles (NPs) including Pt, Au, Pd, and Ag were used to decorate graphene and rGO to form hybrid composites, which exhibited enhanced sensing performance (74).

1.12.1 Pd/Pt -graphene nanocomposites

Palladium forms hydrides (PdH_x) on its surface upon hydrogen adsorption and subsequent dissociation. Diffusion and high sticking coefficient and high selectivity for hydrogen makes palladium the most ideal material for hydrogen gas sensing (75). However, dramatic increase in cost of bulk palladium in recent years has rendered its use in gas sensors economically unviable (76). Moreover, pristine graphene and even rGO are shown to have insignificant sensitivity towards hydrogen (77). Thus, palladium in the form of decorated nanostructures on graphene sheets is an attractive option as a selective gas sensing material. Furthermore, it has been shown that palladium surface exhibits lattice expansion and contraction on hydrogen adsorption and desorption, respectively. Therefore, given the mechanical strength of individual graphene sheets, palladium-graphene nanocomposite is expected to provide enhanced mechanical and topographical stability to the sensing material (78). A detailed study of sensitivity, selectivity, and stability done by Phan and Chung (79) reveals that PdNP/rGO based chemo-resistive gas sensors are sensitive up to 0.2 ppm concentration of H_2 in the atmosphere. The sensor fabricated on SiO_2/Si substrate showed appreciable stability for more than 6 months. It was shown that the Pd nanoparticle size of 70 nm was best suited for H_2 sensing application and showed a linear response within a range of 1-1000 ppm. Furthermore, they showed that the H_2 response for Pd nanocube/graphene composite increased with increasing particle size due to bigger spill over zone and increased penetrability of the material (80).

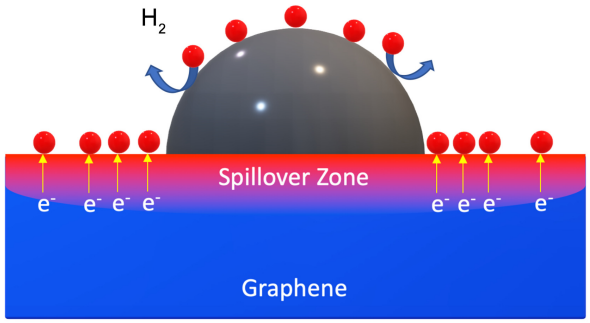

Figure 1.9: Schematic representation of spill over zone formation in Pd-Graphene nanocomposites upon H_2 exposure depicting transfer of hydrogen atoms to graphene via Pd nanostructure.

Hydrogen response of sensor systems involving Pd is governed by the spill over effect. Hydrogen spillover effect, as depicted in Figure 1.9, can be defined as the dissociative chemo-sorption of hydrogen into the metal nanoparticles and their subsequent transfer to the adjoining adsorbate surface upon saturation. The larger the nanoparticle size, the bigger the spill over zones formed, which leads to greater H_2 response.(81) However, too large particle size would reduce the surface-area to weight ratio, which will drastically affect the catalytic property of Pd.

1.12.2 Ag-graphene nanocomposites

Silver has long been known to exhibit high affinity for elements with lone pair of electrons in their valence shells, such as O, S, and N due to which, gases such as H_2S, NH_3, and O_2 are readily adsorbed on the surface of silver. Although functionalization of graphene with Ag nanostructures can theoretically result in improved sensing properties for these gases, yet weak binding of Ag ad-atoms to pristine graphene remains an issue to be addressed. Henceforth, studies have shown that structurally strained sites in graphene act as favourable binding sites for transition metals (82). Such sites readily occur in GO and rGO or may be created by mechanical straining of graphene sheets. Qin et al.(83) calculated that binding energy for Ag atoms on graphene can be increased by 44% at a tensile strain of 8%. Also, it was shown that binding energy of H_2S for such a composite was six times to that compared to pristine graphene. This makes graphene viable for H_2S sensing which was not possible without Ag atoms due to weak interactions of H_2S with graphene. It was also reported that AgNPs reduce the sensitivity of graphene toward NO_2 due to some reversal in electron withdrawing behaviour of NO_2 gas, thus improving selectivity (84).

1.12.3 Au-graphene nanocomposites

Au decorated carbon materials based gas sensors have been shown to elicit high response due to the spill over effect (catalytic action of noble metal interface for gaseous dissociation and subsequent spreading of charged gaseous ions on anchoring substrate, due to free electrons and high conductivity of these particles) at these nano-particles (85). For instance, Cittadini et al.(86) reported appreciable response to extremely low H_2 (100 ppm) and NO_2 (1 ppm) concentrations with selectivity over CO exposure for the above material. In this study, the semiconducting and photocatalytic activity

of partially reduced graphene oxide was enhanced by the Localized Surface Plasmon Resonance (LSPR) of the Au-NPs.

1.13 Metal oxide decorated graphene

The development of gas sensors based on metal oxides decorated graphene or rGO has been proved to be an effective method for achieving high-performance detection of gases, including NO_2, H_2, liquefied petroleum gas (LPG), H_2S, ethanol gas, etc. Indeed, some typical metal oxides, such as SnO_2, ZnO, TiO_2, WO_3, In_2O_3, CuO, NiO, Ga_2O_3, and V_2O_5, have been successfully used for enhancing the sensing properties of graphene and rGO based gas sensors.(87, 88, 89, 90, 91, 92, 93, 94, 95, 96) However, it is still a challenge for preparation of graphene or rGO-based gas sensors with high sensitivity, fast response, and recovery times at low operating temperature. Some studies have used several methods to improve the performance of these sensors. In the past two decades, a tremendous improvement has been demonstrated in the performance. There are many reports on the gas sensing properties of nanostructured metal oxides. However, a much smaller number of papers address the feasibility of Nb_2O_5 for gas sensing (97, 98, 99). Nb_2O_5 is known as a wide band-gap n-type metal oxide and has desirable properties such as good chemical stability, low film stress, and a high refractive index (n = 2.4 at 550 nm) (100). We report in this work the use of niobium oxide (Nb_2O_5) nanoclusters deposited onto few-layers graphene powder by magneton sputtering showing good sensing performance vs. ppm concentrations of NO_2 at room temperature.

1.14 Transition metal dichalcogenide sensors

Transition metal dichalcogenides (TMDs) are a class of materials with chemical formula of MX_2, where M indicates a transition metal element (including Ti, Zr, Hf, V, Nb, Ta, Mo, W, Re, etc), and X represents a chalcogen (Se, S or Te) (101). Bulk crystals of TMDs have been long studied, but in recent years the isolation of their 2D structures has led to renewed interest in this field. 2D layered TMDs consist of a plane of metal atoms covalently bonded to the chalcogen atoms. To date, several inorganic 2D TMDs

layered materials including MoS_2, WS_2, MoSe, WSe_2, and III-VI group semiconducting layered materials GaS and GaSe, have been reported and identified for possible gas sensing applications. So far, disulfides play the key role for gas sensing among the variety of TDMs materials due to their unique physical and chemical properties, including semiconducting property, high surface-tovolume ratio, sizable bandgaps, high absorption coefficient, and availability of reactive sites for redox reactions (102).

In this specific class, MoS_2 is the most dominating thin 2D non-graphene material in gas sensor applications owing to its ability to differentiate between a charge donor and an acceptor analyte. The MoS_2 crystal (Figure 1.10) consists of a metal Mo layer sandwiched between two S layers, with these triple layers stacking together to form a layered structure (103).

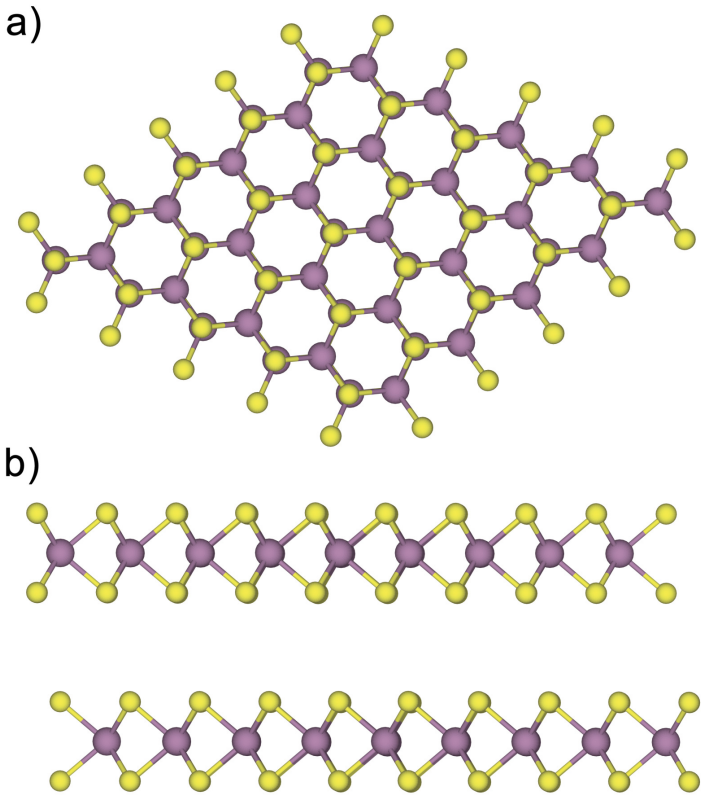

Figure 1.10: Simulation of the atomic-layered MoS_2. The quasi-2D MoS_2 was occupied by one Mo(a trigonal prismatic structure) and two S atoms (hexagonal planes) top view (a), side view(b)

1.15 Phosphorene sensors

The increasing demand of new materials in the field of gas sensing have constantly pushed forward the research in material science and technology in the recent years. In particular, the needs of high selective materials over a single analyte and room-temperature (RT) operation are key feature to possess for any high-performance gas sensing device. In the majority of currently employed materials for gas detection, such as metal-oxide semiconductors (MOX), the lack of selectivity and the need of high operating temperature, typically ranging within 250-650 °C, are typical drawbacks that prevent the wide use of MOX in harsh or industrial environments. At room or low temperature, MOX sensors lack sensitivity, stability, and ultimately reversibility of the detection process at the surface. In recent years, two-dimensional (2D) materials such as graphene, transition metal dichalcogenides (TMD) and phosphorene have attracted the interest of the research community due to their unique chemical and physical characteristics, showing kinetics of reaction as rapid as for heated conventional material-based devices, through their sensitivity and stability still remains significantly lower. In fact, the atomically thin geometry makes their electronic properties highly susceptible to the environment changes. Phosphorene is a monolayer of black phosphorus with a puckered honeycomb structure, which possesses unique direct and tunable band gap ranging from 0.3 eV (bulk) to 2.0 eV (monolayer) and its high carrier mobility (104) (up to 6000 cm^2 V^{-1} s^{-1}) but also for its high chemical adsorption energy, less out-of-carrier conductance, and large adsorption sites caused by its corrugate surface structure (105) as well as anisotropic electrical, optical, and thermal properties, making it a promising candidate for various applications, including FETs, solar cells, photodetectors, and sensors (106, 107, 108). The sensing characteristics of phosphorene to various gases have been investigated by both theories and experiments. For example, Zhang et al. investigated the noncovalent interaction between phosphorene and physisorbed small molecules, including CO, H_2, H_2O, NH_3, NO, NO_2, and O_2 through the first-principles calculations.(109) They also evaluated their energetics, charge transfer, and magnetic moment by the dispersion corrected DFT. The physisorbed gas molecules significantly altered the electronic and magnetic properties of phosphorene. O_2, NO_2, and NO acted as strong acceptors while CO, H_2, H_2O, and NH_3 molecules donated electrons to phosphorene. Specifically, NO_2 had the strongest interaction with phosphorene in these

molecules. The distinct charge transfer and strong binding energy between phosphorene and these physisorbed molecules provided phosphorene as a promising candidate for application in gas sensors. In addition, the moderate adsorption energy of H_2 on phosphorene implied stable H_2 storage at ambient conditions. As another example, Kou et al. studied the adsorption of CO, CO_2, NH_3, NO, and NO_2 molecules on a monolayer phosphorene by first-principles calculations (110). They first determined the optimal adsorption positions, the corresponding binding energy, and the charge transfer between phosphorene and the adsorbed molecules, resulting in that the strength of binding was highly dependent on the amount of charge transfer. NO and NO_2 exhibited the strongest binding among the considered gas molecules, suggesting that phosphorene was more sensitive to these toxic gases. Furthermore, they calculated the current voltage I-V relation with and without the gas molecule adsorption using the nonequilibrium Green's function (NEGF) formalism. The transport calculations not only showed the different changes in the current of phosphorene by different gas molecule adsorption but also exhibited large anisotropy of the I-V relation along the armchair or zig-zag directions depending on the type of molecules. Such sensitivity and selectivity to gas molecule adsorption made phosphorene a desirable candidate as a superior gas sensor, promising high-performance and wideranging applications. Abbas et al. experimentally demonstrated NO_2 gas sensing performance of multilayer phosphorene based FETs (111). The phosphorene sensors exhibited increased conduction upon exposure to NO_2 and excellent sensitivity even to 5 ppb NO_2. To study the stability of phosphorene sensors, they compared the Raman spectra before and after exposure to NO_2, which revealed no apparent change, indicating the multilayer phosphorene maintained its relative stability after sensing. When the phosphorene FET exposing to varying concentrations of NO_2 (5, 10, 20, and 40 ppb), it showed a systematic increase in conductance, which followed the Langmuir isotherm for molecules adsorbed on a surface, confirming the charge transfer from phosphorene to NO_2 as the dominant sensing mechanism. Moreover, the sensors showed a good recovery to the original conductance after argon flushing, suggesting a reversible adsorption and desorption of NO_2 with the rate constants in the range of 130–840 seconds. Comparing the three main allotropes (white, red, and black) of phosphorus, the bP has merits including thermodynamic stability and insolubility in most solvents and lesser chemical reactivity and non-flammability. Recent density functional theory (DFT) studies conducted on the

molecular adsorption energy of bP have suggested its use as a high-performance chemical sensor confirming its superior adsorption energy, even higher than that of other 2D materials (110). In particular, bP is selective for the detection of paramagnetic molecules, e.g., NO_2, in addition to high sensitivity at a limit of detection (LOD) of ppb levels (112). Despite this, stability remains an issue in practical uses of bP based gas sensors and it is of great interests to develop proper passivation schemes that can preserve the intrinsic properties and sustain the long-term environment stability. To achieve this goal and further improve the performance of the bP-based sensing devices, it results functioning to effectively tune material properties by n- or p-type functionalization, as already proved for other sensing materials such as graphene and reduced graphene oxide (113, 114, 115). In this way it is possible to control and modify bP with different chemical species.(116, 117) If the concentration and chemical sensitization levels are efficiently controlled, the selective analysis of target chemicals can be realized (118, 119). Commonly, the sensitivity of p-type material can be enhanced by tuning the morphology of the nanostructures,(120) doping with additives to electronically sensitize the oxide semiconductor,(121) or loading noble metals(119) to chemically sensitize the active surface. Among these methods, doping with additives can modulate the concentration of charge carriers, which can have a subsequent effect on the sensitivity. We propose here the study and the electrical characterization at room temperature of black phosphorus nanoflakes decorated with nickel nanoparticles (Ni/bP). The latter resulted highly selective to to different concentrations of NO_2 in a dry air environment highlighting fast and stable response over the time.

Chapter 2

Materials and Methods

2.1 Experimental Setup

A wide range of experimental measurements with different techniques covering many aspects of material characterizations have been employed during the PhD period. In this chapter, a brief overview of morphological and elemental techniques exploited will be covered. All the performed measurements were possible thanks to the collaboration between different research center. In particular, the Department of Physics and Earth Sciences of the University of Ferrara, the Structural Characterization Department of the CNR IMM in Bologna, the IMM department of Bruno Kessler Foundation in Trento, the Department of Industrial Engineering University of Trento and the ICCOM-CNR in Florence.

2.1.1 SEM-EDX

The scanning electron microscope exploits a focused beam of primary electrons to hit the sample. The primary beam is not fixed, but it scans the surface of interest: it is controlled in sequence, point by point and line by line, over a small rectangular area of the sample. During the interaction between the primary beam and the atoms of the sample, secondary electrons and other particles are emitted. Secondary electrons are captured by a detector and converted into electrical impulses, which are sent to a monitor in real time. The result is a high-resolution black and white image, with high field depth, which is similar to a normal photography. For this reason SEM images are immediately intelligible and easy to understand. The resolving power of a normal

electron microscope with tungsten cathode is about 5 nm, but some models can reach 1 nm. The sample is kept under high vacuum (10^5 Torr), as the air would prevent the beam emission since secondary electron have low energy. Besides, the sample must be conductive (or metallized), otherwise it could produce electrostatic discharge that would disturb the detection of secondary electrons. Other signals that the sample could emit after the primary beam incidence are: backscattered electrons, X-rays, electron channeling, cathode luminescence, currents induced by the beam and, only for certain samples, transmitted electrons. The sample region from which the interaction signals are emitted is called textitinteraction volume. As regards the microanalysis (EDX spectroscopy), the instrument exploits the X-rays emitted by sample upon the incidence of the accelerated electron beam. These are detected by a special detector that can be a Wave Dispersive spectrometer (WDS) or an Energy Dispersive one (EDS). The resulting image consists of an X-rays spectrum, from which it is possible to obtain the chemical composition of the analysed material, since every peak of the spectrum corresponds to a precise atomic species. The X-radiation comes from the ionization of the inner orbits of atoms by the incident beam. A primary electron can remove an electron belonging to the K, L or M atomic orbit, losing the correspondent energy EK, EL or EM. The ionized atom can acquire more stability by going down to a lower energy level or, alternatively, through the occupation of the hole by an outer electron with the emission of an X-photon. The released energy can be absorbed by another electron, which can jump out of the atom (Auger electron emission). The emitted X-radiation is characteristic of the atom and gives information about its chemical species. However, the electron beam generates not only a characteristic spectrum, but also a continuous one (background radiation), due to the interaction between electrons and the atomic nuclei. Therefore the system must be able to analyze and separate the different energies. We have mainly used two different type of SEM in our analysis:

- A Jeol JSM-7401F, available at IMM department of Bruno Kessler Foundation, was produced by Joel and is equipped with a Bruker EDX detector to perform composition analyses. The instrument (installed in February 2005) is equipped with a cold field emission source, with Secondary Electron detectors (SE) and Backscattered Electron Detectors (BSE) both “in the lens” and “in the chamber”, which offers a nominal resolution of 0,8nm at 30kV and 1,5 nm at 1kV. A special

sample bias reduces the effective beam energy and enhances the resolution at low kV (0.1 kV), thus improving performances while charging effects are minimized. An EDS system (Oxford INCA 350) with the ultra-thin window is also available for elemental detection starting from Boron. This instrument offers a state-of-the-art capability for microstructural surface characterization using an electronic beam.

- SEM Zeiss EVO 40 (available at the microscope centre of Ferrara), which allows analysing surface morphology or topography from zooming in very large areas (one-millimetre side) up to sub micrometric dimensions. The microscope is provided with a LaB^6 source with a maximum acceleration voltage of 30 kV. Identification of the chemical elements present in user-selected areas and particle sizes not smaller than micron is possible thanks to the energy dispersion spectrometer (EDS), coupled with the instrument, and suitable for X-ray microanalysis. The microscope can operate both conventionally in high vacuum or with variable pressure (SEM XVP), with a maximum pressure of 6 torr.

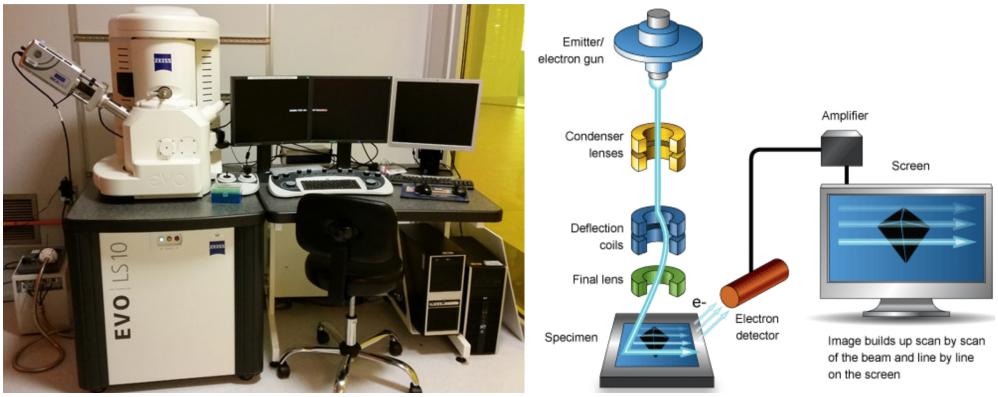

Figure 2.1: SEM Zeiss EVO LS10, located at the Structural Characterization Department of the CNR IMM, Bologna (left) and its schematic representation (right).

2.1.2 TEM Analysis

Transmission electron microscopy (TEM) is a microscopy technique in which a beam of electrons is transmitted through an ultra-thin specimen, interacting with the specimen

as it passes through it. An image is formed from the interaction of the electrons transmitted through the specimen; the image is magnified and focused onto an imaging device, such as a fluorescent screen, on a layer of photographic film, or to be detected by a sensor such as a CCD camera.

TEMs are capable of imaging at a significantly higher resolution than light microscopes, owing to the small de Broglie wavelength of electrons. This enables the instrument's user to examine fine detail even as small as a single column of atoms, which is thousands of times smaller than the smallest resolvable object in a light microscope. TEM forms a major analysis method in a range of scientific fields, in physical, chemical and biological sciences. TEMs find application in cancer research, virology, materials science as well as pollution, nanotechnology, and semiconductor research. At smaller magnifications TEM image contrast is due to absorption of electrons in the material, due to the thickness and composition of the material. At higher magnifications complex wave interactions modulate the intensity of the image, requiring expert analysis of observed images. Alternate modes of use allow for the TEM to observe modulations in chemical identity, crystal orientation, electronic structure and sample induced electron phase shift as well as the regular absorption based imaging.

In this work we have used a FEI Tecnai F20T microscope, available at CNR-IMM centre of Bologna. The instrument is provided with a Field Emission Gun (FEG) cathode, and it is equipped whit EDS x-ray microanalysis, PEELS detector and HAADF detector for STEM operation. It is possible to carry out conventional analysis of materials, such as conventional diffraction contrast imaging, HREM imaging and analysis, micro- and nanodiffraction, STEM imaging and quantitative analysis, EDS X-ray elemental microanalysis and mapping in STEM mode

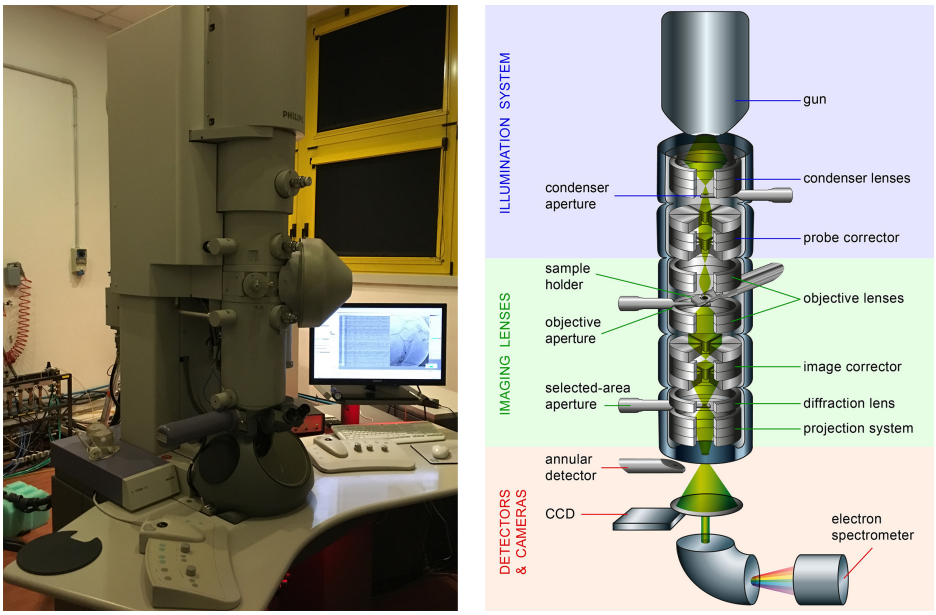

Figure 2.2: TEM FEI Tecnai F20 ST, located at the Structural Characterization Department of the CNR IMM, Bologna (left) and its schematic representation (right).

2.1.3 XPS Analysis

X-ray photoelectron spectroscopy (XPS), also knows as electron spectroscopy for chemical analysis (ESCA), is the most widely used of the contemporary surface characterization methods. A large amount of information is acquired from each spectrum and the technique is flexible enough to be used on a large variety of sample types.

Each atom on the surface of a material (except for hydrogen) is made of valence electrons that are involved in chemical bonding along with core electrons. These core electrons possess a unique binding energy which is characteristic of the type of atom to which it is bound. By analyzing the binding energies of the electrons and the peak areas, quantitative elemental surface analysis is possible. Because the electrons can only travel a short distance through the sample without undergoing inelastic collisions resulting in a drastic loss of energy, XPS is considered to be highly surface sensitive. Usually only the upper 50 Å to 100 Å of the sample is analyzed using this technique. Surface analysis by X-ray photoelectron spectroscopy begins by placing the sample in an ultra-high vacuum environment ($\approx 10^{-10}$ torr) and then irradiating the material with a source of low-energy X-rays. If the frequency of the excitation X-rays are greater

than the binding energy for each element, photoemission will occur. The resulting photoelectrons are emitted from the surface having a kinetic energy (Ek) measured by a hemispheric analyzer. Using the known x-ray energy (hν), the binding energy (Ec) is calculated using the Einstein relation seen in 2.1 where Φ is the work function of the spectrometer.

$$Ec = h\nu - Ek - \Phi \tag{2.1}$$

XPS spectra were recorded using a Scienta Esca-200 system equipped with a monochromatized Al Kα (1486.6 eV) source. The powders were attached to the sample holder using a double-sided carbon tape. An overall energy resolution of 0.4 eV was routinely used. The emission angle between the axis of the analyser and the normal to the sample surface was negligible. For each sample, Charge compensation was achieved using a flood gun and all core level peak energies were referenced to the saturated hydrocarbon in C 1 s at 285.0 eV. We have also used a Kratos AXIS Ultra^{DLD} instrument equipped with a monochromatic Al K_α (1486.6 eV) X-ray source. The emission angle between the axis of the analyzer and the normal to the sample surface was 0°. For each sample, surveys and high-resolution scans of the O 1s, N 1s and C 1s core levels were collected. XPS quantification was performed using the atomic sensitivity factors and the high-resolution scans. Charge compensation was achieved using a charge neutralizer located at the bottom of the electrostatic input lens system and all core levels were referenced to the C-C/C-H component of C 1s at 284.5 eV. Both the instruments are available at IMM department of Bruno Kessler Foundation. The XPS instrument used is available at IMM department of Bruno Kessler Foundation.

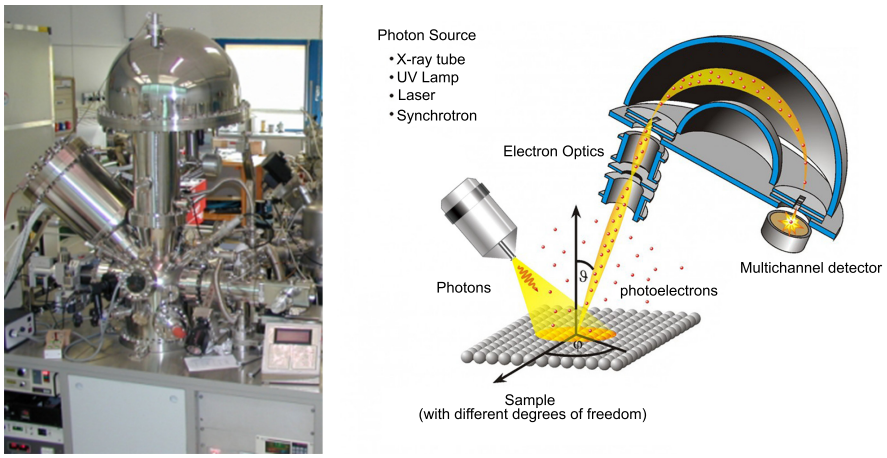

Figure 2.3: Scienta Esca-200, located at the IMM department of Bruno Kessler Foundation, Trento (left) and its schematic representation (right).

2.1.4 AFM

The atomic force microscope (AFM) is part of a larger family of instruments termed the scanning probe microscopes (SPMs). These also include the scanning tunnelling microscope (STM) and scanning near field optical microscope (SNOM), amongst others. The common factor in all SPM techniques is the use of a very sharp probe, which is scanned across a surface of interest, with the interactions between the probe and the surface being used to produce a very high resolution image of the sample, potentially to the sub-nanometre scale, depending upon the technique and sharpness of the probe tip. In the case of the AFM the probe is a stylus which interacts directly with the surface, probing the repulsive and attractive forces which exist between the probe and the sample surface to produce a high-resolution three-dimensional topographic image of the surface. The AFM was first described by Binnig et al. as a new technique for imaging the topography of surfaces to a high resolution. It was created as a solution to the limitations of the STM, which was able to image only conductive samples in vacuum. Since then the AFM has enjoyed an increasingly ubiquitous role in the study of surface science, as both an imaging and surface characterisation technique, and also as a means of probing interaction forces between surfaces or molecules of interest by the application of force to these systems. The AFM has a number of advantages over electron microscope techniques, primarily its versatility in being able to take measurements in air or

fluid environments rather than in high vacuum, which allows the imaging of polymeric and biological samples in their native state. In addition, it is highly adaptable with probes being able to be chemically functionalized to allow quantitative measurement of interactions between many different types of materials – a technique often referred to as chemical force microscopy. At the core of an AFM instrument is a sharp probe mounted near to the end of a flexible micro-cantilever arm. By raster-scanning this probe across a surface of interest and simultaneously monitoring the deflection of this arm as it meets the topographic features present on the surface, a three-dimensional picture can be built up of the surface of the sample to a high resolution. Many different variations of this basic technique are currently used to image surfaces using the AFM, depending upon the properties of the sample and the information to be extracted from it. These variations include 'static' techniques such as contact mode, where the probe remains in constant contact with the sample, and 'dynamic' modes, where the cantilever may be oscillated, such as with the intermittent or non-contact modes. The forces of interaction between the probe and the sample may also be measured as a function of distance by the monitoring of the deflection of the cantilever, providing that the spring constant of the lever arm is sufficiently calibrated.

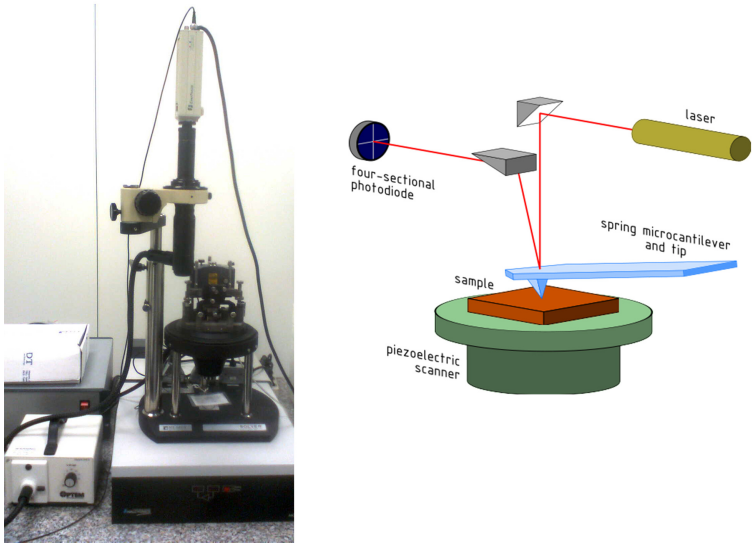

Figure 2.4: Solver P47H, located at the IMM department of Bruno Kessler Foundation, Trento (left) and its schematic representation (right).

2.1.5 Infrared spectroscopy

Vibrational spectroscopy is one of the most important tools to investigate molecular adsorbates that form on metals in the course of surface chemical reactions. Among the different vibrational techniques, infrared spectroscopy (IR) is nowadays probably the most suitable method to study catalytically relevant adsorption systems on surfaces. In comparison with other surface techniques, such as high-resolution electron energy loss (HREELS) or Raman spectroscopy, IR spectroscopy has a high resolution ($\approx$1 cm^{-1}) and high sensitivity (typically 0.1% of a CO monolayer) and can be employed on a variety of surfaces, (from single crystals to supported catalysts and complex real catalysts), both under UHV and under more realistic pressure conditions. The principle of infrared spectroscopy is based on the vibrational excitation of molecules by absorption of infrared light. The information of these vibrational spectra is related to the chemical nature of the adsorbed molecules and also to the substrate and adsorbate-adsorbate interactions.

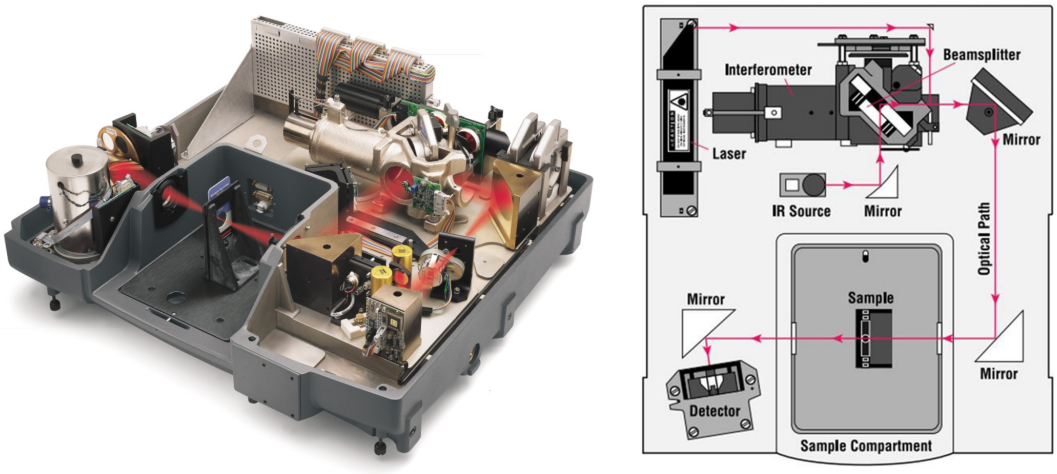

Figure 2.5: Nicolet Avatar 330, located at the Department of Industrial Engineering University of Trento (left) and its schematic representation (right).

2.1.6 X-Ray Powder Diffraction

A powder of a crystalline material contains a high number of crystallites, whose size is of the order of 0.01 nm. Since the population of crystallites is statistically oriented, surely there would be some of them arranged in the correct way to satisfy the Bragg's diffraction condition:

$$\lambda = 2d \sin \theta \tag{2.2}$$

An experiment of diffraction of X-ray from powders essentially requires: an X-ray source, the sample to be investigated and a detector able to detect the diffracted X-rays (Figure 2.6). The X radiation commonly used is that emitted by copper (whose characteristic wavelength of the K radiation is 1.5418 Å). The end result, developed by the software, is a diffraction spectrum or diffractogram constituted by a series of peaks having different intensity and angular position and relative to the various crystalline phases present in the sample. From it, the following characteristics of the sample can be read: chemical characterization, existing crystalline phases and their percentage compared to the overall crystalline phase, the average size of crystallites. In order to correctly interpretate the diffractogram, a comparison with the reference database of crystalline substances is done.

The XRD instrument used in our work is a power Bruker X-Ray Diffraction model D8 Advance diffractometer, with an X-ray tube operating at 40 kV and 40 mA, and equipped with a Si(Li) solid-state detector (SOL-X) set to measure CuKα1,2 radiation. Powder samples were side-loaded on an aluminium holder, and zero-background holder respectively. Measuring conditions were from 5 through 95° 2θ range, 0.02° 2θ scan rate, counting time per step 4 and 6 s for all powders analysed. The phase identification was achieved by search-match using the EVA v.14.0 program by Bruker and the Powder Diffraction File database (PDF) v. 9.0.133. The crystallite size of the as-synthesized nanopowder was determined by the Rietveld method, as implemented in TOPAS v.4.1 program by Bruker AXS.

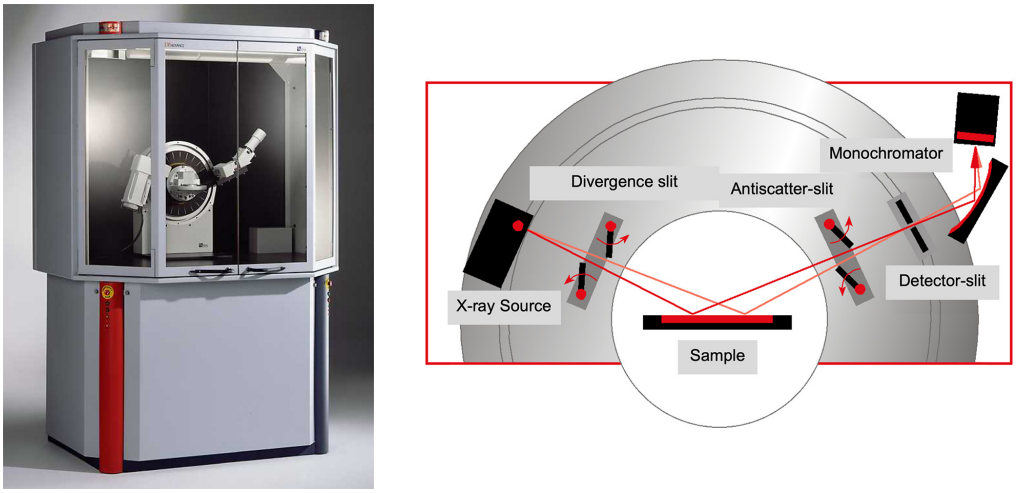

Figure 2.6: Bruker D8 Advance DaVinci diffractometer, located at Department of Physics and Earth Sciences, Ferrara (left) and its schematic representation (right).

2.1.7 Micro Raman spectroscopy

Raman scattering spectroscopy has proven to be a powerful technique for studying materials. The fact that solids, liquids and gases are able to scatter light through the Raman effect has made possible the application of this technique in a wide variety of cases ranging from monocomponent to multicomponent samples, which in turn may consist of both organic and inorganic materials. The case of pure metals has been a difficult experimental matter for Raman scattering spectroscopists due to extremely short penetration of the electromagnetic radiation in a metal, limited by the skin depth, and also to their low-Raman scattering efficiency, probably due to the small values of the Raman tensor components, whose values to date remain undetermined. The energy of the Raman scattered photons may be changed in two ways: energy lost caused by the creation of a phonon (Stokes process) or energy gained by the photon caused by the absorption of a phonon (anti-Stokes process). In either case, the energy change of the scattered photon is discrete and is directly related to the vibrational properties of the specimen. Each peak in a Raman spectrum, thus, corresponds to a particular atomic vibrational mode in the sample, and its energy measures the frequency of the corresponding atomic normal mode.

Raman scattering is a very sensitive technique to probe local atomic environments.

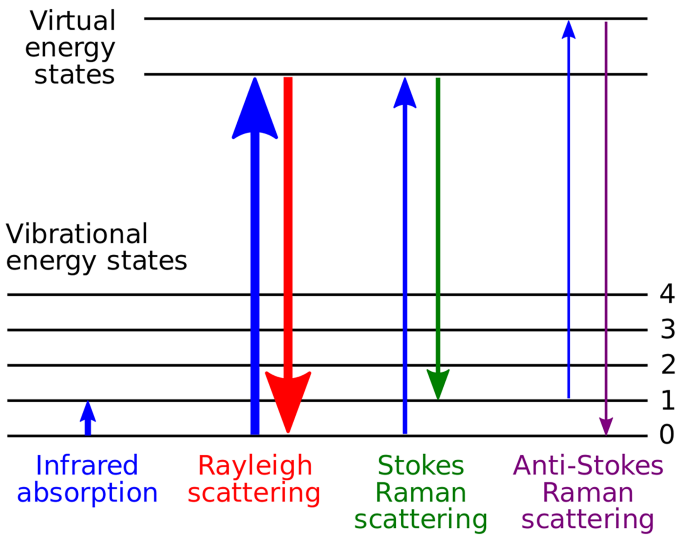

Figure 2.7: Energy-level diagram showing the states involved in Raman spectra.

Indeed, the properties of the vibrational modes are basically determined by the mass, bond type and symmetry of the constituting atoms in the elemental unit of the gas or liquid (molecule), or solid (primitive unit cell). In this fashion, the surroundings of a particular atom have a strong influence on its dynamics; therefore, the appearance of any physical factor affecting the short-range order, such as defects or impurities, have a direct impact on the atom vibrational properties. Such modifications in the vibrational characteristics of the moving atoms are readily noticeable in the Raman spectrum features. This is reflected, for instance, in the striking differences between the spectrum of a crystalline sample and that of an amorphous material of the same kind. For the interpretation of Raman spectra, the knowledge of the symmetry properties of the molecule or crystal under study is a relevant aid. Indeed, group theory applied to such systems allows one to determine the symmetry, number and activity of the atomic vibrational modes in a particular sample.

Raman measurements were performed by LabRam HR800 spectrometer (Horiba Jobin Yvon, France), coupled with an Olympus BXFM optical microscope (Olympus, Tokyo, Japan). The spectrometer was equipped with air-cooled CCD detector (1024x256 pixels) set at -70°C, and with 600 and 1800 grooves/mm gratings. The laser beam was concentrated in a spot with 1 mm diameter and the spectral resolution

was approximately 4 cm^{-1}. The He-Ne laser line at 632.82 nm was used as excitation source and was filtered to keep the laser power varying from 0.2 to 10 mW. Exposure time, beam power and accumulations were optimized for each sample in order to obtain sufficiently informative spectra but ensuring to avoid alteration of the sample.

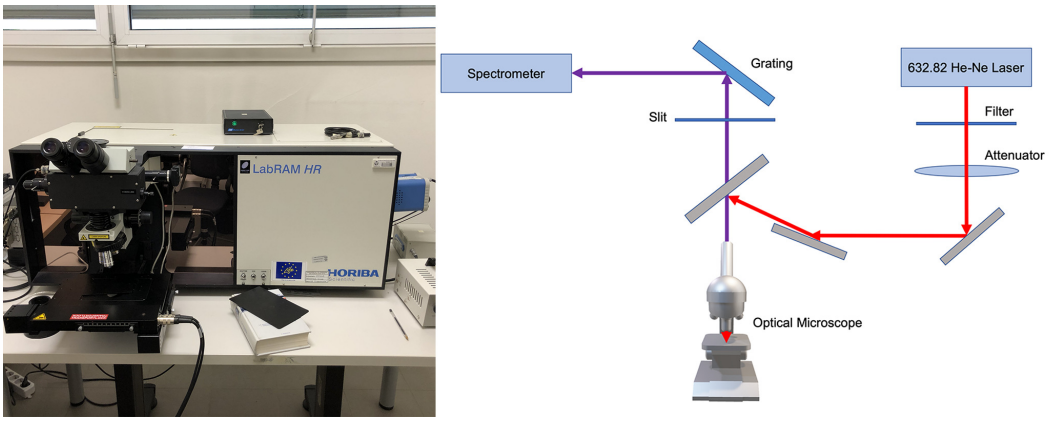

Figure 2.8: LabRam HR800 spectrometer, located at the Department of Physics and Earth Sciences, Ferrara (left) and its schematic representation (right).

2.1.8 Mechanical Profilometry measurements

The stylus instrument, through half a century of development, is one of the most widely used techniques for surface morphology measurements. The stylus profilometer can be used to measure surface morphology with a diamond stylus probe that touches the surface. Height variations are measured as either the stylus or the sample is being moved. The mechanical movements of the stylus are converted to electrical signals, which are then amplified to give DC output signals. Most modern stylus systems use digital data recording methods.

All of the stylus profilometry techniques have the following components: a gear box, a pickup, a datum, a stylus, a transducer, a sample holder, a control unit, and a data acquisition system. The pickup comprises the stylus, stylus holder mechanism, transducer, and any signal conditioning associated with the transducer. The pickup is driven by a gear box, which draws the stylus over a surface at a constant speed. As the system is scanned across a sample, the z-axis displacements of the stylus are sensed by the transducer (usually a linear variable differential transformer), which converts linearly the mechanical motion to the electrical signal. The signal, after being magnified by an electronic amplifier, is collected by a data acquisition system to generate the surface profile. The lateral length of a stylus profilometer is limited by how far the pickup can traverse. Generally this length can be as large as 300 mm. The lateral resolution depends on the shape and size of the stylus tip. It also depends on the load on the stylus. The vertical range depends on the dynamic range of the transducer and can reach as much as 6 mm. The vertical resolution is limited by the noise in the linear variable differential transformer, the airborne acoustic noise, the mechanical noise, the accuracy of the traversing mechanism, and the thermal drift. For a single-profile stylus, the noise has been measured to be as small as 0.05 nm under certain conditions. The accuracy of a stylus profilometer is limited by the accuracies of standards used to calibrate the vertical transfer and the linearity of the transducer used. The latter is typically better than 1%, i.e., the variation in measured step heights is less than 1% over the height range of the transducer.

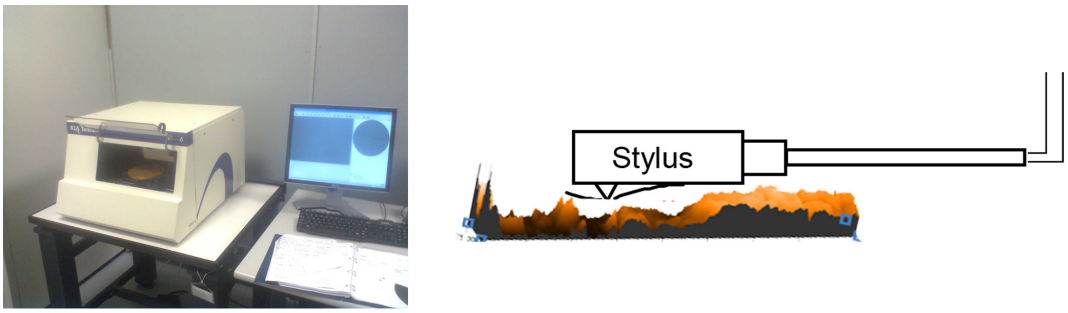

Figure 2.9: KLA-Tencor P-6 stylus profilometer, located at the IMM department of Bruno Kessler Foundation, Trento (right) and its schematic representation.

2.1.9 Total Reflection X-Ray Fluorescence

Total reflection X-rays fluorescence (TXRF) is a surface elemental analysis technique often used for the ultra-trace analysis of particles, residues, and impurities on smooth surfaces. TXRF is essentially an energy dispersive XRF technique arranged in a special geometry. An incident beam impinges upon a polished flat sample carrier at angles below the critical angle of external Total reflection for X-rays, resulting in the reflection of most of the excitation beam photons at this surface. The sample, which is a small residue deposited in the sample carrier, is seen as a very thin sample under a very small angle. Due to this configuration, the measured spectral background in TXRF is less than in conventional XRF. This reduction results in increased signal to noise ratio.

TXRF can be classified according to its application scope:

- Bulk chemical analysis: Samples are subjected to more or less intense processes of chemical treatment for suspension, dissolution, mineralization, pre-concentration and separation.
- Micro analysis: Minute amounts of sample (usually few grains) are analyzed. In this aspect TXRF is a valuable tool in archaeometry and forensics.
- Surface analysis: The chemical quality of flat surfaces is ready analyzed by TXRF.

One of the causes limiting the signal to noise ratio in EDXRF techniques based in the use of direct X-ray tube excitation is the presence of a significant background contribution in the measured spectra. This background is due to the scatter of the x-ray

tube Bremstrahlung. Scattered high energy photons not only increase the background in the high energy region of the measured spectra, but also can undertake multiple scatter acts and appear as background in the low energy region. Contrary to the behaviour of the visible light photons, for X-rays any medium is less dense than vacuum and any solid is optically less dense than air. This results in a refracted beam deflected toward the interface. Following this logic, one can see that there is a minimum critical angle $\alpha_1 = \alpha_{\text{crit}}$ for which refraction is just possible. For angles α_1 smaller than α_{crit} no beam enters the medium 2. The interface behaves like an ideal mirror and completely reflects the incident beam back into the medium 1. This phenomenon is called Total Reflection.

There are several designs of TXRF spectrometers, but for general laboratory use they are normally based on the utilization of X-ray tubes. The polychromatic collimated beam of a conventional X-rays tube is deflected by the first reflector, which alters the primary spectrum. For most applications, a quartz flat polished glass block is sufficient, acting as a low pass filter for the removal of the high energy photons of the bremsstrahlung continuum (cut off). Alternatively this first reflector can be substituted by a device acting as monochromator. Some single crystals or multilayer structured devices are used, acting as Bragg reflectors. Only the reflected beam at this spectrum modifier is allowed to hit the sample carrier under grazing incidence at an angle lower than that ensuring total reflection of the main excitation energy. The sample holder may be loaded with some sample material or may be the actual object of analysis itself. The x-ray radiation emerging from the sample is measured using an energy dispersive solid sate detector, usually a Si(Li) detector. Since scatter cross sections are minimal at 90 degrees, the detector is mounted with its entry window parallel to the sample carrier plane, in order to obtain spectra with the minimum scattered background. The distance to the sample is reduced to about 1 mm in order to secure the detection of the fluorescence radiation within a large solid angle. The measured signal is sorted by amplitude (proportional to the energy of the x-rays) in a multi-channel analyzer, leading to an energy dispersive spectrum. Measurements can be carried out in air ambient, but more sophisticated sample chamber can be designed as to perform measurements under vacuum or helium flush to reduce attenuation of the low energy characteristic emission radiation in the air.

TRFX measurements were performed by an in-house build spectrometer based on a Phoenix-TNX theta-theta diffractometer modified by DFP (Italy) and equipped with a Silicon Drift Detector (SDD) having an active area of 50 mm^2 (Ketek, Germany), was used to acquire the X-ray fluorescence photons emitted by the sample at grazing incidence. The SDD was mounted at 90 degrees with respect to the 0 degree incidence angle (theta = 90). The instrument is equipped with a Mo tube, which was operated at 40 kV and 30 mA and a parabolic graded multilayer monochromator (AXO, Germany) aligned to select the Mo Kα radiation. Aliquots of 5 μL of the solutions were deposited on a Si substrate, dried in vacuum and analyzed at 0.08 degrees incidence. The quantification was performed by ab initio simulation of the fluorescence spectrum through the GIMPy code — a software for the simulation of X-ray fluorescence and reflectivity of layered materials (122).

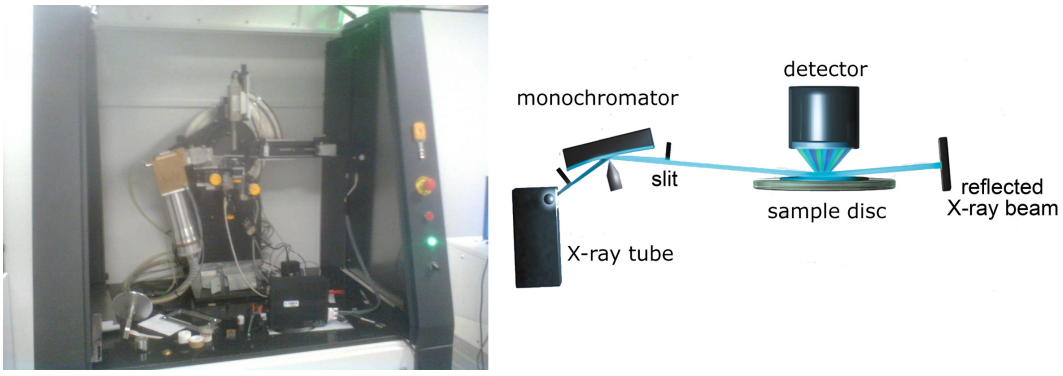

Figure 2.10: In-house build spectrometer based on a Phoenix-TNX theta-theta diffractometer modified by DFP, located at the IMM department of Bruno Kessler Foundation, Trento (left) and its schematic representation (right).

2.1.10 Radio Frequency magnetron sputtering

The preparation of nanostructures using sputtering is a method in which accelerated high-energy inert gas ions are incident on the target material to eject, or sputter, atoms or small clusters from the surface, which are subsequently deposited on the substrate in high pressure. In sputtering, two electrodes are used, one electrode is the target material and the other is the substrate, and in between are inert gas ions. Depending on the process of formation of ions and the focusing of ions, sputtering is subdivided

into direct current (DC) sputtering, radio frequency (RF) sputtering, or magnetron sputtering. In DC sputtering a high DC voltage is connected to the electrodes; usually high negative voltage is connected to the target material and positive or ground to the substrate. When the required vacuum level is reached, inert gas is introduced. In between the electrodes, due to the high electric field, energetic electrons impact the gas, creating ions. These ions then contact target material, resulting in the sputtering of nanoclusters, which are then deposited on the substrate (Figure 2.11). DC sputtering is mainly used for metal/conducting target deposition. RF sputtering, on the other hand, is mainly used if the target is insulating or near insulating materials. In this process, high-frequency alternative current (high voltage) is applied between cathode and anode, to sustain the ion production. Deposition of insulating materials is not possible in DC sputtering as it requires very high voltage to maintain discharge between the electrodes. Hence, high frequency, mostly 13.56 MHz, is used to adequately ionize the gas. In magnetron sputtering, a magnetic field is applied along with the electric field generated by DC/RF sputter, to increase the impact of ionization and also increase the focusing of the ions toward the target material. Sputtering is used to easily produce nanostructures of metals, semiconductors, and alloys, and by adding gases, such as O_2, N_2, and NH_2, metal oxides, nitrides, and carbides may also be produced.

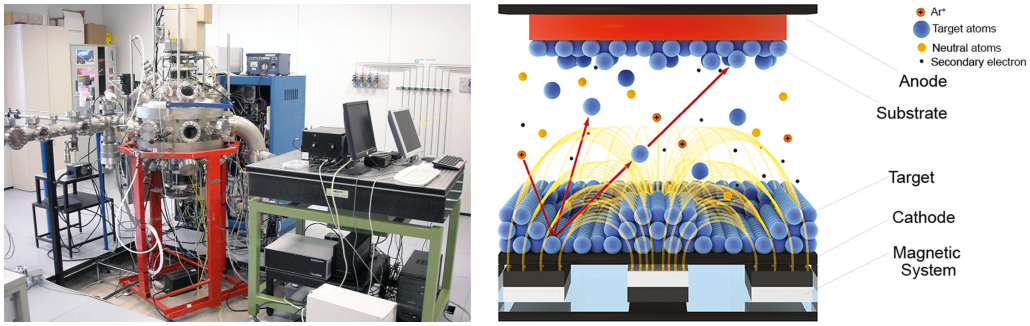

Figure 2.11: RF magnetron sputtering, located at the IMM department of Bruno Kessler Foundation, Trento (left) and its schematic representation (right).

2.1.11 Sensing films preparation and deposition techniques

The techniques for film preparation can be grouped into two categories depending either on the method used for material synthesis, i.e. whether physical or chemical, or on the fashion used for film deposition, that is, thick film or thin film technology (27). But mainly it has to consider if the material is soluble or not soluble. The Table 2.1 presents deposition and patterning techniques for solution and not processable materials

Table 2.1: Deposition and patterning techniques.

Solution processable materials		Non soluble materials	
Deposition	Patterning	Deposition	Patterning
Drop casting	Screen printing	Vacuum Thermal Evaporation	Shadow masking
Spin coating	Soft Lithography	Organic Vapour Phase Deposition	Vapour Jet Printing
Dip coating	Photo-patterning	Organic Molecular Beam Deposition	
Spray coating	Ink-jet printing		

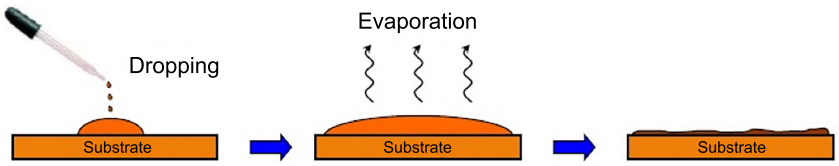

Figure 2.12: Representation of drop coating process.

Drop coating consists in application of a thin cover to a sample by depositing consecutive drops of a solution on its surface, and allowing the solvent to evaporate. With 2D materials suspensions is possible in order to use drop coating. This is an easier method than screen printing avoiding a considerable waste of material. However, this technique presents some limitations, such as small area coverage, difficult thickness control with poor uniformity. Nevertheless, these limitation can be ridded out with the use of spin coating to improve film morphology.

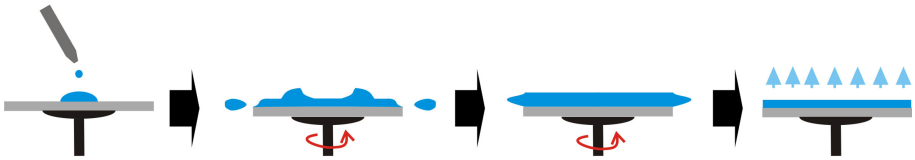

Figure 2.13: Representation of spin coating process.

2.1.12 Sensor substrates and packaging

Substrates used in gas sensing production act as mechanical support for the sensitive layer and as electric insulator between the functional compound and the circuit elements. The most commonly used substrates are made of Al_2O_3 (also known as alumina), owing to its good thermal stability, resistance to corrosion, reliability in use, excellent dielectric properties and low production costs. Alumina powder is obtained from Bauxite (the main source of aluminum in nature). It is grounded together with other oxides (SiO_2, NaO, MgO) in order to obtain a substrate with desired chemical-physical properties. Grinding is effected in a mill with blades to ensure a good mixing level. Then, the obtained compound undergoes two treatments at different pressures depending on the desired thickness. Then, after imposing a form to the substrate, firing process can occur for 12-24 hours; this thermal treatment is composed by two principal steps: pretreatment and sintering. The modulation of temperatures and of total firing times is the key point in order to optimize physical-chemical characteristics of materials. On upper alumina support interdigitated gold electrodes are deposited, whereas on the bottom side there is a platinum heating coil covered by dielectric layer (see Figure 2.14). The alumina substrate is pre-cut in square modules of 2.54 mm side by the means of laser cutting.

The substrate should not play an active role in the sensing activity, moreover, a certain compatibility between the sensitive layer and the support must subsist, in order to avoid the possible creation of tensions as a result of possible thermal expansion. Substrates undergo superficial characterization to ensure the lowest number of possible visible surface defects. Furthermore, the substrate material must have chemical and physical compatibility with deposited sensing film. Thefinal device must be assembled

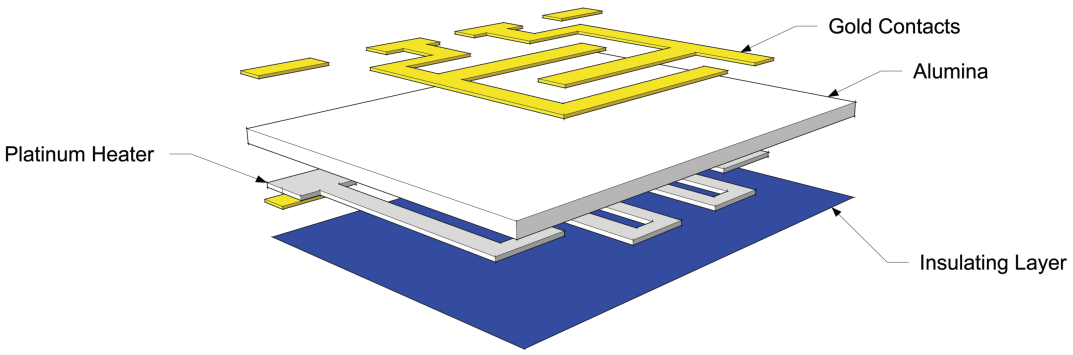

Figure 2.14: Exploded-view drawing of alumina substrate for produced sensors.

by means of bonding, which involves the connection of the sensor substrate with a dedicated support, by the means of four pins. These are welded, by thermo-compression, to the heater and to the interdigitated gold electrodes where the film is deposited. This connection involves the use of golden wires (99:99%) with a diameter of 0.06 mm and is carried out via the apparatus shown in Figure 2.15.

Figure 2.15: Example of gas sensor produced at Sensors Laboratory of Ferrara (on the left) and instrument for the packaging (on the right).

2.1.13 Electrical characterization setup

In order to evaluate the response of a sensor is mandatory to perform experimental measurements on dedicated instruments, allowing to work in ideal conditions, enabling as it the possibility to perform repeatable measurements. The apparatus, showed in Figure 2.16, used consists of:

- flow meters for gas mixing:
- test chamber;
- data acquisition system;

Gaseous molecules are fed by certified bottles into a proper pneumatic system based on mass-flow meters. This flow is then sent to the measuring chambers, at which are connected through teflon tubes. To know which flow is to be set, the following relation must be used.

$$F = \frac{F_{\mathrm{Tot}} \times C}{C_{\mathrm{bot}}} \tag{2.3}$$

where $\mathrm{F_{tot}}$ is the total flux in the flow meter, C is the gas concentration that one wants to send to the chamber and $\mathrm{C_{bot}}$ is the gas concentration in the bottle (certified by the supplier).

Gaseous molecules are fed by certified bottles into a proper pneumatic system based on mass-flow meters. A dedicated test chamber (volume of 2000 cm^3) was controlled by a circuit based on an operational amplifier (OA). The voltage values V_{in} and V_{out} are connected at the ends of sensor resistor R_S and applied load resistor R_f, respectively. Then, the gain is given by $V_{\mathrm{out}}/V_{\mathrm{in}} = -R_{\mathrm{f}}/R_S$. The expression for sensor conductance G_S results equal to:

$$G_s = \frac{1}{R_s} = \frac{V_{out}}{R_f \cdot V_{in}}$$

Sensor response is defined as:

$$Response = \frac{G_{gas} - G_{air}}{G_{air}}$$

where G_{gas} and G_{air} are the steady-state conductances in gas and in air, respectively (123). The acquisition system must manage all phases regarding the sensor electronics

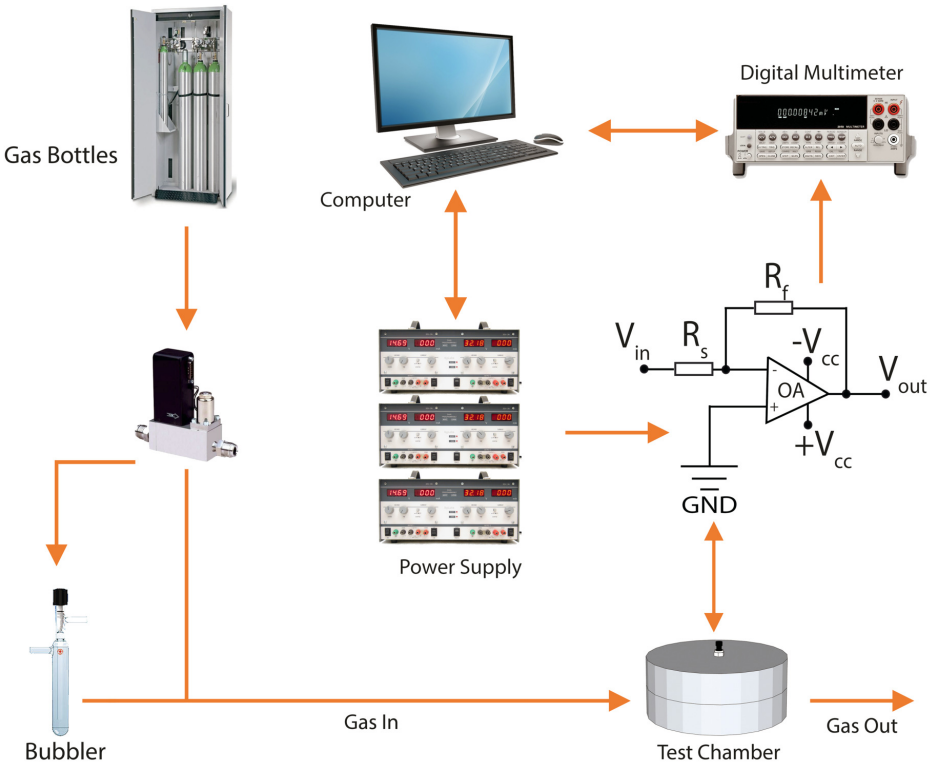

Figure 2.16: Schematic representation of the gas mixing and data acquisition system.

and is composed of a Keitheley K2000 Multimeter, to convert output voltages from analog to digital, and a management/acquisition software consisting of an acquiring software, at regular intervals, the input channel of the multimeter (gas sensor, temperature sensor and humidity sensor). The sensing measures were performed in either dry or wet air, gas from certified synthetic air bottles (20% O_2 and 80% N_2) were fluxed through mass-flow controllers with a fixed flow of 500 cc/min. A fixed fraction of the total flux came from the gas bubbler filled with distilled water to simulate humidity condition, the relative humidity in the test chamber has been controlled with a commercial Honeywell HIH-4000 humidity sensor.

For any new sensing material, the performance needs to be proved through the so-called 3S-rule (93):

- Sensitivity is the slope of the calibration curve, that is, how large is the change in the sensor signal upon a certain change in the analyte concentration,

- Selectivity is the ability of a sensor to respond primarily to only one chemical species (specific sensor response) in the presence of other species (interferants),
- Stability is the ability of a sensor to provide reproducible results over a certain period of time; it depends on drift of the baseline signal, drift of response, and regeneration after interaction with analyte. In particular, long-term stability is related to aging of the sensor materials.

Chapter 3

Graphene Based Materials

3.1 Niobium Oxide decorated Graphene

With the aim of coupling the characteristics of pristine graphene with the well know sensing capabilities of Nb_2O_5 we investigated the gas sensing performance of nanoclusters decorated few layer-graphene (Nb_2O_5/graphene). This composite material was obtained by using magnetron sputtering technique, in which a mixing system allow to deposit homogeneously Nb_2O_5 nanoclusters on graphene powder. Two different samples were prepared to investigate the influence of sputtering power deposition effect on the final Nb_2O_5 decorated graphene samples. The electrically characterization highlighted that Nb_2O_5/graphene sensors showed good and selective sensing properties vs. NO_2 both in dry and wet air, at room temperature.

3.1.1 Synthesis Process

Nb_2O_5 deposits were grown at room temperature on graphene powder of 1.5 nm thickness purchased from Graphene Supermarket, by means of RF magnetron sputtering of a commercially available high purity Nb_2O_5 disc (99.99%) with 5 cm diameter. A powder vibration set up was employed to uniformly coat the graphene powder with Nb_2O_5. The deposition was carried out at a 6 Pa gas pressure, with a powder vibration frequency of 10 Hz, a deposition time of 30 min and varying the electrical power at the target (50 and 80) Watt. Nb_2O_5, graphene and Nb_2O_5 nanostructured materials were mixed with ethanol and deposited onto alumina substrates, provided with gold interdigitated electrodes and platinum heater, by means of drop coating technique.

Table 3.1: Niobium content in samples 1 and 2, calculated ad Nb/C ratio through XPS analysis.

Sample	Power (W)	Vibration frequency (Hz)	Deposition time (min)	Nb/C atomic ratio (%)
Sample 1	50	10	30	3.2
Sample 2	80	10	30	7.3

3.1.2 Characterization

Chemical, structural and morphological characterizations were carried out on samples. The morphology was analysed by SEM, cold cathode JEOL Microscope, model JSM 7401-F). The chemical characterization was performed by using a Kratos AXIS Ultra^{DLD} instrument equipped with a monochromatic Al Kα (1486.6 eV) x-ray source. In the Figure 3.1 SEM and TEM characterizations are shown. In Figure 3.1 (left) is reported an image of the graphene flakes before the Nb_2O_5 deposition, meanwhile Figure 3.1 (right) highlights the change of the sample morphology after the magnetron sputtering deposition, due to the formation of Nb_2O_5 clusters over the graphene flakes surface. The average flake thickness is 1.6 nm and the specific surface area is 510 m^2/g.

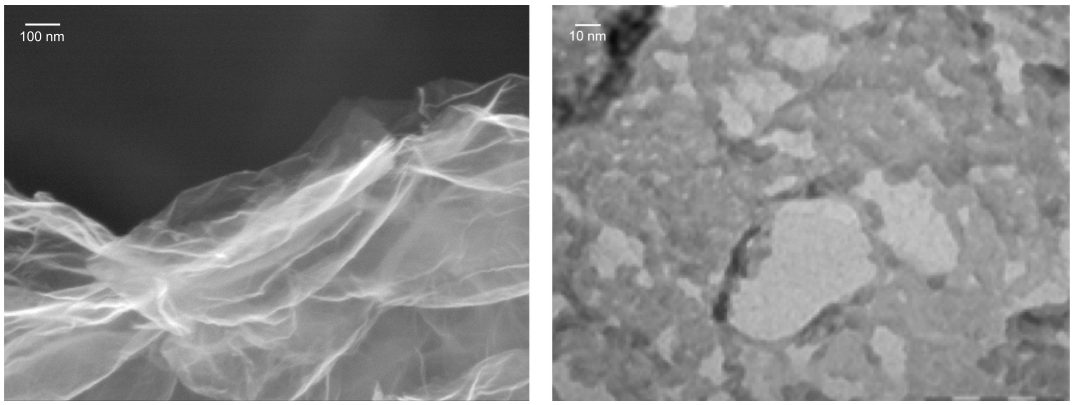

Figure 3.1: SEM images of (Left) graphene and (Right) graphene decorated with Nb_2O_5 nanoparticles (deposition power 80 Watt).

XPS analysis was carried out to investigate elemental composition and how the deposition parameters influenced the Nb_2O_5 concentration on samples (Table 3.1). Typical Nb 3d peak assignable to Nb_2O_5 can be see at ≈207 eV Moreover, symmetric peaks shapes undoubtedly identify Nb_2O_5 on Graphene surface. The C 1s spectra highlight C-C peak at binding energy of ≈284 eV. Little humps at ≈289 eV and ≈291 eV are characteristic pf pristine graphene, assignable to plasmon loss feature of graphene and C=O group, respectively. The presence of carboxylic group peak is mainly due the slight oxidation of the edges of graphene nanosheets. O 1s binding energy highlight ≈530 peak corresponding to metal oxide presence, due to Nb_2O_5 nanoparticles and two deconvoluted peaks at ≈532 and ≈ 533 eV corresponding to Organic C-O and C=O on the edges of graphene sheets, respectively.

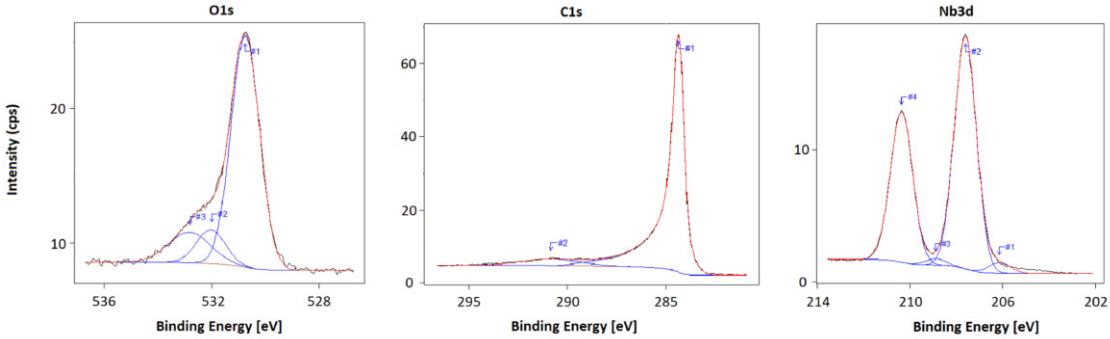

Figure 3.2: Schematic representation of the synthesis process of aza-crown-functionalized graphene oxide.

As it can be seen in Table 3.1, the change in the deposition electrical power strongly affected the Nb_2O_5/graphene concentration in the material, giving a major concentration by using 80 Watt compared to 50 Watt.

3.1.3 Electrical characterization and gas sensing performance

Electrical characterization, in dry air, highlighted that Nb_2O_5/graphene sensors were insensitive to all gases tested, except for NO_2, at room temperature. The same measurements were repeated in presence of wet air, showing that the selectivity of the sensing material to NO_2 was not affected by the presence of moisture. Furthermore, the

response values obtained in dry and wet air were comparable up to a relative humidity of 40% (Figure 3.3).

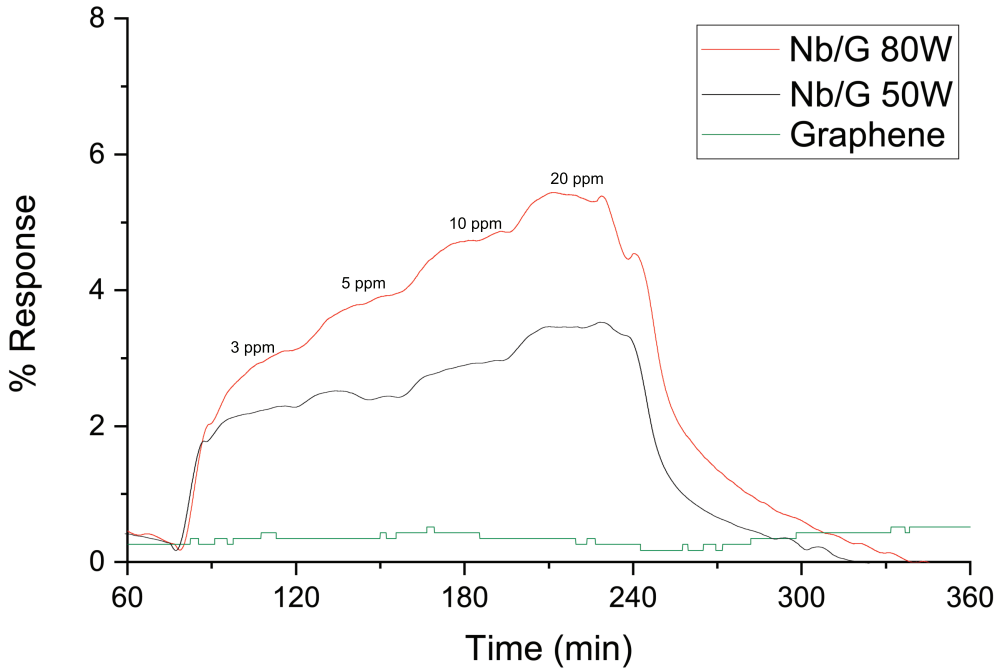

Figure 3.3: % Sensing response of a Nb_2O_5/graphene sensors and pristine graphene vs. 3, 5, 10, 20 ppm of NO_2, in wet air (RH%=40%, T=23 °C).

The response of sensors was strongly influenced by the concentration of Nb_2O_5 on the surface of the graphene flakes. Indeed, the sensor obtained by depositing the sample with the highest concentration of Nb_2O_5 showed responses 1.5 times higher than the less concentrated one (Figure 3.4).

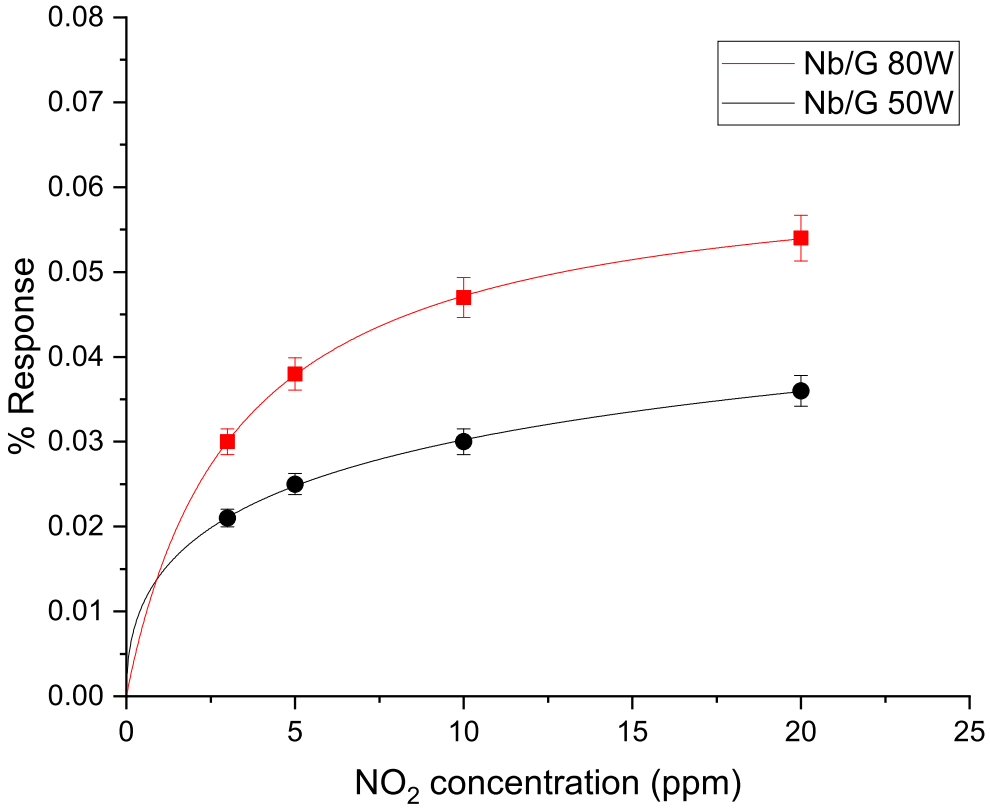

Figure 3.4: Sensitivity of Nb_2O_5/graphene sensors vs. NO_2 concentrations (RH%=40%, T=23 °C).

3.1.4 Proposed sensing mechanism

The sensitivity of the Nb_2O_5/graphene composites towards NO_2 is tentatively explained from the following aspects. First, the introduction of Nb_2O_5 prevents the graphene sheets from restacking, thus leading to a good surface accessibility and effective gas diffusion between parallel layers of graphene, which may contribute to the gas sensing enhancement. Second, electrons should flow from the n-type material to the p-type conducting backbone. This should cause electron-hole recombination which would decrease conductivity in the p-type metal oxide backbone. When an oxidizing gas is in-

troduced, less electrons would be introduced into the p-type conducting channel, further enhancing the number of conducting holes. This could improve resistance modulation in the same way as synergistic effects with n-type conducting channels. Decoration of n-type metal oxides such as Nb_2O_5 onto p-type materials such as graphene has been used to improve sensing response and selectivity.

3.2 Aza-crown-functionalized graphene oxide composite

As proposed by the Lerf-Klinowski model (68), GO nanosheets have chemically reactive oxygen-based functionality groups, such as carboxylic acid on the edge, hydroxyl and epoxy groups on the surface. An ideal approach to the chemical modification of graphene oxide would utilize reactions of these groups to selectively functionalize one site over another (69, 70). In particular, the GO platelets feature chemically reactive epoxy groups on their basal planes. The amount of these groups depends on the GO oxidation degree. They can easily be modified under various conditions through ring-opening reactions (124), an effective mechanism, which involves the nucleophilic attack at the α-carbon by the amine group, i.e. aza-crown ether composites amine site (125). Cyclic ether functionalities provide a potential acceptor site for chemical species due to charge distribution and to their consequent affinity to some chemical species (e.g. polar molecules and cations). Thus, being interested in straightening the properties of reversible and controlled interaction of the surface with different chemical species, we functionalized GO with 1-aza-15-crown-5 ether via chemical route synthesis and explored two possible applications of the functionalized graphene oxide (FGO) We probed the possible use of FGO for gas sensing, especially for selectively sensing humidity under room temperature conditions, and as cation membrane. In order to achieve these goals, we prepared FGO by tuning different synthesis parameters, then we compared the functionalized material to pristine GO from a morphological, structural and chemical point of view. FGO and GO films were deposited and comparatively probed vs. detection of gaseous molecules.

3.2.1 Synthesis Process

The synthetic procedure adopted for the preparation of aza-crown-functionalized graphene oxide composite is shown in Figure 3.5.

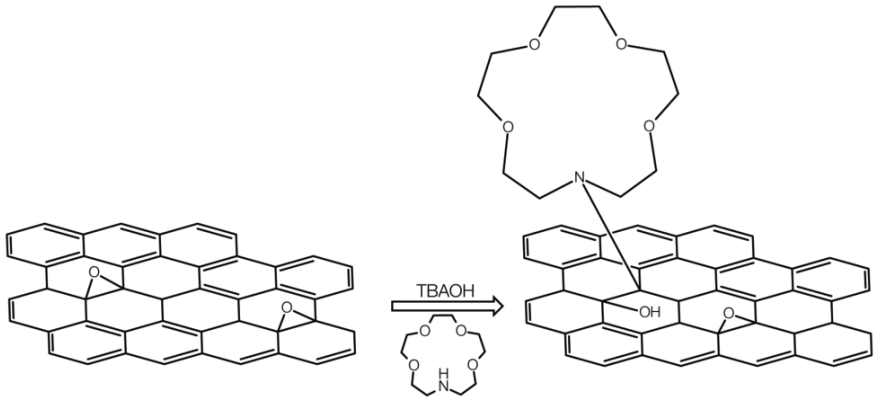

Figure 3.5: Schematic representation of the synthesis process of aza-crown-functionalized graphene oxide. Reprinted with permission from (72). Copyright IOP Publishing.

Aza-crown-functionalized GO was obtained starting from commercial GO (4 mg/mL) (Sigma-Aldrich), 1 mL of GO solution was diluted to 10 mL with deionized water in a beaker, thus stirred to obtain a clear homogeneous brown dispersion (0.4 mg/mL). 1-Aza-15-crown-5 (TCI Europe) and tetrabutylammonium hydroxide (TBAOH) (Sigma-Aldrich) were added to the GO solution at room temperature. The role of the latter in the reaction mechanism is to deprotonate the nucleophile in order to increase its nucleophilicity and hence the rate with which the nucleophilic substitution takes place. The mixture was stirred and heated gradually up to 80 °C. Then, the temperature was kept constant for 20 h and thermalized to room temperature.

3.2.2 Morphological and structural characterization

AFM was used to determine the thickness and size of GO and FGO nanosheets. AFM data were acquired in semi-contact mode with a silicon tip NGS10 (resonant frequency 140-390 kHz, force constant 3.1-37.6 N/m) with a nominal radius of less than 10 nm. The scan areas range between 30x30 μm^2 (not reported) to 10x10 and 5x5 μm^2 and 3x3 μm^2. Samples were dispersed in deionized water and deposited onto silicon substrates. In this way GO and FGO monolayer can be recognized and analyzed. Thickness and size of GO and FGO nanosheets resulted to be in the range of 1 to 8 μm wide and $\approx$1.7 nm thick for the GO. The lateral dimensions of FGO were of the order of 1-4 μm in widness and $\approx$1.8 nm in thickness and present elongated shape. Multi-layer stacking in FGO prevail over single sheet, which is presumably caused by the basal plane functionalization.

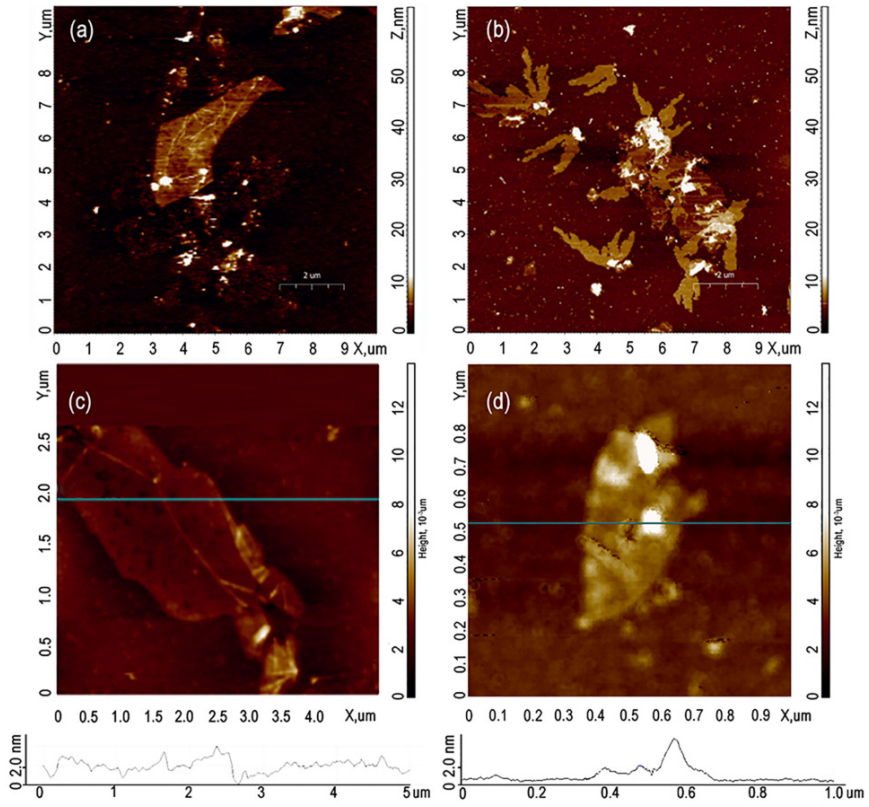

Figure 3.6: AFM images in semicontact mode of (a) GO and (b) FGO 2.5x2.5 μm and 10x10 μm scanned area, (c) GO and (d) FGO nanosheets and corresponding height profiles. Reprinted with permission from (72). Copyright IOP Publishing.

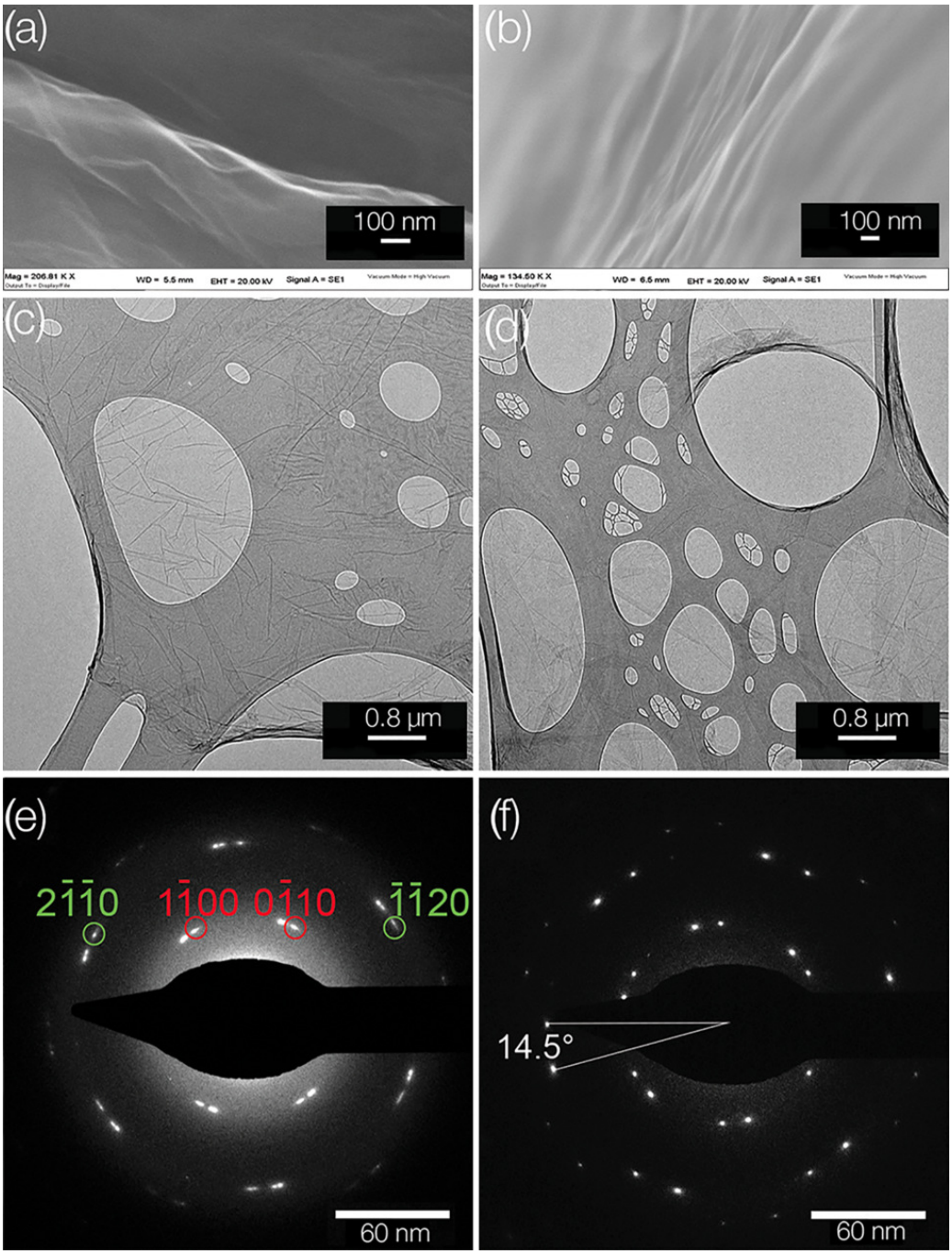

Figure 3.7: SEM images of (a) GO and (b) FGO 1:1 sheets. TEM images of (c) GO and (d) FGO 1:1 sheets. SAED of (e) GO and (f) FGO 1:1 sheets (diffraction spots are labeled with Miller - Bravais indices). Reprinted with permission from (72). Copyright IOP Publishing.

SEM, TEM images and the Selected Area Electron Diffraction (SAED) of GO and synthetized FGO 1:1 films presents similar smooth featureless surface patterns. In Figures 3.7c and 3.7d TEM images do not show markable differences between GO and FGO films. In particular, in the bottom left of Figure 3.7c and in the upper right of figure 3.7d overlapped sheets can be observed by the different contrast. SAED patterns of GO and FGO (Figure 3.7e and 3.7f) show characteristic crystalline order diffraction spots of the 6-fold rotation symmetry, consistent with the hexagonal lattice accordingly to the Miller - Bravais hk-il indexing. Figure 3.7f shows two identical hexagonal patterns rotated by an angle of 14.5°, this angle corresponds to a misorientation between two FGO sheets. Typically, FGO maintains the hexagonal symmetry of an unmodified GO, besides, FGO sheets are not completely amorphous and adjacent layers are not orderly stacked when deposited by drop-casting.

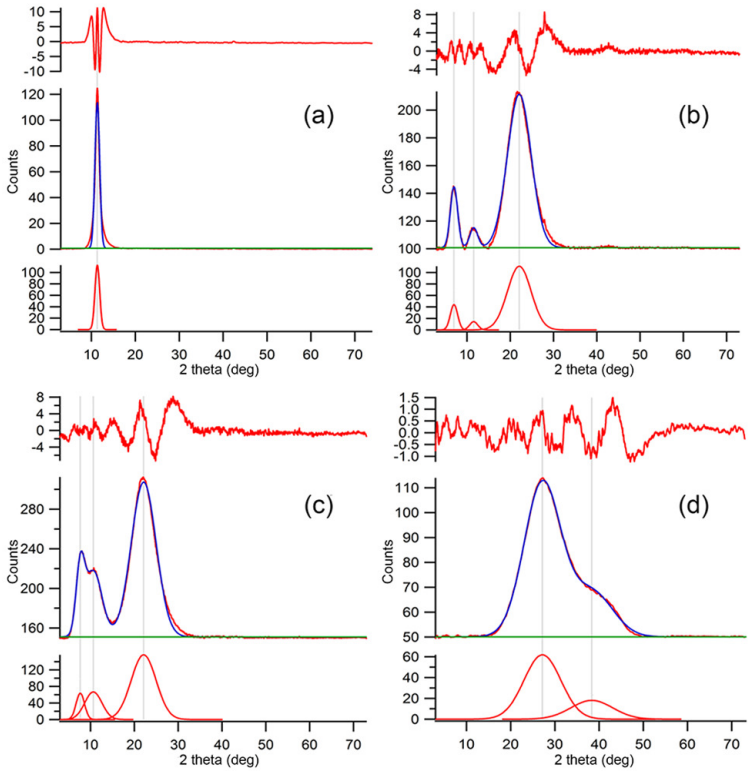

Figure 3.8: XRD pattern of (a) pristine GO, (b) FGO 1:1, (c) GO mixed with TBAOH and (d) GO with 1-Aza-15-crown-5. From the bottom of every sample plot: single fitted gaussian peaks, XRD data and fitted results and residual plots between experimental and fitted data. Reprinted with permission from (72). Copyright IOP Publishing.

Figure 3.8 shows the XRD pattern of pristine GO, FGO 1:1 composites, GO with only TBAOH and GO in solution with 1-aza-15 crown-5. The last two samples were produced while maintaining all the reaction conditions (i.e. reagents concentration and temperature) used for FGO 1:1 sample, in order to study the interaction of GO with every single reagents in the process, to allow a more straightforward interpretation of the reaction. Figure 3.8a shows the typical peak of the GO placed at about 12.0° 2-theta, due to 0001 reflection (126). FGO sample (Figure 3.8b) shows a diffraction peak at 12.0° 2-theta that is along with previously cited GO peak. In addition, there are two new peaks at 7.6° and at 22.5° 2-theta. The peak at lower angle is ascribed to an increase in interlayer separation from 7.9 to 11.5 Å due to the functionalization of GO with bulky aza-crown ligand, whereas, the higher-angle peak is assigned to disordered-graphitic system (127). GO-TBAOH (Figure 3.8c) shows, other than the previously cited peaks of FGO at 12,0° and 22,5° 2-theta, a peak at 5.4° 2-theta, which is to be ascribed to the presence of TBAOH in GO interlayers. GO-1-aza-15-crown-5 ether mixture (Figure 3.8d) presents peaks at 25.5° and at 38.0° 2-theta not overlapping with the previous patterns. In conclusion, the pristine GO, GO-TBAOH, GO-1-aza-15-crown-5 ether mixture and FGO show well defined XRD fingerprint peaks, which could be used to discriminate reaction products.

Figure 3.9 shows the FTIR spectra for GO and FGO films. According to previous FTIR studies of pure GO (128), various peaks were observed at ≈ 3385, 1720, 1600, 1220 and 1052 cm^{-1}, which correspond to the hydrogen-bonded O-H stretching, carbonyl (C=O) stretching, C=C stretching, O-H deformation and the C-O stretching of the epoxides (C-O-C), respectively. In the FGO composite, the peak at 3200 cm^{-1} is due to the presence of the -OH groups. Skeletal C=C vibrations are observed at 1570 cm^{-1}. It is also observed that some new peaks at 1230 and 1030 cm^{-1}, corresponding to C-N stretching (tertiary amine) and C-O stretching vibrations, have appeared. These results confirm that aza-crown molecules in FGO react with the oxygen-containing functional groups of GO, generating C-N covalent bonds through the nucleophilic addition reaction of amine on the epoxy group (129).

Moreover, the FTIR results are helpful to estimate the bond length, thus, the force constant of 5.8 N/cm for the C-N linkage, calculated from FTIR stretching frequency, can be correlated with the average C-N bond length by the ”Badger′s Rule”, resulting in ≈ 1.4 Å (130). Details of the full calculations are provided below.

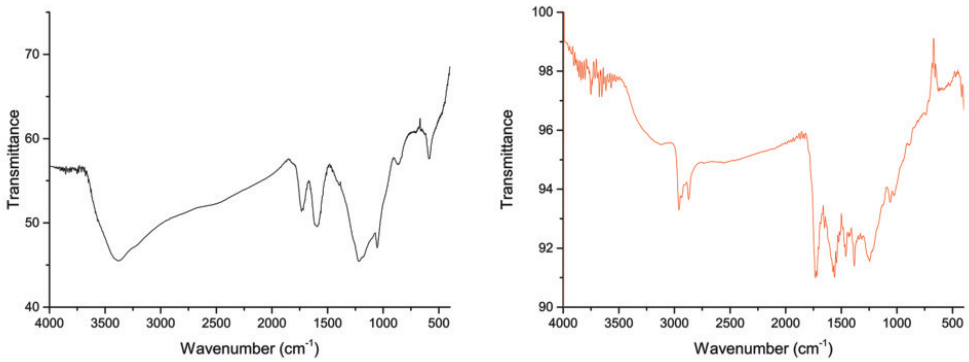

Figure 3.9: FTIR spectra of GO (left) and FGO 1:1 (right). Reprinted with permission from (72). Copyright IOP Publishing.

The vibrational frequency of C-N bond can be determined by:

$$\nu = \frac{1}{2\pi c}\sqrt{\frac{k}{\mu}}$$

where ν is wave number, c is the speed of light in vacuum, k is average force constant of the C-N bond and μ is the reduced mass given by the relation:

$$\mu = \frac{M_C \cdot M_N}{M_C + M_N}$$

where M_{C} and M_{N} are atomic weight of carbon and nitrogen, respectively. The force constant of 5.8 N/cm for the C-N linkage, calculated from FTIR stretching frequency, can be correlated with the average C-N bond length by the "Badger′s Rule", resulting in $\approx$ 1.4 Å.

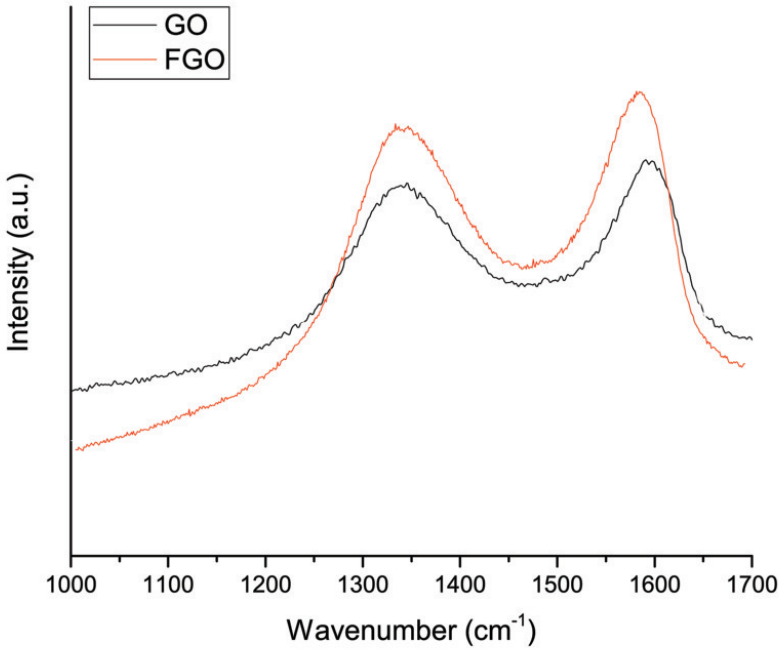

Figure 3.10: Raman spectra of GO and FGO 1:1. Reprinted with permission from (72). Copyright IOP Publishing.

In order to retrieve useful information about the composite structures, Micro-Raman analysis have been performed on GO and FGO samples (Figure 3.6). GO exhibits two main bands: G band at ≈1597 cm^{-1} corresponding to the first-order scattering of the E_2g phonon of in-plane vibration mode of sp^2 carbon atoms and the D band ≈1335 cm^{-1} assigned to the vibrations of sp^3 hybridized carbon atoms of disordered graphene such as partially disordered structures of the sp^2 network and structural defects. In aza-crown functionalized GO, the G band is red-shifted to 1590 cm^{-1}. Such shift of the binding energy of G band has also been reported by Banerjee et al(129).

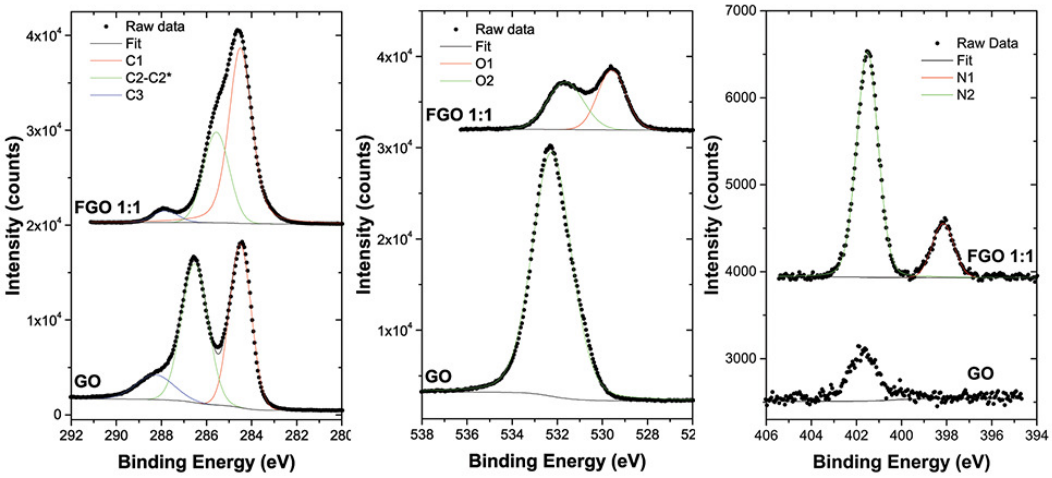

Figure 3.11: High resolution XPS spectra of GO and FGO 1:1 materials for carbon (C 1s-left), oxygen (O 1s-centre) and nitrogen (N 1s-right), showing the fit and the resulting components.

XPS spectra of GO (Figure 3.8, bottom) show clearly C 1s and O 1s core levels (left and centre panels) and a small amount of nitrogen, probably due to impurities (right panel). The carbon spectrum (Figure 3.8, left) exhibits three peaks, the C-C/C-H component at ≈284.5 eV, C-O at ≈287 eV, and carboxylic group at ≈288 eV (128). The oxygen spectrum (Figure 3.11, centre) shows a single peak at ≈532.4 eV. XPS spectra of FGO (Figure 3.11, top) show C 1s, O 1s and N 1s core levels. The carbon spectrum shows the C-C/C-H peak at ≈284.5 eV and COO at ≈288 eV and a shoulder at 285.8 eV originated from a combination of C-N and C-O bonds. One can observe that the previous C-O peak of GO (287 eV) is diminished as a result of the reduction of GO during the functionalization reaction (131). The oxygen spectrum of FGO shows two peaks at 532 eV and 529 eV, originated from the C-OH and C=O bonds, respectively. The nitrogen spectrum of FGO shows two peaks at 401.5 and 398 eV, assignable to tertiary amine N atoms in the aza-crown ether accompanied by some imine N atoms. As previously suggested by Ballesteros et al. the imines peak at 398 eV could be formed by the condensation of a 1-aza-15-crown-5-ether with GO C=O groups (125).

Table 3.2: Elemental percentages in GO and FGO samples.

Sample	%C	%O	%N
GO	68.4	30.6	1.0
FGO 1:1	81.0	14.4	4.6

Multiple XPS analyses were performed on different spot and on different produced samples also to quantify the elemental composition of GO and FGO. The percentage amounts of C, O and N are reported in Table 3.2 as the results of the elaboration of elemental survey XPS spectra. The analysis shows that the amount of oxygen decreases during the functionalization reaction, providing a reduction of GO. FGO carbon to crown-ether ratio can be determined by using the atomic percentage difference between nitrogen atoms in GO and FGO (125). This difference depends on the added functional groups of the aza-crown moiety, which amounts to 3.6% ($C_{10}H_{21}NO_4$) equivalent to an average C_{GO}:aza-crown-ether ratio of 12.5.

The characterizations results reported gave a sufficient insight to model the FGO structure through simulation. Indeed, performing MMFF94 energy minimization with a modified MM2 with Truncated-Newton-Raphson method force field, we propose a simulated FGO structure starting from GO layers (Figure 3.12), taking into account the formation of the C-N bond with the consequent increase in interlayer separation, as obtained from XRD pattern, and the previously calculated C_{GO}:aza-crown-ether ratio. Structural characteristics of simulated nanocomposite are comparable to experimental characterizations confirming the coherence between experimental and simulated data. Indeed, energy minimization distances from the simulation are consistent with experimental data, i.e. 8 Å and 12 Å for interlayer separation of GO and FGO, respectively, 1.4 Å for C-N bond for FGO.

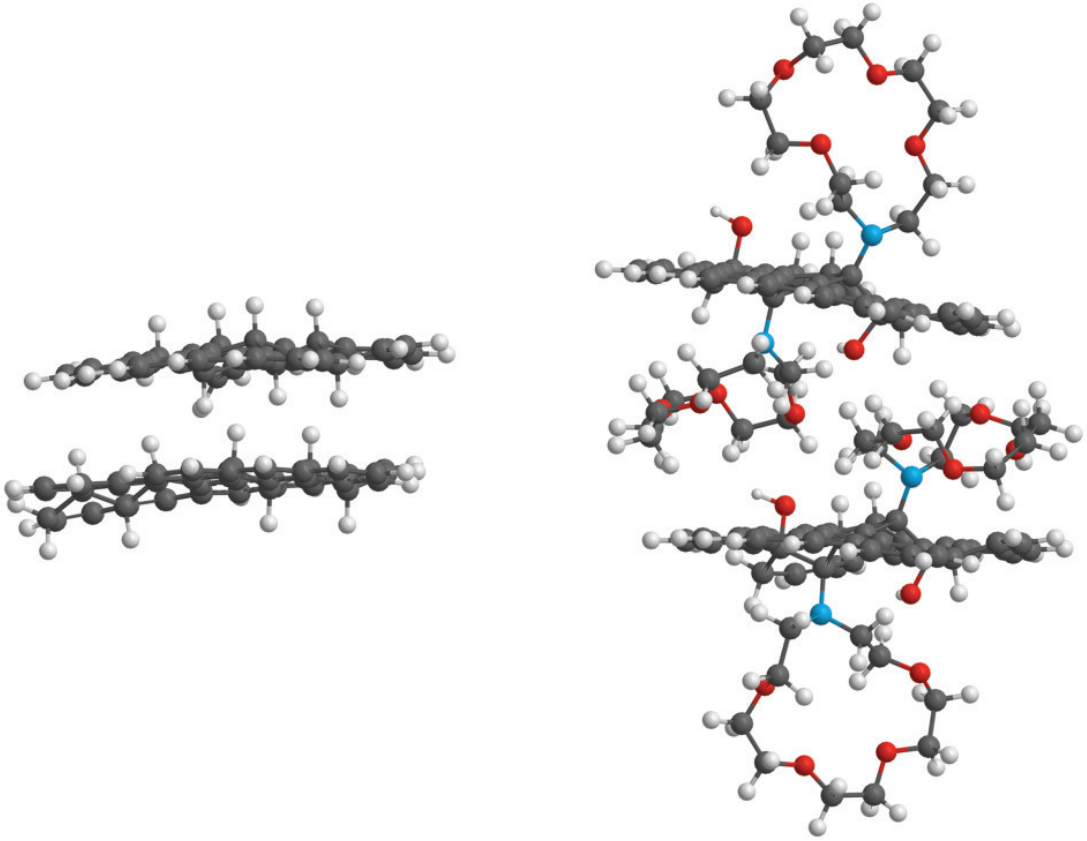

Figure 3.12: Simulation of stacked GO (left) and FGO (right) layers: Carbon atoms in grey, Oxygen atoms in blue, Hydrogen atoms in white and Nitrogen atoms in red. Reprinted with permission from (72). Copyright IOP Publishing.

3.2.3 Electrical characterization and gas sensing performance

GO-based gas sensors have been widely investigated by researchers and the number of publications has increased considerably over the last years. Indeed, its large specific surface area makes GO a promising material for applications where functionality is magnified by the extension of the surface exposed for interaction with the environment. At the same time, the high charge-carrier mobility enhances the transduction of the chemico-physical conditions variation, e.g. as occurs in chemoresistive gas sensors. Contrary to graphene and reduced graphene oxide, widely used for gas sensing applications both as pristine material and in functionalized arrangements (55), GO is proton conductive and hydrophilic, which makes it a promising material for moisture sensing (56, 57). The interaction with certain gases, e.g. water vapour, NO_2 and H_2 (58), can be controlled by tuning the physical properties of GO sheets by reduction and/or chemical functionalization approaches (59). Among eight diverse gases tested at room temperature (methane, acetaldehyde, ammonia, acetone, toluene, ethanol, benzene and humidity), prepared FGO films resulted selective only to water vapours. Figure 3.13a shows the response of FGO 1:1 film at 25% RH in comparison to pristine GO and rGO. Unlike GO and rGO, FGO 1:1 film appears to be selective toward humidity and demonstrated good stability during repeated measurements (Figure 3.13b). The response and recovery times of the tested films, calculated as the time necessary to attain 90% of steady-state sensor response and as the e-folding response, respectively, ranged from 500 to 900 s. The response time exhibited by FGO sensors are comparable with the response time of the commercial HIH-4000 Honeywell capacitive humidity sensor used to control Relative Humidity (%RH) in the test chamber.

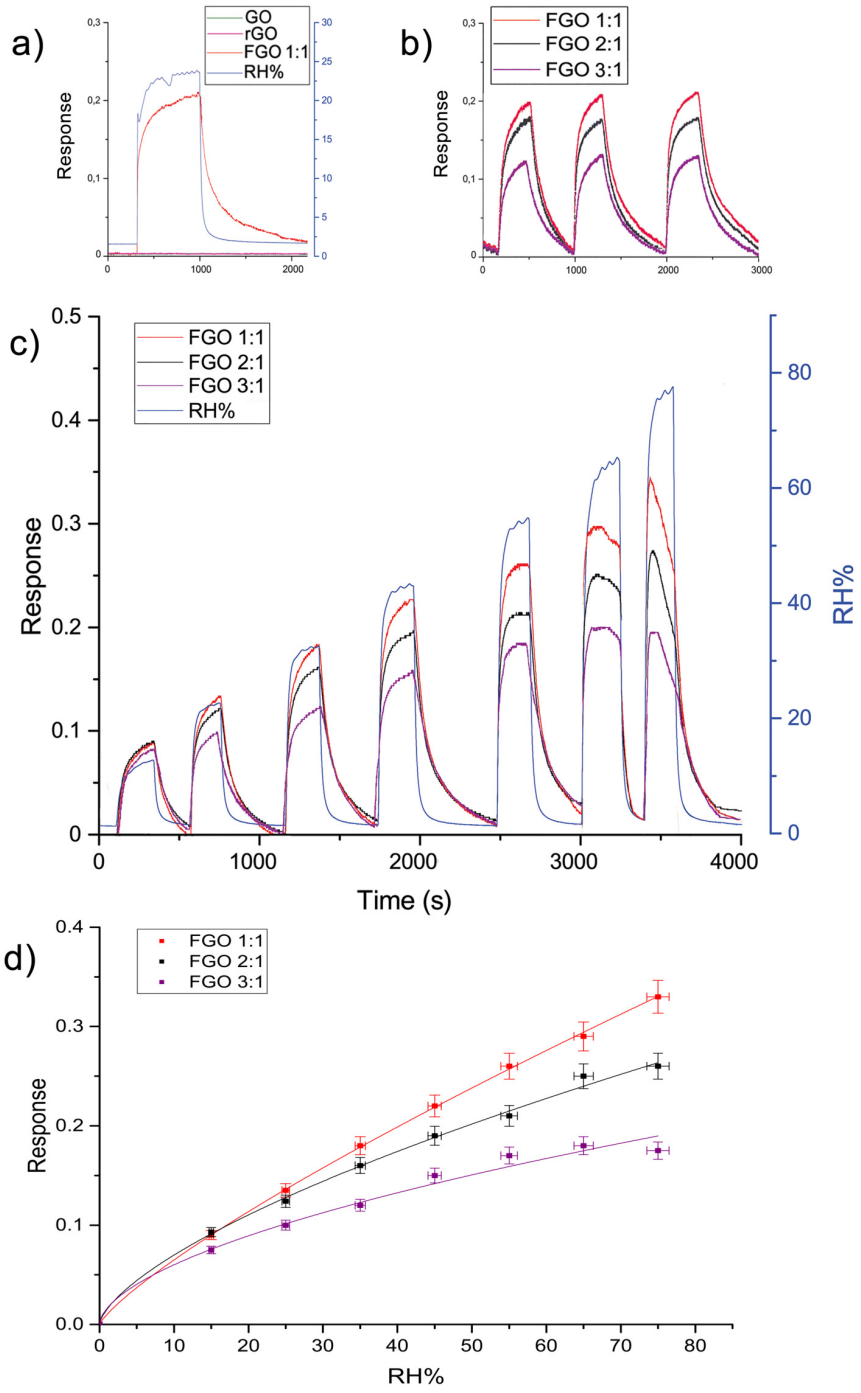

Figure 3.13: Electrical characterization at room temperature of (a) GO, rGO and different GO:1-Aza-15-crown-5 rate devices vs. 25% RH. (b) Stability and complete reversibility of the sensing reaction, (c) Dry-wet cycles from 10% RH to 80% RH. FGO 1:1 based sensor present better stability and sensitivity and (d) humidity calibration curve of FGO sensors. Reprinted with permission from (72). Copyright IOP Publishing.

In order to evaluate the role of the 1-aza-15-crown-5 in humidity detection, different sensing films with different GO:1-aza-15-crown-5 weight rate were produced (Table S1). Figure 3.10c shows the dependence of the sensing performance on graphene:aza-crown-ether rate. Produced FGO devices showed different responses while exposed to a fixed humidity of 25% RH. Among the FGOs synthetized, best performing devices were provided by 1:1 GO:aza-crown-ether concentration rate, confirming that cyclic ether acts as receptor in the sensing mechanism. Functionalization plays a crucial role in improving the sensing performance of the device. Indeed, as it can be seen in Figure 3.13c, at low humidity concentrations all the FGO films exhibit the same sensing trends. On the contrary, by increasing the concentration of water molecules, the sensing films response increases for highest functionalized film (FGO 1:1), since all the active sites of the 1-aza-15-crown-5-ethers tend to become saturated. The stability of the sensing film and the repeatability of its response vs. humidity (Figure 3.13b) were not affected by any memory effects in the material during the dry-wet cycles. The normalized responses of sensors prepared under the same procedure were investigated over a wide RH% range (Figure 3.13c).

The demonstrated high selectivity of the sensing film alongside with room temperature operation without employing any thermo- or photo-activation makes FGO a promising graphene oxide-based gas sensor, even in comparison to those obtained with other functional GO, pure GO or defected graphene films prepared by various methods, not only in the chemoresistive domain (132, 133, 134).

3.2.4 Proposed sensing mechanism

Figure 3.14 illustrates the proposed sensing mechanism of FGO. In our assumption, the interaction between the functionalization and water molecules causes a change in conductance, which is due to hydrogen-bonding interaction via proton-electron exchange between FGO and the adsorbed molecules. Previous deepened study by Carnegie *et al.* (135) demonstrated that the crown-ether structure presents two primary binding sites, both exposed in a Cs symmetry. Theoretically, even an individual water molecule can change the conformational distribution of aza-crown structure. Water molecule(s) take advantage of the oxygen-rich character of the aza-crown ether, donating its OH groups to H-bonds to the crown oxygens. The formation of hydrogen-bonded networks facilitates the rapid transport of protons, in this way, hopping between adjacent water molecules occurs easily employing the Grotthuss mechanism, which can cause an increase of conductance (136, 137). Furthermore, the fact that the aza-crown possesses multiple oxygen sites in proximity to one another raises the possibility that bound water molecules could interact with more than one site simultaneously. Water bonded molecules can interact via H-bond with other water molecules, forming clusters, then affecting still more the film conductance. In addition, with further increase in humidity, the large number of existing functional groups in FGO could aid proton migration between layers. All of these factors would lead to a sudden increase in conductance, leading to a quite high sensitivity humidity sensor.

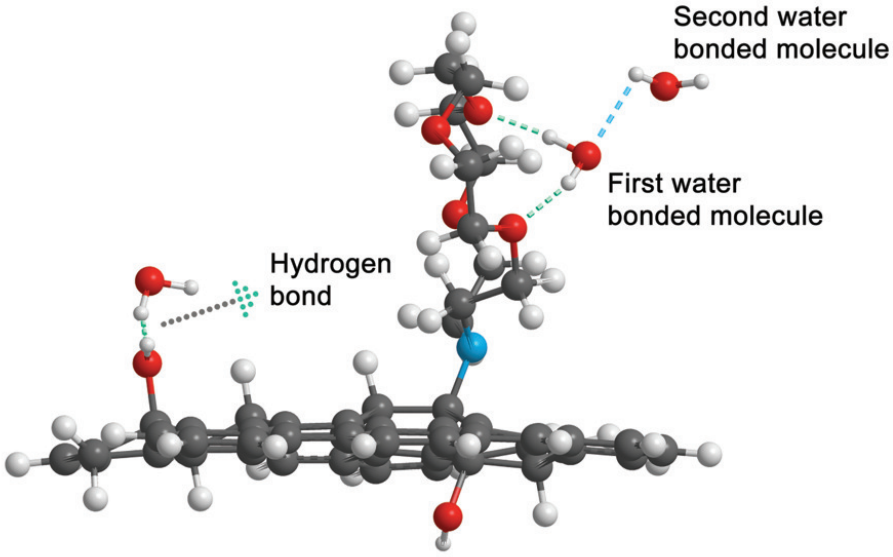

Figure 3.14: Scheme for the humidity sensing mechanism proposed for FGO. Reprinted with permission from (72). Copyright IOP Publishing.

3.2.5 Impact of aza-crown-ether cycle size on the sensing performance

In order to investigate the influence of aza-crown-ether cavity dimension on the sensing performance three different aza-crown-ethers (1-Aza-12-crown-4, 1-Aza-15-crown-5 and 1-Aza-18-crown-6) were used to functionalize GO with the same reaction route presented before. Obtained materials have been deposited by spin-coating onto alumina substrate with built-in interdigitated gold electrodes with the aim of better controlling film thickness. Uniformity of the film has been confirmed by profilometry measurements, with an average thickness of 10 μm.

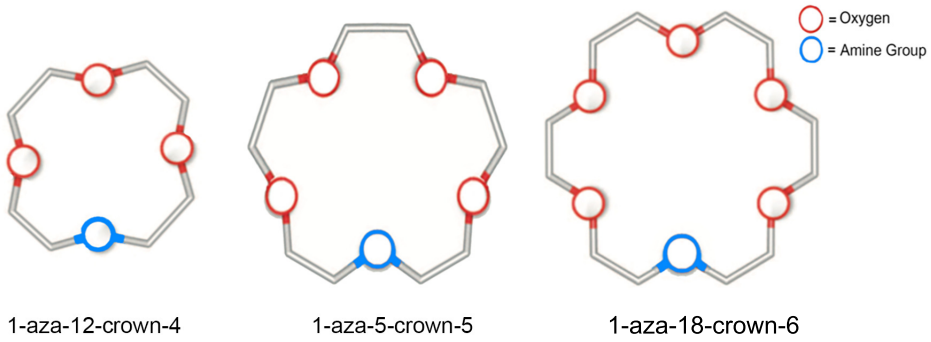

Figure 3.15: Schematic representation of 1-Aza-12-crown-4, 1-Aza-15-crown-5 and 1-Aza-18-crown-6 structure.

As it can be seen in Figure 3.16 and 3.17 sensor response is cavity size dependent. In fact, 1-aza-12 functionalized graphene oxide performed better at low RH% value than 1-Aza-15-crown-5:GO and 1-Aza-18-crown-6:GO composites. This behaviour can be ascribed to the more proximal oxygen sites in the aza-crown moieties that facilitate the H-bonding with water molecules. Further increasing RH% in gas sensing chamber 1-Aza-12-crown-4 based material saturate faster than 1-Aza-15-crown-5:GO and 1-Aza-18-crown-6:GO composites since the availability of oxygen sites is increasing with the functionalities dimensions and active sites concentration.

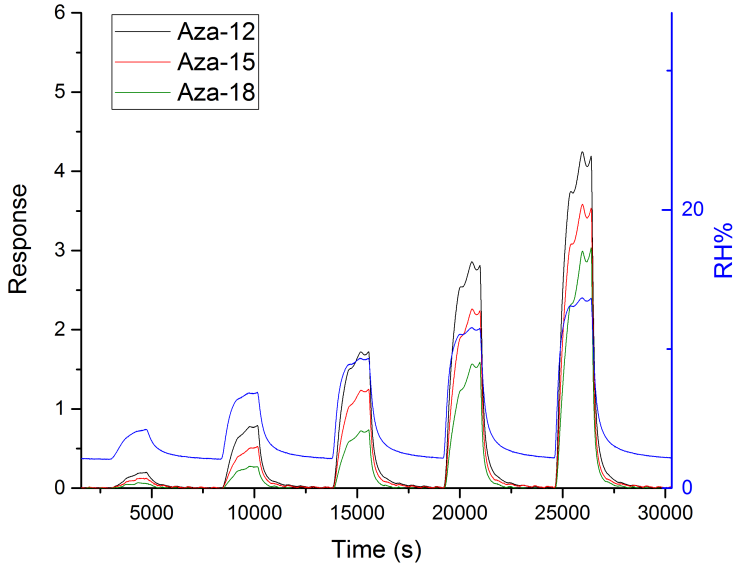

Figure 3.16: Dynamic response at room temperature of GO:1-Aza-12-crown-4, GO:1-Aza-15-crown-5 and GO:1-Aza-18-crown-6 devices vs. different RH% values.

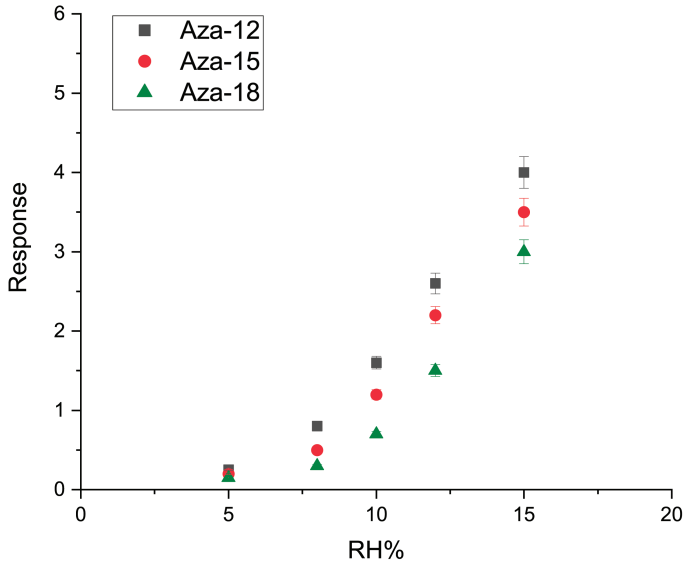

Figure 3.17: Humidity calibration curve of GO:1-Aza-12-crown-4, GO:1-Aza-15-crown-5 and GO:1-Aza-18-crown-6

Chapter 4

Nickel decorated black Phosporous

With the aid of first-principles calculations, a systematic study on binding energy, geometry, magnetic moment, and electronic structure of several metal ad-atoms adsorbed on phosphorene has been carried out, predicting that the immobilization of transition on the surface of phosphorene is feasible, while preserving its structural integrity.(138, 139, 140, 141) Despite the importance of adopting a customized decorating strategy, only few materials, e.g. Au, Pt(119), TiO_2(141) , $SrTiO_3$(142), Cs_2CO_3 and MoO_3(118) have been incorporated into bP. Research has remained confined to the investigation of the carrier concentration and the n- or p-decorating level of bP with a simple device structure. The effects of decoration on the chemoresistive gas sensing ability of a bP system have not been widely investigated. Nickel appears to be a good candidate for bP functionalization due to the first-principles calculated high adsorbition energy (Ea) of -4.09 eV 14 , this value is much larger than Ea of Ni adatoms on graphene (143), and the well-known gas sensing capabilities in various structures and under diverse conditions (120, 144, 145, 146). In this work, made in collaboration with CNR-ICCOM in Florence, by applying a multiscale characterization approach we demonstrated a stability and functionality improvement of Nickel-decorated bP (Ni/bP) films for gas sensing prepared by a simple, reproducible and affordable deposition technique. Furthermore, we studied possible electrical activity of these films for their employment as functional layers in gas sensors by exposing them to different gaseous compounds (NO_2, CO_2, H_2, NH_2, CO, Benzene, ethanol, ethylene, Formaldehyde) in

different relative humidity (RH%) conditions. Moreover, the influence in sensing performance of nickel nanoparticle (NP) dimensions in related to the decoration technique and the film thickness were investigated. In particular, the sensing performance of the films was studied in room-temperature operation mode in order to highlight possible technological advantages for this completely novel application of Ni/bP material.

4.1 Synthesis process

4.1.1 Synthesis of black phosphorus and liquid phase exfoliation.

Crystals of black phosphorus (bP) were prepared according to a published procedure (147). The liquid phase exfoliation was carried out suspending bP microcrystals in dimethysulfoxide under the action of ultrasounds in inert atmosphere. The prepared 2D bP was suspended in dry tetrahydrofuran (4.0 mg/1.0 mL) and was used as a reference in the device later described.

4.1.2 Synthesis of Ni/bP (1). Nickel nanoparticles deposited on bP

To solid $Ni(acac)_2$ (50.0 mg, 0.194 mmol), oleylamine (640 μL,1.362 mmol) and trioctylphosphine (70 μL, 0.152 mmol) were added under nitrogen. The mixture was heated up to 220°C in 15 minutes under nitrogen and kept at this temperature for two hours. Then, to a freshly prepared suspension of few-layer BP in THF (1.2 mL, 1.2 mg, 0.0387 mmol "P") a black colloidal solution of nickel nanoparticles dispersed in toluene (0.29 mL, 0.018 M, 0.00531 mmol "Ni", P/Ni = 8) was added drop-wise under nitrogen at room temperature. After stirring for 30 minutes, degassed acetone (10.0 mL) was added, and the mixture was centrifuged at 8000 RPM for 20 minutes. The black residue was washed once more with acetone (10 mL), dried under a stream of nitrogen and re-suspended in THF.

4.1.3 Synthesis of Ni/bP (2). Nickel nanoparticles grown directly on bP

To a suspension of 2D bP (5.0 mg, 0.161 mmol) in 6.0 mL of dry tetrahydrofuran, 40 mL of dry methanol were added. The suspension is stirred at RT for 10 minutes, after a solution of $NiCl_2$*$6H_2O$ (5.08 mg, 0.0214 mmol) in 255 μL of methanol was added and the resulting mixture was stirred for ten minutes. Afterwards, the addition of $NaBH_4$

as a solid (10.0 mg, 0.265 mmol) turned out the suspension from grey to black and the stirring was kept at maximum speed for five minutes. At this point, the mixture was centrifuged (9000 RPM for 20 minutes), the surnatant was discarded and to the black residue methanol (5 mL) and tetrahydrofuran (2 mL) were added to wash it by another centrifugation cycle. The resulting black solid was dried under vacuum.

4.1.4 Device fabrication

Three samples in suspension of tetrahydrofuran, all with the same concentration, 4.0 mg in 1.0 mL, were used to prepare the films: 2D bP, Ni/bP(1) and Ni/bP(2). The gas sensing films were prepared by dropping 50 μL of each solution and spin coated, at 3000 RPM for 20 seconds, on Al_2O_3 substrates with built-in interdigitated gold electrodes followed by drying at RT for 15 min. The deposition was repeated 4, 8 and 16 times in order to obtain different film thickness. In this way, 3 different films with an average thickness of 2, 4 and 10 μL were prepared, film thickness was measured by the means of a KLA-Tencor P-6 stylus profilometer. The sensor substrate was subsequently packaged on commercially available TO-39 support via thermo-compressing bonding for electrical characterization.

4.2 Characterization

TEM analysis showed well-dispersed nickel nanoparticles on the surface of black phosphorus nanosheets for both the synthesis. After immobilization, Ni nanoparticles preserved their size, average diameter of 11.9±0.8 nm for Ni/bP (1) and 3±0.8 nm for Ni/bP (2). Moreover, no aggregation took place.

On the same sample AFM was measured. Looking at smaller structures, which are likely to be single flakes or few flake-aggregates, see Figure S11 (ESI), we found their typical size to be a few hundred nanometers, and their thickness up to 50 nm. A typical flake is shown in Figure 6(a), and two cross-sections are shown in Figure 6(b) and (c). Knowing that a single Ni nanoparticle has a diameter around 12 nm, and using the same approximation as in Hersam's paper (149) we can roughly estimate the BP flake thickness. The object in Figure 6(a), with a thickness of 14–32 nm, corresponds to a BP flake thickness of 2–20 nm, and having the BP layer spacing of 0.53 nm, the number of layers ranges from 4 to 38.

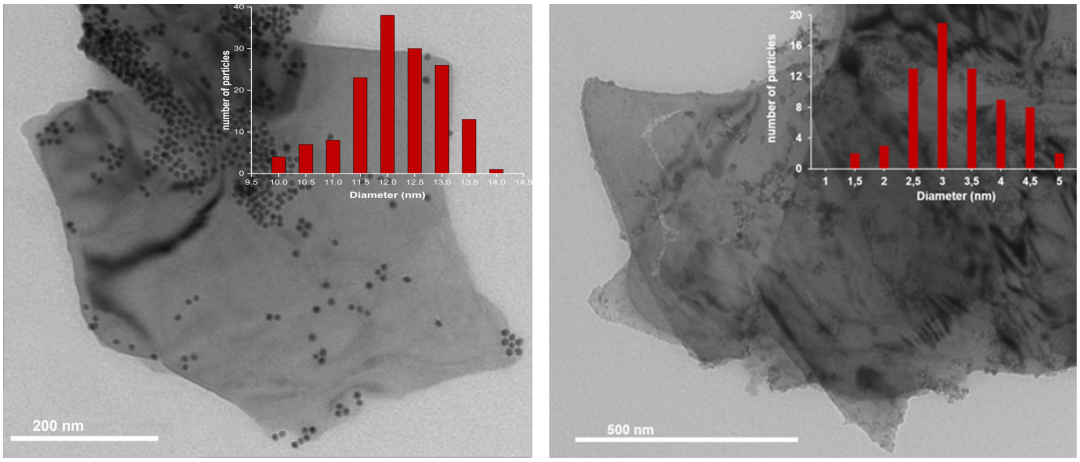

Figure 4.1: TEM image of Ni/bP (1) (Left) and Ni/bP (2) (Right) supported on few-layer black phosphorus, P:Ni molar ratio 8:1. Inset: Size distribution histogram of Ni NPs. Reprinted with permission from (148) Published by The Royal Society of Chemistry.

The new nanohybrid was further characterized by Raman spectroscopy. Figure 4.4 compares the Raman spectrum of a freshly prepared sample of 2D BP (blue curve) with the same batch of 2D BP after functionalization with nickel nanoparticles (red curve). The spectrum of the nickel functionalized material reveals the three typical Raman bands of black phosphorus at 360, 435 and 460 cm^{-1}, attributed to the $A^1{}_g$, B_{2g}, and $A^2{}_g$ vibrational modes respectively,(150) confirming the orthorhombic crystalline structure of 2D BP. Since nickel is silent in Raman, the crystalline nature of the nanoparticles was confirmed by SAED and powder XRD, see Figure 4.3 and 4.5, which showed that the nanoparticles have the characteristic cubic face centred structure of crystalline nickel.

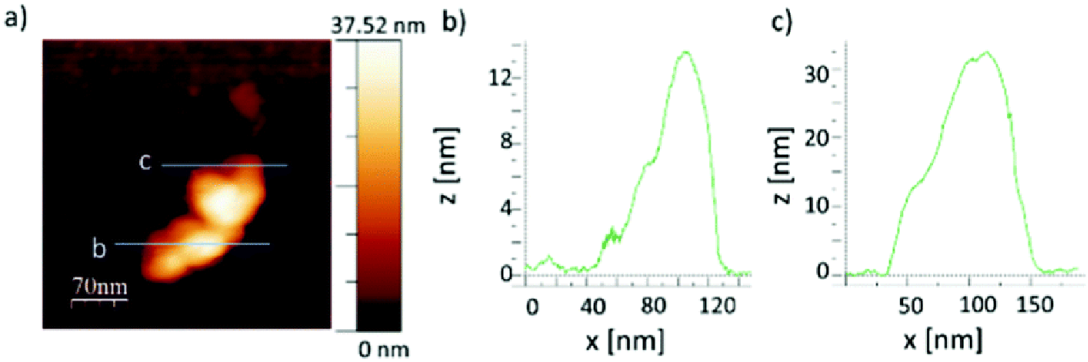

Figure 4.2: (a) AFM image of a typical flake and (b and c) profiles along the two lines displayed in (a). Reprinted with permission from (148) Published by The Royal Society of Chemistry.

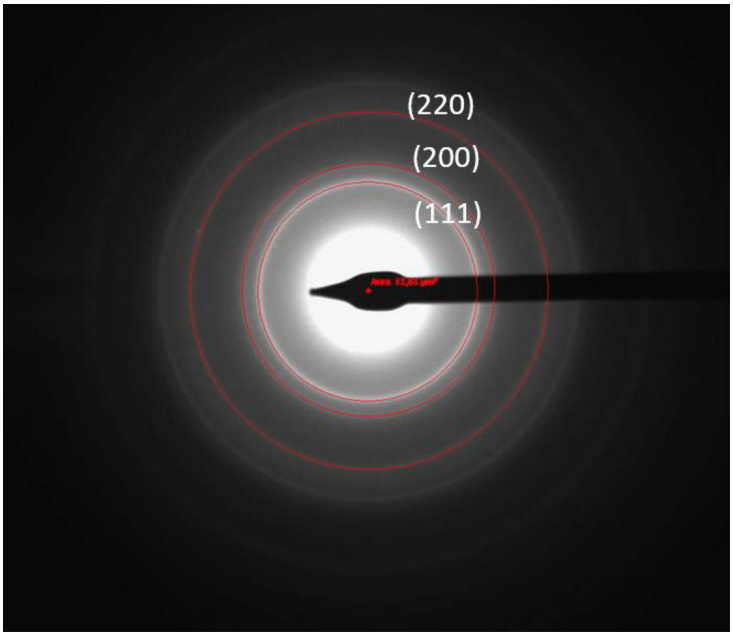

Figure 4.3: SAED (selected area electron diffraction) pattern of Ni NPs. The diffraction rings correspond to face-centered cubic nickel. Reprinted with permission from (148) Published by The Royal Society of Chemistry.

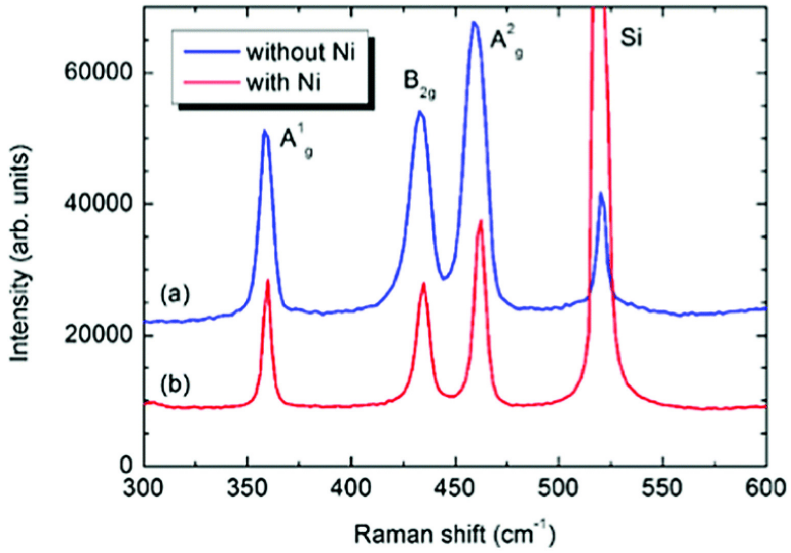

Figure 4.4: Comparison of the Raman spectra between (a) pristine few-layered bP (blue curve) and (b) Ni/bP (1) (red curve). The strong peak at 520 cm^{-1} is due to the silicon substrate.

Powder X-ray diffraction of Ni/bP (1) (Figure 4.5) shows the characteristic peaks of black P and additionally a broad peak at 2θ equal to 44.41° revealing the presence of nickel NPs. The other peaks at 51.81° and 76.41°, also characteristic of nickel, are too weak to be identified. Thus, the surface functionalization with Ni NPs did not affect the structure and the crystallinity of 2D bP.

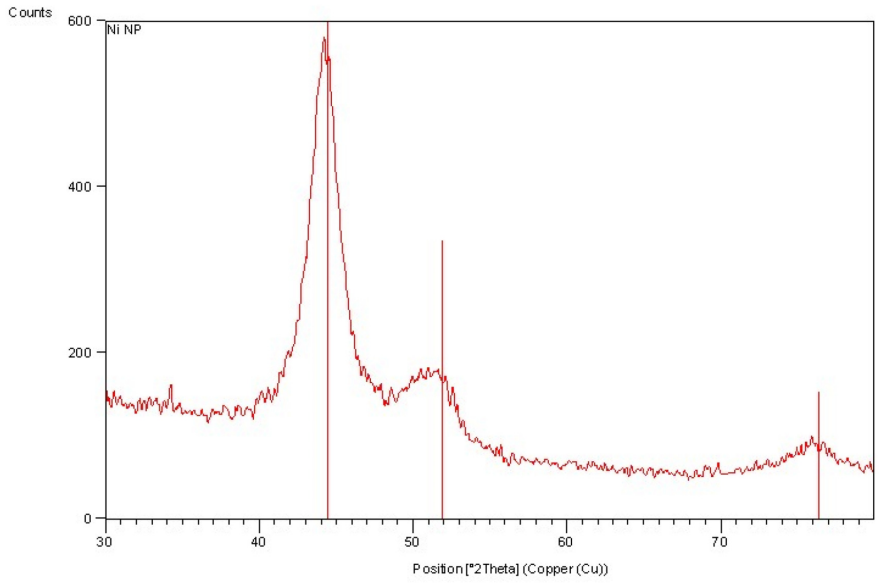

Figure 4.5: Powder X-Ray diffraction of Ni NPs. Reprinted with permission from (148) Published by The Royal Society of Chemistry.

4.3 Gas sensing performance

To determine the effects of decoration on the gas sensing properties of Nickel decorated bP, the conductance variation of the films was investigated as a function of the Ni nanoparticle dimensions, direct consequence of different employed decoration technique, and compared to pristine bP. The measured conductance in dry air (Figure 4.7a) for the prepared films (4 μm-thick) was 2.26 $\cdot 10^{-4}$ μS for pristine bP, 2.2$\cdot 10^{-2}$ μS for Ni/bP (1) and 1.29$\cdot 10^{-3}$$\mu$S for Ni/bP (2). The introduction of Ni nanoparticles increases carrier mobility of the film with further increase in conductance in the nanocomposite system, a desirable quality for any functionalized material for gas sensing application. The increase in the electrical conductance in function of the diameter size of the Ni nanoparticles is probably related to conformational change in the bP induced by nanoparticles formation. The dynamic sensing responses of pristine bp, Ni/bP (1) and Ni/bP (2) based sensors were investigated exposing the devices to several gaseous mixture in air at room temperature (methane, acetaldehyde, ammonia, acetone, ethanol, ethylene, benzene, nitrogen dioxide, carbon monoxide, carbon dioxide, sulfur dioxide and hydrogen). Among diverse gases tested, prepared Ni/bP nanocomposite demonstrated a high sensitivity and selectivity only toward NO_2 with a Low Detection Limit

of 100 ppb, whereas pristine bP sensor exhibited a negligible response to all tested gases. Fig 4.7a shows the dynamic response of Ni/bP(1), Ni/bP(2) and pristine bP with various concentration of NO_2.

As previously reported, pristine bP can exhibits a sensitive response to NO_2 and many researchers have theoretically predicted and experimentally observed that the adsorption of the NO_2 molecules on the bP surface can take place via non-covalent interactions (111). However, stacked layers of 2D pristine bP, with 5 Å interlayer distance, can be considered as a porous system. In this way, the number of active sites of the material is significantly reduced and, alongside with the fast and severe degradation process occurring under employed ambient conditions, makes pristine bP difficult to use in real life applications. Furthermore, Nickel decorated bP exhibited a highly stable baseline resistance with ultralow noise level (≈0.002%) and response only to NO_2 with a positive conductance variation. The baseline noise level is drastically improved with Ni/bP (2) compared to that of Ni/bP (1) (≈0.4%) and pristine bP (≈ 0.25%).

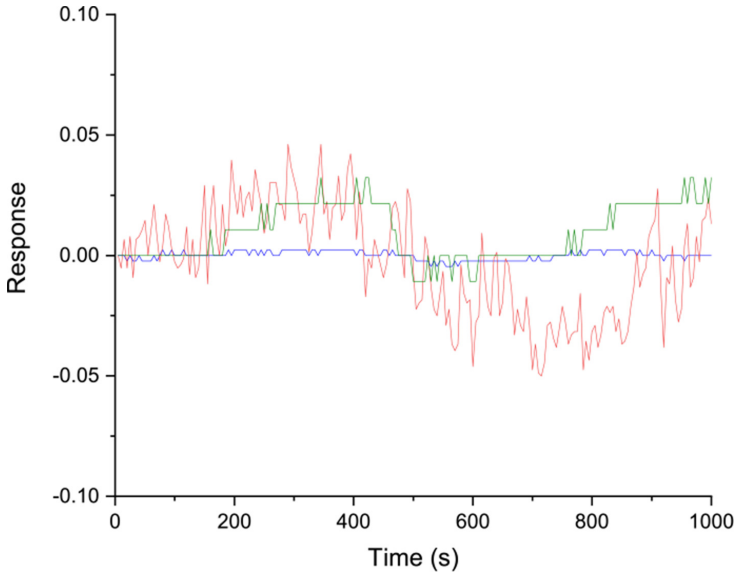

Figure 4.6: Baseline noise level of bP, Ni/bP (1) and Ni/bP (2) devices in dry conditions

Functionalization with Ni induced significant chemical sensitization of the bP surface for the sensing of NO_2 molecules caused by the highly catalytic properties of Ni. The slow and incomplete recovery of the base line, showed by Ni/bP (1), was previously observed in few layers reduced graphene oxide(151) and, recently, for few layer

phosphorene in both dry air and N_2 atmosphere (112, 152). Indeed, as reported in (112, 153) the existence of irreversible sites where target gas molecules may strongly bind, physically represented by defects, inhibits a complete desorption in the time scale of a sensing cycle. The response and recovery times of these films, calculated as the time necessary to attain 90% of steady-state sensor response and as the e-folding response, respectively, ranged from 25 to 40 min. Therefore, the characteristic times of Ni/bP-based sensors are perfectly comparable to those of other bP-based gas sensors (111, 112).

The calibration curve shown in figure 4.7b display Ni/bP(1) and Ni/bP(2) response versus NO_2 gas concentrations. The presented plot show typical fit with Langmuir Isotherm for molecules adsorbed on a surface (111) further suggesting that charge transfer is the sensing mechanism for NO_2 sensing in multilayer bP based devices. Moreover, in order to investigate the influence of humidity in the response, sensors have been exposed to different RH% conditions (from 2% up to 60%) to 1 ppm of NO_2 (Fig 4.7c). Ni/bP (2) based sample show a small decrease of the response value with RH% increasing highlighting good humidity resistance. On the contrary, Ni/bP (1) film showed a rapid decline in sensing performance and an irreversible degradation of the film at 30%RH, for 60RH% measure a twin device has been used and irreversibly compromised after the water vapours injection. In order to demonstrate the stability of these sensors and investigate the influence of the film thickness in the sensing performance, three sensors (2, 4 and 10 μm thick), based on each Ni-decorated bP film, were produced and tested with 1 ppm of NO_2 for a four weeks period in dry condition (Fig 4.7d). The conductance in dry air highlights an inverse correlation between film thickness and conductance value. Interestingly, despite the initial higher response, the Ni/bP (1) material suffers performance degradation only after one week under a dry air flux, this phenomenon is impeded and slowered in thicker films. Ni/bP (2) highlight better stability over the measurement period, and after several months, even if the response value is well below the Ni/bP (1) initial one. A possible explanation of the aforementioned behaviour resides in the morphological characteristics of the employed materials. In particular, nickel nanoparticles in Ni/bP (1) present an average diameter of 12 nm, which increases the interlayer separation with respect to Ni/bP (2) which possess a four times smaller diameter of $\approx$3 nm avoiding, in this way, the restacking of bP sheets. This fact drastically enhances the specific surface area exposed

to NO_2 in the case of Ni/bP (1), resulting in a more effective initial sensor response. On the other hand, this separation exposes a more extended sensing area to ambient adsorbates which, as suggested by Wood et al (153), irreversibly react with bP forming oxidized phosphorus species compounds (PO_x), fundamentally altering electronic and material properties of bP. Moreover, in situ grown Ni/bP (2) shows stable response during all the four weeks measurements period with no dependence of the response on the film thickness. Ni decoration effectively suppress ambient degradation, for at least 1 week in Ni/bP (1) and over 4 weeks in Ni/bP (2) in ambient conditions. This result highlighted that Ni/bP (2) sensor can be practically used under ambient conditions for a reasonable period without performance degradation of the devices.

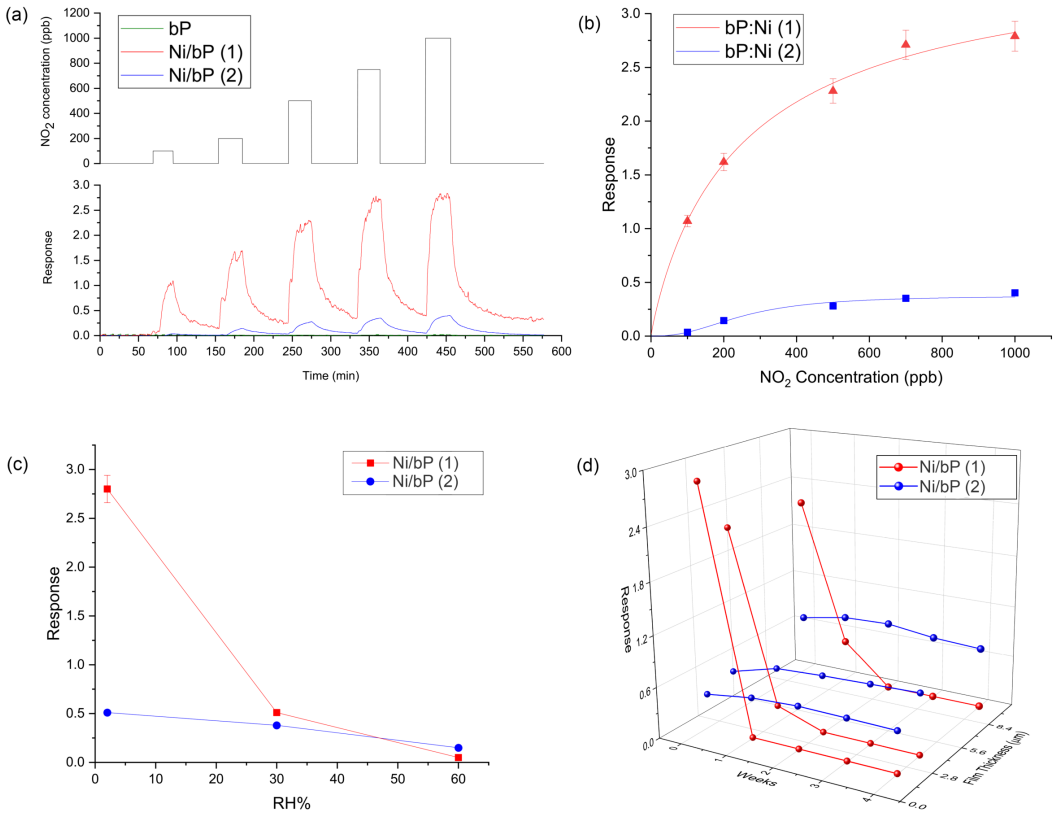

Figure 4.7: Electrical characterization at room temperature of (a) bP, Ni/bP (1) and Ni/bP (2) devices in dry conditions with five different concentration of NO_2. (b) Calibration curve of Ni/bP based sensors (c) Response to 1 ppm of NO_2 at different RH% values, (c) Response values for different thickness of the film during a four-week testing to 1 ppm of NO_2 in dry condition.

4.3.1 Proposed sensing mechanism

By using adsorption chemistry on Nickel decorated bP composite surface it is possible to propose a sensing mechanism in order to understand the change in conductance in presence of NO_2. After Ni decoration of bP surface, the sensor response to NO_2 gas molecules is markedly enhanced with respect to pristine bP-based sensor and the gas sensing mechanisms involved are supposedly different. It is reasonably to assess that NO_2 molecules interact more intensively with Ni and the synergic effect with bP plays an important role in sensing performance. In our assumption Ni atoms act as a catalytic reaction centre in the reaction with NO_2 molecules at surface. The adsorption of NO_2, which is an oxidizing gas, on the Ni nanoparticles leads to the formation of NO^{2-}. This process traps electrons from the conduction band or the donor level of the nanocomposites, which leads to an increase of hole density that finally results in an increase of conductance. First, the oxygen molecules from the air is chemisorbed on the Ni surface. After this first interaction, the chemisorbed O_2 molecules can react with the electrons at surface and transform into O^{2-} at RT, thus decreasing the concentration of electrons at surface and forming a depletion layer. As follows:

$$O_2(\text{ads}) + e^- \longrightarrow {O_2}^- (\text{ads})$$

Then, the generated oxygen adsorbent (O_2) at the Ni surface, when exposed to an oxidizing gas (NO_2), the co-adsorption and mutual interaction between the gases and the adsorbed oxygen result in reduction at surface and a decrease in the chemisorbed oxygen concentration. This process is represented in equations:

$$NO_2(\text{ads}) + e^- \longrightarrow {NO_2}^-(\text{ads})$$

$$NO_2(\text{gas}) + {O_2}^-(\text{ads}) \longrightarrow {NO_2}^-(\text{ads}) + O_2(\text{gas})$$

The desorption process can be controlled by the surface desorption related to the binding energies reported in Kou et al. (110) and/or by the desorption of the NO_2 molecules previously diffused between the nanocomposite layers. It is reasonable to assume that the fastest process involved is the surface desorption, being related just to

the charge transfer. Therefore, it is very likely that NO_2 slow desorption rate is principally dependent on the diffusion phenomena inside material layers. When the sensing film is exposed to the gas, the NO_2 molecules tend to diffuse between the bP layers and the interlayer desorption results in slower process than the one from the exposed Ni/bP surface. This behaviour has been reported for pristine bP sheets and in other similar 2D systems like graphene.(154) Therefore, we think that the enhanced sensing properties of the Ni/bP nanocomposites should be attributed to the synergism between bP and Ni nanoparticles. Compared with pristine bP, the active sensing area of the Ni/bP was increased. According to the literature reported in recent years, a relatively weak and unstable sensing response is the challenge when employing 2D materials alone for high performance sensing applications. Composites of inorganic materials and bP as gas sensing materials have demonstrated good response for the detection of NO_2, H_2 (112, 119). In our case, the Ni nanoparticle growth on bP plays a crucial role as active center in the charge carrier trans-mission to adsorb NO_2 molecules with strong electron-withdrawing power. The electron transfer from bP via Ni nanoparticle to adsorbed NO_2 molecules produces a hole enrichment in p-type hole-transport-driven composite and con-sequently increase its conductance. In the same gas environment, the sensing performance was enhanced with increased effective adsorbance of NO_2 for the chemoresistive gas sensor. This means that the effective load of Ni on bP could affect the response of composites to NO_2. The scheme of the proposed gas sensing mechanism is shown in Figure 4.8.

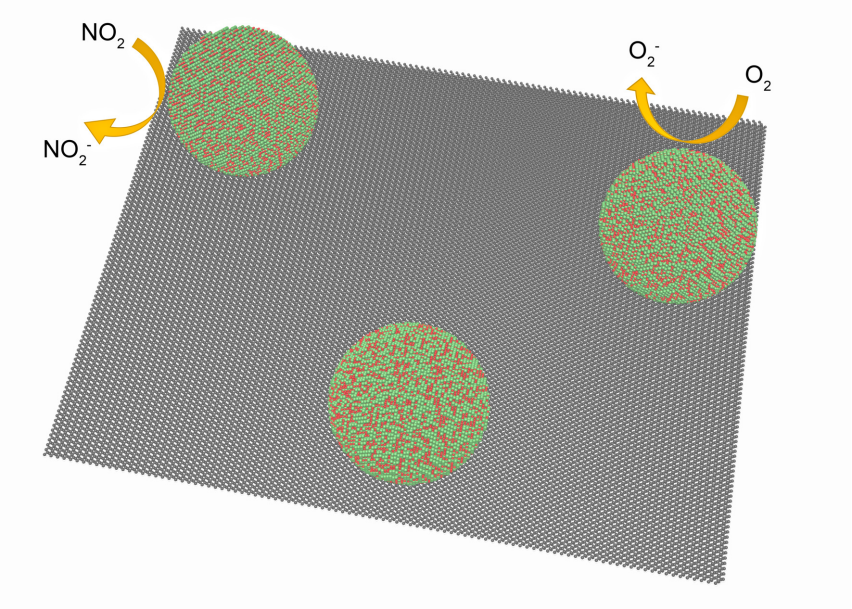

Figure 4.8: Schematic representation of the proposed NO_2 sensing mechanism for Ni/bP Nanocomposite

Chapter 5

Conclusions and future perspectives

This PhD thesis work, carried out at the Department of Physics and Earth Sciences of the University of Ferrara, is focused on the exploration of the fascinating properties of some 2D materials in the field of chemoresistive gas sensing. Their outstanding morphological and electronic properties have been widely investigated and their exploitation leads to the fabrication of many types of gas sensing devices, in order to detect different gases. Gas sensors based on 2D materials have demonstrated high sensitive detection of different gas molecules at low concentrations, due to the maximum sensor surface area per unit volume, low noise and superior ability to screen charge fluctuations compared to conventional systems, in addition to their favourable electrical properties for gas adsorption. Even though pristine graphene, GO and rGO present a very promising gas sensing platform for room temperature gas detection, they get strongly affected by a range of different gas species and also suffer from slow recovery and poor electrical stability under different environmental conditions. Chemical modification of graphene or graphene oxide, functionalized with defects, dopants, metal, metal-oxide nanoparticles and organic compounds have proven to provide promising solutions for improving the sensing performance with high specificity, enhanced sensitivity and low detection limit.

Towards this direction, it was presented an innovative method to homogeneously decorate graphene with Nb_2O_5 nanoparticles by the means of an RF magneton sputtering instrument equipped with a powder mixing system. Nb_2O_5/graphene showed good sensing properties with a low detection limit of 100 ppb towards NO_2 at room

temperature in both dry and wet air conditions. Moreover, synthesis procedure, characterizations and structure simulation of 1-aza-15-crown-5 ether FGO with a high coverage of crown-ether functional molecules has been proposed. With the aim of exploring the physical and chemical properties of the material, in particular the reversible and controlled interaction of the surface with diverse chemical species, we employed FGO in two different fields of application, both exploiting the highly specific properties of the employed functionalization. A gas sensing device, by depositing FGO onto alumina substrates via drop casting technique, was produced. The films showed chemoresistive behaviour with relevant selectivity to humidity and fast response time. A humidity sensing mechanism based on H-bond interaction between the film and water molecules has been proposed. The sensing unit holds all the fundamental properties for a good-quality gas sensor, and makes them competitive with respect to the traditional MOX sensors. Furthermore, the FGO sensors accomplish sensing performance at room temperature without employing any thermo- or photo-activation stimulation to attain full reversibility of the sensing process occurring at surface. Finally, FGO has been functionalized with different aza-crown-ethers in order to further understand the role of the functionalization moieties in the humidity sensing mechanism. FGO was also tested as potential multifunctional material in cation sorbent application (Appendix A) with a simple, time-efficient and reagent-saving method. The results highlighted possible usage of FGO as a filter for heavy metals polluted water or preconcentrator of trace amount of metals. In this way, any additional treatment, such as the elution of analytes, is unnecessary, thereby reducing the sources of contamination as well as the sample preparation time. Using FGO may be an efficient alternative to the classical sorbent such as active carbon. Indeed, the conducted studies reveal the great potential of FGO towards Ni(II), Cu(II), Cr(III) as excellent sorbent material in analytical chemistry. The method proposed in aza-crown-ether functionalization of GO is quite flexible. Indeed, with an appropriate selection of specific crown ethers, it is possible to tailor molecules with cavities whose size, shape and donor properties would allow the capture of any desired guest in order to prepare a wide range of other crown-ether-GO nanocomposites for gas sensing as well as sorbent materials.

The desorption of gases on 2D materials such as rGO, MoS_2, phosphorene, etc., is observed to be slow due to the strong adsorption of gas molecules on these materials, which usually require external assistance such as UV light exposure or high temperature

annealing after gas exposure. This drawback of 2D material based gas sensors, which limits their practical use need to be addressed as it degrades the sensing performance in terms of sensitivity, detection limit and repeatability.

Most of the gas sensing experiments already reported using 2D materials had to be performed under a controlled environment, as the sensitivity values were found to be affected by the presence of other gases in practical environmental conditions. Hence future works need to concentrate on achieving ultra-high selective gas sensing devices under practical conditions using 2D materials. This issue can be addressed by modification of the material surface with suitable modifiers such as metal or metal oxide nanoparticles. The functionalization scheme could be extended to TMDs and phosphorene, which had already proven to be highly successful for graphene based materials. Exfoliated black phosphorus nanoflakes decorated with nickel nanoparticles (Ni/bP) have been prepared and characterized with particular attention to the role of Ni nanoparticle dimension in the sensing mechanism. Electrical activity towards different concentrations of NO_2 at RT in a dry air environment highlighted fast and stable response over the time. This latter characteristic is particularly relevant since environmental instability of exfoliated BP has been an issue so far, under ambient conditions few-layer bP degrades completely in less than a week, preventing its applications in several fields.

This thesis work has explored different approaches in the use of 2D materials as a building block for the synthesis of completely new nanocomposites. The employment of these materials as gas sensing films has been proved for real life applications with room-temperature operation and high selectivity maintained over the time.

In conclusion, the results of this thesis envisage great potential for further refinement and investigation in order to fabricate gas sensors satisfying the 3S: sensitivity, selectivity and stability. In these last years, many researchers pave the way to the fabrication of 2D materials-based gas sensors, suggesting that they can substitute metal oxides gas sensing devices. The deep understanding of the gas sensing mechanisms, with the help of theoretical calculations and in-situ operando analysis, can help to design and produce more selective 2D materials-based gas sensors.

First-principles calculations on the adsorption of gas molecules using different 2D materials could enable the identification of the suitable modification of these materials for enhanced sensor performance. The gas sensing mechanisms of devices based on

newly discovered 2D materials are not completely explained till now. Once the above mentioned shortcomings are addressed, 2D materials could revolutionize the field of gas sensing so that they could emerge as ideal sensing elements with ultrahigh sensitivity, surprisingly high selectivity, fast response, good reversibility, room temperature operation, outstanding stability, etc., for gas sensing systems in the near future.

The effect of the humidity on the responses needs to be minimized and the response stability through months is a crucial point for the fabrication of everyday life sensors. 2D materials can degrade and oxidize in ambient air (phosphorene and WS_2, for example, can oxidize at RT and their responses can change through days of operation). Therefore, capping the 2D materials with metal oxide, or polymers films, can prevent this effect.

Lack of large scale manufacturing of 2D materials with large area, high and uniform quality is yet another challenge. Flexible electronics could benefit from the mechanical compatibility of 2D materials with the device fabrication due to their excellent mechanical properties. 2D heterostructures obtained by the combination of different 2D materials provide a suitable sensing platform for developing future wearable electronics. Modelling of nano sensing devices based on 2D materials is receiving great importance now-a-days, as it could enable the study of underlying sensing mechanisms and the analysis of the sensor performance before going for expensive experimentation.

Appendix A

Multifunctional capabilities of FGO

A.1 Cation trapping measurements

The use of graphene oxide as a ionic membrane was developed by Nair *et al.* (154). Indeed, graphene-based materials have recently emerged as potential candidates for heavy metal absorbent (155) and desalinator with excellent characteristics (131, 156, 157). FGO synthetized in this work combines the high affinity for cations of the aza-crown-ether, that could not be used as is owing to its solubility in water, with the mechanical properties of graphene oxide. Indeed, it is well known that crown ethers form strong bonds with certain cations, generating chemical complexes (158, 159, 160). The oxygen atoms are well situated to coordinate with a cation located inside the ring thus the denticity of the polyether influences the affinity of the crown ether vs. various cations, as schematized in Figure 3.12. We tested the absorbent capabilities of FGO and pristine GO with some cations of environmental interest, such as Ni(II), Cu(II) and Cr(III) by the means of Total Reflection X-Ray Fluorescence (TXRF) analysis, measuring the cation concentration before and after interaction with the FGO membranes in aqueous solution.

For cation trapping measurements 10 mg of GO and 10 mg of FGO were placed in different test tubes, each one containing a 10 mL solution of one of the following cations: Cu(II), Ni(II) and Cr(III), all at the nominal concentration of 40 ppm. Then, through a centrifugation process of 30 minutes at 5000 rpm, GO and FGO materials

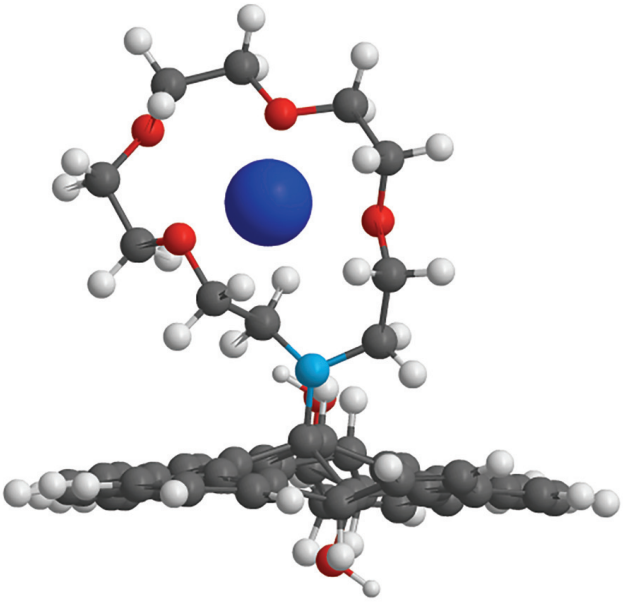

Figure A.1: Schematic rapresentation of FGO sorbent capabilities. Reprinted with permission from (72). Copyright IOP Publishing.

were separated from the suspension. 0.01 mL of an internal standard solution (Gallium 1000 ppm) were added to 0.99 mL of the supernatant solutions for each samples. TXRF was used to quantify the amount of cations before and after the interaction with GO and FGO at Micro Nano Facility of Bruno Kessler Foundation.

TXRF analyses were carried out to quantify the amount of three selected cations via internal standard method, using Gallium as reference, on initial sample and after its interaction with GO and FGO 1:1.

The amount of cations for every sample solution was determined by:

$$c_{\mathrm{i}} = \frac{I_{\mathrm{i}} \cdot c_{\mathrm{s}}}{S_{\mathrm{i}} \cdot I_{\mathrm{s}}}$$

where c_{i} is the cation concentration (ppm), I_{i} is the count number of the cation of interest, c_{s} is the concentration of the internal standard (10 ppm), I_{s} is the count number of the internal standard and S_{i} is the relative sensitivity.

Figure A.2 shows the energy spectrum of one of the performed measurements on Cr(II) containing solution. The energy of the peaks identifies the elements present in the sample by their characteristic K_{α} and K_{β} emission lines, whereas the intensity of

the peaks is strictly related to the cation concentrations. Reference internal standard peaks of Gallium are easily recognizable, $K_\alpha \approx 9250$ eV and $K_\beta \approx 10250$ eV. Indeed, peaks at ≈ 5400 eV and ≈ 5900 eV correspond to K_α and K_β of the Cr(II) emission lines, respectively.

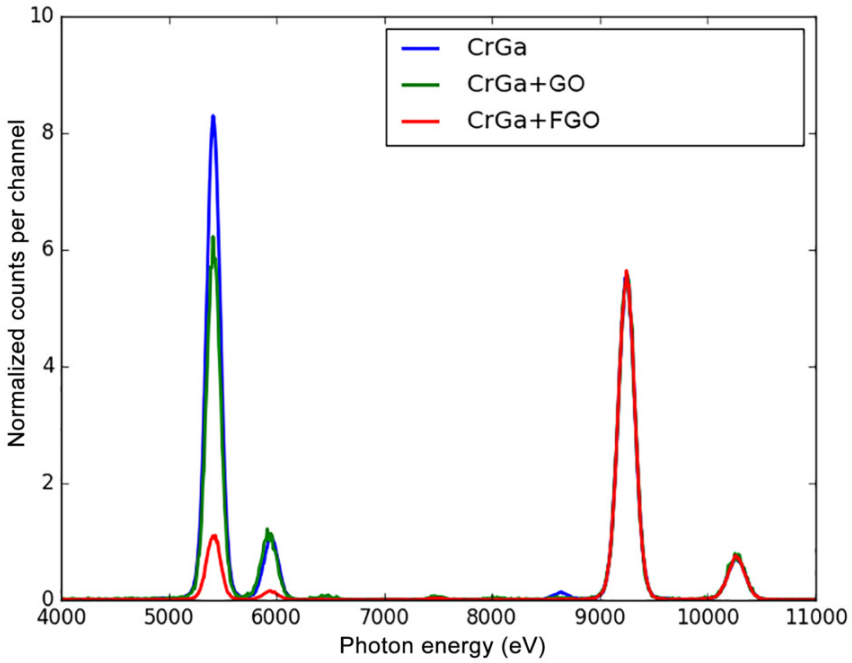

Figure A.2: TXRF analysis of trapped Cr(II) sample in GO and FGO.

Table A.1 reports TRXF analysis results, i.e. the cation concentrations before and after the interaction with GO and FGO 1:1 materials. The nominal cation concentration was 40 ppm for each solution, whereas the real values were slightly different. The percentage recovery for GO and FGO 1:1 were 45.0% and 99.4% for Cu(II) solution, 32.4% and 96.0% for Ni(II) solution, 22.8% and 86.5% for Cr(II) sample. In each sample GO layer plays a role in cation adsorption (155), but a comparison between GO and FGO 1:1 highlights an outstanding activity of the aza-crown-ether moieties. Indeed, the absorption capability of the adduct is more than the double with respect to our tested pure GO.

Table A.1: Concentration (ppm) of the initial experimental cation solutions, pristine GO and FGO 1:1 after treatment.

Sample	Cu (ppm)	Ni (ppm)	Cr (ppm)
Initial solution	43.05 ±0.01	37.52 ±0.20	41.74 ±0.04
GO	23.67 ±0.01	25.36 ±0.19	32.22 ±0.05
FGO 1:1	0.24 ±0.01	1.51 ±0.19	5.62 ±0.05

The remarkable stability of crown ether complexes with cations is enthalpic in origin (161). However, such a complex system depends on various factors. Stability decreases in the same order as electronegativity of heteroatoms included in the cycle. Moreover, cation affinity of aza-crown ethers depends on the type of substituent attached to the nitrogen, GO in our case of study. In order to explain the different behaviour of FGO 1:1 in sorbtion capability, it is useful to apply to the utilized transition metals the "hard and soft acids and bases" (HSAB) theory (162) and taking into account the cation valence. Within the same category of cations, the most stable complexes are formed when the ratio of cation size and cavity diameters is close to one. Any deviation from the perfect fit results in a loss of stability and, consequently, in a loss in binding capacity (158). For Ni(II) (0.166 nm of ionic diameter) and Cu(II) (0.174 nm of ionic diameter), the ratio of cation diameter over aza-crown cavity (whose size is $\approx$ 0.175 nm), corresponds to 0.948 and 0.994, respectively. In this way, the better affinity of the aza-crown moieties for Cu(II) with respect to the Ni(II) cations is well justified. The behavior of FGO with an "hard" cation like Cr(III) is different from that with "intermediate" cations, as Ni(II) and Cu(II). This evidence demonstrates the better affinity of the aza-crown site of FGO for relatively easy polarizability of transition metal cations, since cation-dipole interactions are thought to provide the binding energy of crown-ether complexes with "hard" cations. Prepared FGO material showed excellent results in cation adsorption capabilities, as can be seen in Table A.2 FGO sorbing performance are comparable with other carbon-based nanomaterials for determination / preconcentration of metal ions. Moreover, the direct interaction between the cations and the sorbent material allows one to reduce the time of sample preparation in comparison with a classical Solid Phase Extraction (SPE) method (163).

Table A.2: Comparison of the presented method with published procedures based on solid-phase extraction and determination of Cr, Cu and Ni ions.

Sorbent	Method	Element	Recovery, %	Ref.
GO	EDXRF	Ni(II)	94	(164)
		Cu(II)	97	
GO-EDA	EDXRF	Ni(II)	93	(165)
		Cu(II)	96	
GO-Gly	EDXRF	Cr (III)	98	(166)
		Cu(II)	99	
FGO 1:1	TRXF	Cu(II)	99.4	This work
		Ni (II)	96.0	
		Cr (III)	86.5	

References

[1] C. Wagner and K. Hauffe. **The stationary state of catalysts in homogeneous reactions**. *Elektrochem*, **33**:172, 1938. ix

[2] Walter H. Brattain and John Bardeen. **Surface Properties of Germanium**. *Bell System Technical Journal*, **32**(1):1–41, jan 1953. ix

[3] G. Heiland. **Zum Einfluß von Wasserstoff auf die elektrische Leitfähigkeit an der Oberfläche von Zinkoxydkristallen**. *Zeitschrift für Physik*, **148**(1):15–27, feb 1957. ix

[4] A BIELAŃSKI, J DEREŃ, and J HABER. **Electric Conductivity and Catalytic Activity of Semiconducting Oxide Catalysts**. *Nature*, **179**(4561):668–669, mar 1957. ix

[5] Tetsuro Seiyama, Akio Kato, Kiyoshi Fujiishi, and Masanori Nagatani. **A New Detector for Gaseous Components Using Semiconductive Thin Films.** *Analytical Chemistry*, **34**(11):1502–1503, oct 1962. ix

[6] N. Taguchi. **US3631436A**, 1971. ix

[7] Kumar Ganesan and Louis Theodore. **Air Pollution Control Engineering**. In *Handbook of Environmental Engineering*, pages 453–492. John Wiley & Sons, Inc., Hoboken, NJ, USA, aug 2018. ix

[8] R M HARRISON. **A FRESH LOOK AT AIR (VOL 30, PG 987, 1994)**. *CHEMISTRY IN BRITAIN*, **31**(2):131, feb 1995. ix

[9] EH40/96 Occupational Exposure Limits. *Health and Safety Executive*. HMSO, London, 1996. ix

[10] ACGIH. **Association Advancing Occupational and Environmental Health**. ix

[11] Giovanni Neri. **First Fifty Years of Chemoresistive Gas Sensors**. *Chemosensors*, **3**(1):1–20, jan 2015. x

[12] N BARSAN, D KOZIEJ, and U WEIMAR. **Metal oxide-based gas sensor research: How to?** *Sensors and Actuators B: Chemical*, **121**(1):18–35, jan 2007. x

[13] Noboru Yamazoe. **Toward innovations of gas sensor technology**. *Sensors and Actuators B: Chemical*, **108**(1-2):2–14, jul 2005. x

[14] G. B. SergeeV V. E. Bochenkov. *Sensitivity, Selectivity, and Stability of Gas-Sensitive Metal- Oxide Nanostructures. In Metal Oxide Nanostructures and Their Applications;*. American Scientific Publishers, 2010. x

[15] Hi Gyu Moon, Youngmo Jung, Soo Deok Han, Young-Seok Shim, Beomju Shin, Taikjin Lee, Jin-Sang Kim, Seok Lee, Seong Chan Jun, Hyung-Ho Park, Chulki Kim, and Chong-Yun Kang. **Chemiresistive Electronic Nose toward Detection of Biomarkers in Exhaled Breath**. *ACS Applied Materials & Interfaces*, **8**(32):20969–20976, aug 2016. x

[16] Estefanía Núñez Carmona, Veronica Sberveglieri, Andrea Ponzoni, Vardan Galstyan, Dario Zappa, Andrea Pulvirenti, and Elisabetta Comini. **Detection of food and skin pathogen microbiota by means of an electronic nose based on metal oxide chemiresistors**. *Sensors and Actuators B: Chemical*, **238**, 2016. x

[17] B. Fabbri, M. Valt, C. Parretta, S. Gherardi, A. Gaiardo, C. Malagù, F. Mantovani, V. Strati, and V. Guidi. **Correlation of Gaseous Emissions to Water Stress in Tomato and Maize Crops: from field to laboratory and back**. *Sensors and Actuators B: Chemical*, page 127227, oct 2019. x

[18] F. Hossein-Babaei and V. Ghafarinia. **Compensation for the drift-like terms caused by environmental fluctuations in the responses of chemoresistive gas sensors**. *Sensors and Actuators B: Chemical*, **143**(2):641–648, jan 2010. x

[19] G Korotcenkov and Beongki Cho. **Instability of metal oxide-based conductometric gas sensors and approaches to stability improvement, G. Korotcenkov, B.K. Cho, Sens. Actuators B 156 (2011) 527-538.** *Sensors and Actuators B Chemical*, **156**:527–538, 2011. x

[20] Isolde Simon, Nicolae Bârsan, Michael Bauer, and Udo Weimar. **Micromachined metal oxide gas sensors: opportunities to improve sensor performance**. *Sensors and Actuators B: Chemical*, **73**(1):1–26, feb 2001. x

[21] P. R. Wallace. **The Band Theory of Graphite**. *Physical Review*, **71**(9):622–634, may 1947. 1

[22] K. S. Novoselov. **Electric Field Effect in Atomically Thin Carbon Films**. *Science*, **306**(5696):666–669, oct 2004. 1

[23] Nathan O. Weiss, Hailong Zhou, Lei Liao, Yuan Liu, Shan Jiang, Yu Huang, and Xiangfeng Duan. **Graphene: An Emerging Electronic Material**. *Advanced Materials*, **24**(43):5782–5825, nov 2012. 1

[24] D.S.L. Abergel, V. Apalkov, J. Berashevich, K. Ziegler, and Tapash Chakraborty. **Properties of graphene: a theoretical perspective**. *Advances in Physics*, **59**(4):261–482, jul 2010. 1

[25] L. A. Ponomarenko, R. V. Gorbachev, G. L. Yu, D. C. Elias, R. Jalil, A. A. Patel, A. Mishchenko, A. S. Mayorov, C. R. Woods, J. R. Wallbank, M. Mucha-Kruczynski, B. A. Piot, M. Potemski, I. V. Grigorieva, K. S. Novoselov, F. Guinea, V. I. Fal'ko, and A. K. Geim. **Cloning of Dirac fermions in graphene superlattices**. *Nature*, **497**(7451):594–597, may 2013. 1

[26] Dattatray J. Late, Yi-Kai Huang, Bin Liu, Jagaran Acharya, Sharmila N. Shirodkar, Jiajun Luo, Aiming Yan, Daniel Charles, Umesh V. Waghmare, Vinayak P. Dravid, and C. N. R. Rao. **Sensing Behavior of Atomically Thin-Layered MoS 2 Transistors**. *ACS Nano*, **7**(6):4879–4891, jun 2013. 2

[27] V. Guidi, M.A. Butturi, M.C. Carotta, B. Cavicchi, M. Ferroni, C. Malagù, G. Martinelli, D. Vincenzi, M. Sacerdoti, and M. Zen. **Gas sensing through thick film technology**. *Sensors and Actuators B: Chemical*, **84**(1):72–77, apr 2002. 3, 47

[28] Alvise Bagolini, Andrea Gaiardo, Michele Crivellari, Evgeny Demenev, Ruben Bartali, Antonino Picciotto, Matteo Valt, Francesco Ficorella, Vincenzo Guidi, and Pierluigi Bellutti. **Development of MEMS MOS gas sensors with CMOS compatible PECVD inter-metal passivation**. *Sensors and Actuators, B: Chemical*, pages 225–232, 2019. 3

[29] Nicolae Barsan and Udo Weimar. **Conduction model of metal oxide gas sensors**. *Journal of Electroceramics*, **7**(3):143–167, 2001. 4

[30] Giselle Jiménez-Cadena, Jordi Riu, and F. Xavier Rius. **Gas sensors based on nanostructured materials**. *The Analyst*, **132**(11):1083, 2007. 4

[31] Hyo-Joong Kim and Jong-Heun Lee. **Highly sensitive and selective gas sensors using p-type oxide semiconductors: Overview**. *Sensors and Actuators B: Chemical*, **192**:607–627, mar 2014. 5

[32] Qu Yue, Zhengzheng Shao, Shengli Chang, and Jingbo Li. **Adsorption of gas molecules on monolayer MoS2 and effect of applied electric field**. *Nanoscale Research Letters*, **8**(1):425, 2013. 4

[33] G. Korotcenkov and B.K. Cho. **Engineering approaches for the improvement of conductometric gas sensor parameters**. *Sensors and Actuators B: Chemical*, **188**:709–728, nov 2013. 7

[34] Yong Zhou, Yadong Jiang, Tao Xie, Huiling Tai, and Guangzhong Xie. **A novel sensing mechanism for resistive gas sensors based on layered reduced graphene oxide thin films at room temperature**. *Sensors and Actuators B: Chemical*, **203**:135–142, nov 2014. 7

[35] Ziqi Sun, Ting Liao, Yuhai Dou, Soo Min Hwang, Min-Sik Park, Lei Jiang, Jung Ho Kim, and Shi Xue Dou. **Generalized self-assembly of scalable two-dimensional transition metal oxide nanosheets**. *Nature Communications*, **5**(1):3813, sep 2014. 8

[36] Chang Liu, Hongbing Lu, Jinniu Zhang, Zhibo Yang, Gangqiang Zhu, Feng Yin, Jianzhi Gao, Chujun Chen, and Xia Xin. **Abnormal p-type sensing response of TiO2 nanosheets with exposed {001} facets**. *Journal of Alloys and Compounds*, **705**:112–117, may 2017. 8

[37] Kin Fai Mak, Changgu Lee, James Hone, Jie Shan, and Tony F. Heinz. **Atomically thin MoS2: A new direct-gap semiconductor**. *Physical Review Letters*, **105**(13):136805, sep 2010. 10

[38] Yeon Hoo Kim, Kye Yeop Kim, You Rim Choi, Young-Seok Shim, Jong-Myeong Jeon, Jong-Heun Lee, Soo Young Kim, Seungwu Han, and Ho Won Jang. **Ultrasensitive reversible oxygen sensing by using liquid-exfoliated MoS 2 nanoparticles**. *Journal of Materials Chemistry A*, **4**(16):6070–6076, 2016. 10

[39] Priyanka Garg, Indrani Choudhuri, and Biswarup Pathak. **Stanene based gas sensors: effect of spin–orbit coupling**. *Physical Chemistry Chemical Physics*, **19**(46):31325–31334, 2017. 12

[40] Jian Zhen Ou, Wanyin Ge, Benjamin Carey, Torben Daeneke, Asaf Rotbart, Wei Shan, Yichao Wang, Zhengqian Fu, Adam F. Chrimes, Wojtek Wlodarski, Salvy P. Russo, Yong Xiang Li, and Kourosh Kalantar-zadeh. **Physisorption-Based Charge Transfer in Two-Dimensional SnS 2 for Selective and Reversible NO 2 Gas Sensing**. *ACS Nano*, **9**(10):10313–10323, oct 2015. 12, 13

[41] Radislav A. Potyrailo, Cheryl Surman, Nandini Nagraj, and Andrew Burns. **Materials and Transducers Toward Selective Wireless Gas Sensing**. *Chemical Reviews*, **111**(11):7315–7354, nov 2011. 12

[42] Priyanka Garg, Indrani Choudhuri, Arup Mahata, and Biswarup Pathak. **Band gap opening in stanene induced by patterned B–N doping**. *Physical Chemistry Chemical Physics*, **19**(5):3660–3669, 2017. 13

[43] Nanshu Liu and Si Zhou. **Gas adsorption on monolayer blue phosphorus: implications for environmental stability and gas sensors**. *Nanotechnology*, **28**(17):175708, apr 2017. 13

[44] F. Schedin, A. K. Geim, S. V. Morozov, E. W. Hill, P. Blake, M. I. Katsnelson, and K. S. Novoselov. **Detection of individual gas molecules adsorbed on graphene**. *Nature Materials*, **6**(9):652–655, sep 2007. 17

[45] Sukju Hwang, Juhwan Lim, Hyung Goo Park, Whan Kyun Kim, Duck-Hwan Kim, In Sang Song, Jae Hun Kim, Seok Lee, Deok Ha Woo, and Seong Chan Jun. **Chemical vapor sensing properties of graphene based on geometrical evaluation**. *Current Applied Physics*, **12**(4):1017–1022, jul 2012. 17

[46] Fazel Yavari, Eduardo Castillo, Hemtej Gullapalli, Pulickel M. Ajayan, and Nikhil Koratkar. **High sensitivity detection of NO 2 and NH 3 in air using chemical vapor deposition grown graphene**. *Applied Physics Letters*, **100**(20):203120, may 2012. 17

[47] A K Geim and K S Novoselov. **The rise of graphene**. *Nature Mater.*, **6**(3):183–191, 2007. 18

[48] S Basu and P Bhattacharyya. **Recent developments on graphene and graphene oxide based solid state gas sensors**. *Sensors and Actuators B: Chemical*, **173**:1–21, 2012. 18

[49] Seba S Varghese, Sunil Lonkar, K K Singh, Sundaram Swaminathan, and Ahmed Abdala. **Recent advances in graphene based gas sensors**. *Sensors and Actuators B: Chemical*, **218**:160–183, 2015. 18

[50] Lu Wang, Kyuho Lee, Yi Yang Sun, Michael Lucking, Zhongfang Chen, Ji Jun Zhao, and Shengbai B Zhang. **Graphene oxide as an ideal substrate for hydrogen storage**. *ACS Nano*, **3**(10):2995–3000, 2009. 18

[51] Catriona McCallion, John Burthem, Karen Rees-Unwin, Alexander Golovanov, and Alain Pluen. **Graphene in therapeutics delivery: Problems, solutions and future opportunities**. *European Journal of Pharmaceutics and Biopharmaceutics*, **104**:235–250, 2016. 18

[52] U R Farooqui, A L Ahmad, and N A Hamid. **Graphene oxide: A promising membrane material for fuel cells**. *Renewable and Sustainable Energy Reviews*, **82**(September 2017):714–733, 2018. 18

[53] Goki Eda, Arokia Nathan, Paul Wöbkenberg, Florian Colleaux, Khashayar Ghaffarzadeh, Thomas D Anthopoulos, and Manish Chhowalla. **Graphene oxide gate dielectric for graphene-based monolithic field effect transistors**. *Applied Physics Letters*, **102**(13):13–17, 2013. 18

[54] Rama K Layek and Arun K Nandi. **A review on synthesis and properties of polymer functionalized graphene**. *Polymer (United Kingdom)*, **54**(19):5087–5103, 2013. 18

[55] Kei Toda, Ryo Furue, and Shinya Hayami. **Recent progress in applications of graphene oxide for gas sensing: A review**. *Analytica Chimica Acta*, **878**:43–53, 2015. 18, 69

[56] Mohammad Razaul Karim, Kazuto Hatakeyama, Takeshi Matsui, Hiroshi Takehira, Takaaki Taniguchi, Michio Koinuma, Yasumichi Matsumoto, Tomoyuki Akutagawa, Takayoshi Nakamura, Shin Ichiro Noro, Teppei Yamada, Hiroshi Kitagawa, and Shinya Hayami. **Graphene oxide nanosheet with high proton conductivity**. *Journal of the American Chemical Society*, **135**(22):8097–8100, 2013. 18, 69

[57] Kazuto Hatakeyama, Mohammad Razaul Karim, Chikako Ogata, Hikaru Tateishi, Asami Funatsu, Takaaki Taniguchi, Michio Koinuma, Shinya Hayami, and Yasumichi Matsumoto. **Proton conductivities of graphene oxide nanosheets: Single, multilayer, and modified nanosheets**. *Angewandte Chemie - International Edition*, **53**(27):6997–7000, 2014. 18, 69

[58] Maurizio Donarelli, Stefano Prezioso, Francesco Perrozzi, Luca Giancaterini, Carlo Cantalini, Emanuele Treossi, Vincenzo Palermo, Sandro Santucci, and Luca Ottaviano. **Graphene oxide for gas detection under standard humidity conditions**. *2D Materials*, **2**(3):35018, 2015. 18, 69

[59] Daniel R Dreyer, Sungjin Park, Christopher W Bielawski, and Rodney S Ruoff. **The chemistry of graphene oxide**. *Chem. Soc. Rev.*, **39**(1):228–240, 2010. 18, 69

[60] Jeremy T. Robinson, F. Keith Perkins, Eric S. Snow, Zhongqing Wei, and Paul E. Sheehan. **Reduced Graphene Oxide Molecular Sensors**. *Nano Letters*, **8**(10):3137–3140, oct 2008. 19

[61] Ruma Ghosh, Anupam Midya, Sumita Santra, Samit K. Ray, and Prasanta K. Guha. **Chemically Reduced Graphene Oxide for Ammonia Detection at Room Temperature**. *ACS Applied Materials & Interfaces*, **5**(15):7599–7603, aug 2013. 19

[62] M. J. Fernández-Merino, L. Guardia, J. I. Paredes, S. Villar-Rodil, P. Solís-Fernández, A. Martínez-Alonso, and J. M. D. Tascón. **Vitamin C Is an Ideal Substitute for Hydrazine in the Reduction of Graphene Oxide Suspensions**. *The Journal of Physical Chemistry C*, **114**(14):6426–6432, apr 2010. 20

[63] Vineet Dua, Sumedh P. Surwade, Srikanth Ammu, Srikanth Rao Agnihotra, Sujit Jain, Kyle E. Roberts, Sungjin Park, Rodney S. Ruoff, and Sanjeev K. Manohar. **All-Organic Vapor Sensor Using Inkjet-Printed Reduced Graphene Oxide**. *Angewandte Chemie International Edition*, **49**(12):2154–2157, mar 2010. 20

[64] Wei Gao, Lawrence B Alemany, Lijie Ci, and Pulickel M Ajayan. **New insights into the structure and reduction of graphite oxide**. *Nature Chemistry*, **1**:403, jul 2009. 20

[65] Alexey Lipatov, Alexey Varezhnikov, Peter Wilson, Victor Sysoev, Andrei Kolmakov, and Alexander Sinitskii. **Highly selective gas sensor arrays based on thermally reduced graphene oxide**. *Nanoscale*, **5**(12):5426, 2013. 20

[66] Yu-Ming Lin and Phaedon Avouris. **Strong Suppression of Electrical Noise in Bilayer Graphene Nanodevices**. *Nano Letters*, **8**(8):2119–2125, aug 2008. 20

[67] Li Guo, Hao-Bo Jiang, Rui-Qiang Shao, Yong-Lai Zhang, Sheng-Yi Xie, Jian-Nan Wang, Xian-Bin Li, Fan Jiang, Qi-Dai Chen, Tong Zhang, and Hong-Bo Sun. **Two-beam-laser interference mediated reduction, patterning and nanostructuring of graphene oxide for the production of a flexible humidity sensing device**. *Carbon*, **50**(4):1667–1673, apr 2012. 20

[68] Anton Lerf, Heyong He, Michael Forster, and Jacek Klinowski. **Structure of Graphite Oxide Revisited**. *Journal of Physical Chemistry B*, **102**(23):4477–4482, 1998. 21, 58

[69] William R Collins, Ezequiel Schmois, and Timothy M Swager. **Graphene oxide as an electrophile for carbon nucleophiles.** *Chemical communications (Cambridge, England)*, **47**(31):8790–8792, 2011. 21, 58

[70] Ming Fang, Kaigang Wang, Hongbin Lu, Yuliang Yang, and Steven Nutt. **Covalent polymer functionalization of graphene nanosheets and mechanical properties of composites**. *Journal of Materials Chemistry*, **19**(38):7098, 2009. 21, 58

[71] Fei Xing, Shan Zhang, Yong Yang, Wenshuai Jiang, Zhibo Liu, Siwei Zhu, and Xiaocong Yuan. **Chemically modified graphene films for high-performance optical NO 2 sensors**. *The Analyst*, **141**(15):4725–4732, 2016. 21

[72] M Valt, B Fabbri, A Gaiardo, S Gherardi, D Casotti, G Cruciani, G Pepponi, L Vanzetti, E Iacob, C Malagù, P Bellutti, and V Guidi. **Aza-crown-ether functionalized graphene oxide for gas sensing and cation trapping applications**. *Materials Research Express*, **6**(7):075603, apr 2019. 21, 59, 60, 61, 62, 64, 65, 68, 70, 73, 96

[73] Seba Sara Varghese, Saino Hanna Varghese, Sundaram Swaminathan, Krishna Kumar Singh, and Vikas Mittal. **Two-dimensional materials for sensing: Graphene and beyond**. *Electronics (Switzerland)*, **4**(3):651–687, 2015. 21

[74] Wei Yang, Lin Gan, Huiqiao Li, and Tianyou Zhai. **Two-dimensional layered nanomaterials for gas-sensing applications**. *Inorganic Chemistry Frontiers*, **3**(4):433–451, 2016. 21

[75] B. Baranowski, F. A. Lewis, W. D. McFall, S. Filipek, and T. C. Witherspoon. **A Study of the Palladium-Platinum-Hydrogen System Over a Wide Range of Hydrogen Pressures**. *Proceedings of the Royal Society A: Mathematical, Physical and Engineering Sciences*, **386**(1791):309–332, apr 1983. 22

[76] M. Armbrüster, K. Kovnir, M. Friedrich, D. Teschner, G. Wowsnick, M. Hahne, P. Gille, L. Szentmiklósi, M. Feuerbacher, M. Heggen, F. Girgsdies, D. Rosenthal, R. Schlögl, and Yu. Grin. **Al13Fe4 as a low-cost alternative for palladium in heterogeneous hydrogenation**. *Nature Materials*, **11**(8):690–693, aug 2012. 22

[77] F. Schedin, A. K. Geim, S. V. Morozov, E. W. Hill, P. Blake, M. I. Katsnelson, and K. S. Novoselov. **Detection of individual gas molecules adsorbed on graphene**. *Nature Materials*, **6**(9):652–655, sep 2007. 22

[78] Sasha Stankovich, Dmitriy A. Dikin, Geoffrey H. B. Dommett, Kevin M. Kohlhaas, Eric J. Zimney, Eric A. Stach, Richard D. Piner, SonBinh T. Nguyen, and Rodney S. Ruoff. **Graphene-based composite materials**. *Nature*, **442**(7100):282–286, jul 2006. 22

[79] Duy-Thach Phan and Gwiy-Sang Chung. **Characteristics of resistivity-type hydrogen sensing based on palladium-graphene nanocomposites**. *International Journal of Hydrogen Energy*, **39**(1):620–629, jan 2014. 22

[80] Duy-Thach Phan and Gwiy-Sang Chung. **Effects of Pd nanocube size of Pd nanocube-graphene hybrid on hydrogen sensing properties**. *Sensors and Actuators B: Chemical*, **204**:437–444, dec 2014. 22

[81] Vinayan Bhagavathi Parambhath, Rupali Nagar, K. Sethupathi, and S. Ramaprabhu. **Investigation of Spillover Mechanism in Palladium Decorated Hydrogen Exfoliated Functionalized Graphene**. *The Journal of Physical Chemistry C*, **115**(31):15679–15685, aug 2011. 23

[82] Ovidiu Cretu, Arkady V. Krasheninnikov, Julio A. Rodríguez-Manzo, Litao Sun, Risto M. Nieminen, and Florian Banhart. **Migration and Localization of Metal Atoms on Strained Graphene**. *Physical Review Letters*, **105**(19):196102, nov 2010. 23

[83] XIAN QIN, QINGYUAN MENG, and YUAN PING FENG. **STRAIN EFFECTS ON ENHANCED HYDROGEN SULPHIDE DETECTION CAPABILITY OF Ag -DECORATED DEFECTIVE GRAPHENE: A FIRST-PRINCIPLES INVESTIGATION**. *Modern Physics Letters B*, **26**(25):1250166, oct 2012. 23

[84] Shumao Cui, Haihui Pu, Ganhua Lu, Zhenhai Wen, Eric C. Mattson, Carol Hirschmugl, Marija Gajdardziska-Josifovska, Michael Weinert, and Junhong Chen. **Fast and Selective Room-Temperature Ammonia Sensors Using Silver Nanocrystal-Functionalized Carbon Nanotubes**. *ACS Applied Materials & Interfaces*, **4**(9):4898–4904, sep 2012. 23

[85] M. Penza, G. Cassano, R. Rossi, M. Alvisi, A. Rizzo, M. A. Signore, Th. Dikonimos, E. Serra, and R. Giorgi. **Enhancement of sensitivity in gas chemiresistors based on carbon nanotube surface functionalized with noble metal (Au, Pt) nanoclusters**. *Applied Physics Letters*, **90**(17):173123, apr 2007. 23

[86] Michela Cittadini, Marco Bersani, Francesco Perrozzi, Luca Ottaviano, Wojtek Wlodarski, and Alessandro Martucci. **Graphene oxide coupled with gold nanoparticles for localized surface plasmon resonance based gas sensor**. *Carbon*, **69**:452–459, apr 2014. 23

[87] Sen Liu, Bo Yu, Hao Zhang, Teng Fei, and Tong Zhang. **Enhancing NO2 gas sensing performances at room temperature based on reduced graphene oxide-ZnO nanoparticles hybrids**. *Sensors and Actuators B: Chemical*, **202**:272–278, oct 2014. 24

[88] Hao Zhang, Jianchao Feng, Teng Fei, Sen Liu, and Tong Zhang. **SnO2 nanoparticles-reduced graphene oxide nanocomposites for NO2 sensing at low operating temperature**. *Sensors and Actuators B: Chemical*, **190**:472–478, jan 2014. 24

[89] Lisha Zhou, Fangping Shen, Xike Tian, Donghong Wang, Ting Zhang, and Wei Chen. **Stable Cu2O nanocrystals grown on functionalized graphene sheets and room temperature H2S gas sensing with ultrahigh sensitivity**. *Nanoscale*, **5**(4):1564, 2013. 24

[90] Wei Yang, Peng Wan, Xiaodong Zhou, Jiming Hu, Yafeng Guan, and Liang Feng. **Additive-Free Synthesis of In 2 O 3 Cubes Embedded into Graphene Sheets and Their Enhanced NO 2 Sensing Performance at Room Temperature**. *ACS Applied Materials & Interfaces*, **6**(23):21093–21100, dec 2014. 24

[91] Shipu Xu, Fengqiang Sun, Zizhao Pan, Chaowei Huang, Shumin Yang, Jinfeng Long, and Ying Chen. **Reduced Graphene Oxide-Based Ordered Macroporous Films on a Curved Surface: General Fabrication and Application in Gas Sensors**. *ACS Applied Materials & Interfaces*, **8**(5):3428–3437, feb 2016. 24

[92] Mark A. Andio, Paul N. Browning, Patricia A. Morris, and Sheikh A. Akbar. **Comparison of gas sensor performance of SnO2 nano-structures on microhotplate platforms**. *Sensors and Actuators B: Chemical*, **165**(1):13–18, apr 2012. 24

[93] A. Gaiardo, B. Fabbri, A. Giberti, V. Guidi, P. Bellutti, C. Malagù, M. Valt, G. Pepponi, S. Gherardi, G. Zonta, A. Martucci, M. Sturaro, and N. Landini. **ZnO and Au/ZnO thin films: Room-temperature chemoresistive properties for gas sensing applications**. *Sensors and Actuators B: Chemical*, **237**:1085–1094, dec 2016. 24, 51

[94] J Yu, S J Ippolito, W Wlodarski, M Strano, and K Kalantar-zadeh. **Nanorod based Schottky contact gas sensors in reversed bias condition**. *Nanotechnology*, **21**(26):265502, jul 2010. 24

[95] Kyoung Jin Choi and Ho Won Jang. **One-Dimensional Oxide Nanostructures as Gas-Sensing Materials: Review and Issues**. *Sensors*, **10**(4):4083–4099, apr 2010. 24

[96] Jiwon Lee, Dai Hong Kim, Seong-Hyeon Hong, and Jae Young Jho. **A hydrogen gas sensor employing vertically aligned TiO2 nanotube arrays prepared by template-assisted method**. *Sensors and Actuators B: Chemical*, **160**(1):1494–1498, dec 2011. 24

[97] D Rosenfeld, P.E Schmid, S Széles, F Lévy, V Demarne, and A Grisel. **Electrical transport properties of thin-film metal-oxide-metal Nb2O5 oxygen sensors**. *Sensors and Actuators B: Chemical*, **37**(1-2):83–89, nov 1996. 24

[98] L. Chambon, A. Pauly, J.P. Germain, C. Maleysson, V. Demarne, and A. Grisel. **A model for the responses of Nb2O5 sensors to CO and NH3 gases**. *Sensors and Actuators B: Chemical*, **43**(1-3):60–64, sep 1997. 24

[99] Zhao Wang, Yongming Hu, Wei Wang, Xiong Zhang, Baoxian Wang, Huyong Tian, Yu Wang, Jianguo Guan, and Haoshuang Gu. **Fast and highly-sensitive hydrogen sensing of Nb2O5 nanowires at room temperature**. *International Journal of Hydrogen Energy*, **37**(5):4526–4532, mar 2012. 24

[100] Xiudi Xiao, Guoping Dong, Cheng Xu, Hongbo He, Hongji Qi, Zhengxiu Fan, and Jianda Shao. **Structure and optical properties of Nb2O5 sculptured thin films by glancing angle deposition**. *Applied Surface Science*, **255**(5):2192–2195, dec 2008. 24

[101] Qing Hua Wang, Kourosh Kalantar-Zadeh, Andras Kis, Jonathan N Coleman, and Michael S Strano. **Electronics and optoelectronics of two-dimensional transition metal dichalcogenides**. *Nature Nanotechnology*, **7**:699, nov 2012. 24

[102] Kyung Yong Ko, Jeong-Gyu Song, Youngjun Kim, Taejin Choi, Sera Shin, Chang Wan Lee, Kyounghoon Lee, Jahyun Koo, Hoonkyung Lee, Jongbaeg Kim, Taeyoon Lee, Jusang Park, and Hyungjun Kim. **Improvement of Gas-Sensing Performance of Large-Area Tungsten Disulfide Nanosheets by Surface Functionalization**. *ACS Nano*, **10**(10):9287–9296, oct 2016. 25

[103] Byungjin Cho, Myung Gwan Hahm, Minseok Choi, Jongwon Yoon, Ah Ra Kim, Young-Joo Lee, Sung-Gyu Park, Jung-Dae Kwon, Chang Su Kim, Myungkwan Song, Yongsoo Jeong, Kee-Seok Nam, Sangchul Lee, Tae Jin Yoo, Chang Goo Kang, Byoung Hun Lee, Heung Cho Ko, Pulickel M. Ajayan, and Dong-Ho Kim. **Charge-transfer-based Gas Sensing Using Atomic-layer MoS2**. *Scientific Reports*, **5**(1):8052, jul 2015. 25

[104] Likai Li, Fangyuan Yang, Guo Jun Ye, Zuocheng Zhang, Zengwei Zhu, Wenkai Lou, Xiaoying Zhou, Liang Li, Kenji Watanabe, Takashi Taniguchi, Kai Chang, Yayu Wang, Xian Hui Chen, and Yuanbo Zhang. **Quantum Hall effect in black phosphorus two-dimensional electron system**. *Nature Nanotechnology*, **11**(7):593–597, jul 2016. 26

[105] S.J. Ray. **First-principles study of MoS2, phosphorene and graphene based single electron transistor for gas sensing applications**. *Sensors and Actuators B: Chemical*, **222**:492–498, jan 2016. 26

[106] Likai Li, Yijun Yu, Guo Jun Ye, Qingqin Ge, Xuedong Ou, Hua Wu, Donglai Feng, Xian Hui Chen, and Yuanbo Zhang. **Black phosphorus field-effect transistors**. *Nature Nanotechnology*, **9**:372, mar 2014. 26

[107] Chongyang Zhu, Feng Xu, Ling Zhang, Minli Li, Jing Chen, Shuhong Xu, Guangguang Huang, Wenhao Chen, and Litao Sun. **Ultrafast Preparation of Black Phosphorus Quantum Dots for Efficient Humidity Sensing**. *Chemistry - A European Journal*, **22**(22):7357–7362, may 2016. 26

[108] Manisha B. Erande, Mahendra S. Pawar, and Dattatray J. Late. **Humidity Sensing and Photodetection Behavior of Electrochemically Exfoliated Atomically Thin-Layered Black Phosphorus Nanosheets**. *ACS Applied Materials & Interfaces*, **8**(18):11548–11556, may 2016. 26

[109] Yongqing Cai, Qingqing Ke, Gang Zhang, and Yong-Wei Zhang. **Energetics, Charge Transfer, and Magnetism of Small Molecules Physisorbed on Phosphorene**. *The Journal of Physical Chemistry C*, **119**(6):3102–3110, feb 2015. 26

[110] Liangzhi Kou, Thomas Frauenheim, and Changfeng Chen. **Phosphorene as a Superior Gas Sensor: Selective Adsorption and Distinct I − V Response**. *The Journal of Physical Chemistry Letters*, **5**(15):2675–2681, aug 2014. 27, 28, 87

[111] Marianne Köpf, Yuqiang Ma, Tom Nilges, Sen Cong, Liang Chen, Chongwu Zhou, Ahmad N. Abbas, Noppadol Aroonyadet, and Bilu Liu. **Black Phosphorus Gas Sensors**. *ACS Nano*, **9**(5):5618–5624, 2015. 27, 84, 85

[112] M. Donarelli, L. Ottaviano, L. Giancaterini, G. Fioravanti, F. Perrozzi, and C. Cantalini. **Exfoliated black phosphorus gas sensing properties at room temperature**. *2D Materials*, **3**(2):025002, mar 2016. 28, 85, 88

[113] Rezvan Ghanbari, Rosa Safaiee, Mohammad H. Sheikhi, Mohammad M. Golshan, and Z. Karami Horastani. **Graphene Decorated with Silver Nanoparticles as a Low-Temperature Methane Gas Sensor**. *ACS Applied Materials & Interfaces*, **11**(24):21795–21806, jun 2019. 28

[114] Byungjin Cho, Jongwon Yoon, Myung Gwan Hahm, Dong-Ho Kim, Ah Ra Kim, Yung Ho Kahng, Sang-Won Park, Young-Joo Lee, Sung-Gyu Park, Jung-Dae Kwon, Chang Su Kim, Myungkwan Song, Yongsoo Jeong, Kee-Seok Nam, and Heung Cho Ko. **Graphene-based gas sensor: metal decoration effect and application to a flexible device**. *J. Mater. Chem. C*, **2**(27):5280–5285, 2014. 28

[115] Vardan Galstyan, Andrea Ponzoni, Iskandar Kholmanov, Marta M. Natile, Elisabetta Comini, Sherzod Nematov, and Giorgio Sberveglieri. **Investigation of Reduced Graphene Oxide and a Nb-Doped TiO 2 Nanotube Hybrid Structure To Improve the Gas-Sensing Response and Selectivity**. *ACS Sensors*, **4**(8):2094–2100, aug 2019. 28

[116] Gonzalo Abellán, Vicent Lloret, Udo Mundloch, Mario Marcia, Christian Neiss, Andreas Görling, Maria Varela, Frank Hauke, and Andreas Hirsch. **Noncovalent Functionalization of Black Phosphorus**. *Angewandte Chemie International Edition*, **55**(47):14557–14562, nov 2016. 28

[117] Yiren Wang, Anh Pham, Sean Li, and Jiabao Yi. **Electronic and Magnetic Properties of Transition-Metal-Doped Monolayer Black Phosphorus by Defect Engineering**. *The Journal of Physical Chemistry C*, **120**(18):9773–9779, may 2016. 28

[118] Du Xiang, Cheng Han, Jing Wu, Shu Zhong, Yiyang Liu, Jiadan Lin, Xue-Ao Zhang, Wen Ping Hu, Barbaros Özyilmaz, A. H. Castro Neto, Andrew Thye Shen Wee, and Wei Chen. **Surface transfer doping induced effective modulation on ambipolar characteristics of few-layer black phosphorus**. *Nature Communications*, **6**(1):6485, dec 2015. 28, 77

[119] Soo-Yeon Cho, Hyeong-Jun Koh, Hae-Wook Yoo, and Hee-Tae Jung. **Tunable Chemical Sensing Performance of Black Phosphorus by Controlled Functionalization with Noble Metals**. *Chemistry of Materials*, **29**(17):7197–7205, sep 2017. 28, 77, 88

[120] Guanghui Li, Xuewen Wang, Haiyan Ding, and Ting Zhang. **A facile synthesis method for Ni(OH)2 ultrathin nanosheets and their conversion to porous NiO nanosheets used for formaldehyde sensing**. *RSC Advances*, **2**(33):13018, 2012. 28, 77

[121] Hyun Uk Lee, Soon Chang Lee, Jonghan Won, Byung-Chul Son, Saehae Choi, Yooseok Kim, So Young Park, Hee-Sik Kim, Young-Chul Lee, and Jouhahn Lee. **Stable semiconductor black phosphorus (BP)@titanium dioxide (TiO2) hybrid photocatalysts**. *Scientific Reports*, **5**(1):8691, aug 2015. 28

[122] Fabio Brigidi and Giancarlo Pepponi. **GIMPy: a software for the simulation of X-ray fluorescence and reflectivity of layered materials**. *X-Ray Spectrometry*, **46**(2):116–122, 2017. 45

[123] Barbara Fabbri, Lucia Bonoldi, Vincenzo Guidi, Giuseppe Cruciani, Davide Casotti, Cesare Malagù, Giuseppe Bellussi, Roberto Millini, Luciano Montanari, Angela Carati, Caterina Rizzo, Erica Montanari, and Stefano Zanardi. **Crystalline Microporous Organosilicates with Reversed Functionalities of Organic and Inorganic Components for Room-Temperature Gas Sensing**. *ACS Applied Materials & Interfaces*, **9**(29):24812–24820, jul 2017. 50

[124] Huafeng Yang, Changsheng Shan, Fenghua Li, Dongxue Han, Qixian Zhang, and Li Niu. **Covalent functionalization of polydisperse chemically-converted graphene sheets with amine-terminated ionic liquid**. *Chemical Communications*, (26):3880, 2009. 58

[125] R Ballesteros-Garrido, M de Miguel, A Domenech-Carbo, M Alvaro, and H Garcia. **Tunability by alkali metal cations of photoinduced charge separation in azacrown functionalized graphene**. *Chem Commun (Camb)*, **49**(31):3236–3238, 2013. 58, 66, 67

[126] M Praveen Kumar, T Kesavan, Golap Kalita, P Ragupathy, Tharangattu N Narayanan, and Deepak K Pattanayak. **On the large capacitance of nitrogen doped graphene derived by a facile route**. *RSC Adv.*, **4**(73):38689–38697, 2014. 63

[127] Margarita Herrera-Alonso, Ahmed A Abdala, Michael J McAllister, Ilhan A Aksay, and Robert K Prud'homme. **Intercalation and stitching of graphite oxide with diaminoalkanes**. *Langmuir*, **23**(21):10644–10649, 2007. 63

[128] Abhisek Gupta, Bikash Kumar Shaw, and Shyamal Kumar Saha. **Photoluminescence study of optically active diaminopyridine intercalated graphene oxide**. *RSC Adv.*, **4**(92):50542–50548, 2014. 63, 66

[129] Moutusi Banerjee, Abhisek Gupta, Shyamal K Saha, and Dipankar Chakravorty. **1-Aza-15-crown-5 functionalized graphene oxide for 2D graphene-based Li+-ion conductor**. *Small*, pages 1–7, 2015. 63, 65

[130] H W Siesler. **Vibrational Spectroscopy**. In *Polymer Science: A Comprehensive Reference, 10 Volume Set*, **2**, pages 255–300. John Wiley & Sons, Ltd, Chichester, UK, 2012. 63

[131] Gunnar Olsen, Jens Ulstrup, and Qijin Chi. **Crown-Ether Derived Graphene Hybrid Composite for Membrane-Free Potentiometric Sensing of Alkali Metal Ions**. *ACS Applied Materials & Interfaces*, **8**(1):37–41, 2016. 66, 95

[132] Yao Yao, Xiangdong Chen, Huihui Guo, Zuquan Wu, and Xiaoyu Li. **Humidity sensing behaviors of graphene oxide-silicon bi-layer flexible structure**. *Sensors and Actuators, B: Chemical*, **161**(1):1053–1058, 2012. 71

[133] S M Balashov, O V Balachova, A P Filho, M C Q Bazetto, and M G de Almeida. **Surface Acoustic Wave Humidity Sensors Based on Graphene Oxide Thin Films Deposited with the Surface Acoustic Wave Atomizer**. *ECS Transactions*, **49**(1):445–450, 2012. 71

[134] Dongzhi Zhang, Jun Tong, and Bokai Xia. **Humidity-sensing properties of chemically reduced graphene oxide/polymer nanocomposite film sensor based on layer-by-layer nano self-assembly**. *Sensors and Actuators, B: Chemical*, **197**:66–72, 2014. 71

[135] V Alvin Shubert, Christian W Müller, and Timothy S Zwier. **Water's role in reshaping a macrocycle's binding pocket: infrared and ultraviolet spectroscopy of benzo-15-crown-5-(H(2)O)(n) and 4'-aminobenzo-15-crown-5-(H(2)O)(n), n = 1, 2.** *The journal of physical chemistry. A*, **113**(28):8067–8079, 2009. 72

[136] Noam Agmon. **The Grotthuss mechanism**. *Chemical Physics Letters*, **50**(October), 1995. 72

[137] Hasmukh A Patel, John Selberg, Dhafer Salah, Haoyuan Chen, Yijun Liao, Siva Krishna, Mohan Nalluri, Omar K Farha, Randall Q Snurr, Marco Rolandi, and J Fraser Stoddart. **Proton Conduction in Tröger's Base-Linked Poly(crown ether)s**. *ACS Applied Materials & Interfaces*, **10**:25303–25310, 2018. 72

[138] Vadym V. Kulish, Oleksandr I. Malyi, Clas Persson, and Ping Wu. **Adsorption of metal adatoms on single-layer phosphorene.** *Physical chemistry chemical physics : PCCP*, **17**(2):992–1000, jan 2015. 77

[139] Arqum Hashmi and Jisang Hong. **Transition Metal Doped Phosphorene: First-Principles Study**. *The Journal of Physical Chemistry C*, **119**(17):9198–9204, apr 2015. 77

[140] Yu Jing, Xu Zhang, and Zhen Zhou. **Phosphorene: what can we know from computations?** *Wiley Interdisciplinary Reviews: Computational Molecular Science*, **6**(1):5–19, jan 2016. 77

[141] L. Seixas, A. Carvalho, and A. H. Castro Neto. **Atomically thin dilute magnetism in Co-doped phosphorene**. *Physical Review B*, **91**(15):155138, apr 2015. 77

[142] Fucai Liu, Chao Zhu, Lu You, Shi-Jun Liang, Shoujun Zheng, Jiadong Zhou, Qundong Fu, Yongmin He, Qingsheng Zeng, Hong Jin Fan, Lay Kee Ang, Junling Wang, and Zheng Liu. **2D Black Phosphorus/SrTiO 3 - Based Programmable Photoconductive Switch**. *Advanced Materials*, **28**(35):7768–7773, sep 2016. 77

[143] Hubert Valencia, Adrià Gil, and Gilles Frapper. **Trends in the Adsorption of 3d Transition Metal Atoms onto Graphene and Nanotube Surfaces: A DFT Study and Molecular Orbital Analysis**. *The Journal of Physical Chemistry C*, **114**(33):14141–14153, aug 2010. 77

[144] Zhidong Lin, Na Li, Zhe Chen, and Ping Fu. **The effect of Ni doping concentration on the gas sensing properties of Ni doped SnO2**. *Sensors and Actuators, B: Chemical*, **239**:501–510, 2017. 77

[145] Meng Bao, Yujiao Chen, Fang Li, Jianmin Ma, Ting Lv, Yunjing Tang, Libao Chen, Zhi Xu, and Taihong Wang. **Plate-like p–n heterogeneous NiO/WO3 nanocomposites for high performance room temperature NO2 sensors**. *Nanoscale*, **6**(8):4063, 2014. 77

[146] Ying Yang, Hongjie Wang, Linlin Wang, Yunlong Ge, Kan Kan, Keying Shi, and Junhong Chen. **A novel gas sensor based on porous α-Ni(OH)2 ultrathin nanosheet/reduced graphene oxide composites for room temperature detection of NO:X**. *New Journal of Chemistry*, **40**(5):4678–4686, 2016. 77

[147] Marianne Köpf, Nadine Eckstein, Daniela Pfister, Carolin Grotz, Ilona Krüger, Magnus Greiwe, Thomas Hansen, Holger Kohlmann, and Tom Nilges. **Access and in situ growth of phosphorene-precursor black phosphorus**. *Journal of Crystal Growth*, **405**:6–10, 2014. 78

[148] Maria Caporali, Manuel Serrano-Ruiz, Francesca Telesio, Stefan Heun, Giuseppe Nicotra, Corrado Spinella, and Maurizio Peruzzini. **Decoration of exfoliated black phosphorus with nickel nanoparticles and its application in catalysis**. *Chemical Communications*, **53**(79):10946–10949, 2017. 80, 81, 83

[149] Christopher R. Ryder, Joshua D. Wood, Spencer A. Wells, Yang Yang, Deep Jariwala, Tobin J. Marks, George C. Schatz, and Mark C. Hersam. **Covalent functionalization and passivation of exfoliated black phosphorus via aryl diazonium chemistry**. *Nature Chemistry*, **8**(6):597–602, jun 2016. 79

[150] Sijie Liu, Nengjie Huo, Sheng Gan, Yan Li, Zhongming Wei, Beiju Huang, Jian Liu, Jingbo Li, and Hongda Chen. **Thickness-dependent Raman spectra, transport properties and infrared photoresponse of few-layer black phosphorus**. *Journal of Materials Chemistry C*, **3**(42):10974–10980, 2015. 80

[151] Ganhua Lu, Leonidas E Ocola, and Junhong Chen. **Reduced graphene oxide for room-temperature gas sensors**. *Nanotechnology*, **20**(44):445502, nov 2009. 84

[152] Damien Hanlon, Claudia Backes, Evie Doherty, Clotilde S. Cucinotta, Nina C. Berner, Conor Boland, Kangho Lee, Andrew Harvey, Peter Lynch, Zahra Gholamvand, Saifeng Zhang, Kangpeng Wang, Glenn Moynihan, Anuj Pokle, Quentin M. Ramasse, Niall McEvoy, Werner J. Blau, Jun Wang, Gonzalo Abellan, Frank Hauke, Andreas Hirsch, Stefano Sanvito, David D. O'Regan, Georg S. Duesberg, Valeria Nicolosi, and Jonathan N. Coleman. **Liquid exfoliation of solvent-stabilized few-layer black phosphorus for applications beyond electronics**. *Nature Communications*, **6**(1):8563, dec 2015. 85

[153] Joshua D. Wood, Spencer A. Wells, Deep Jariwala, Kan-Sheng Chen, EunKyung Cho, Vinod K. Sangwan, Xiaolong Liu, Lincoln J. Lauhon, Tobin J. Marks, and Mark C. Hersam. **Effective Passivation of Exfoliated Black Phosphorus Transistors against Ambient Degradation**. *Nano Letters*, **14**(12):6964–6970, dec 2014. 85, 86

[154] R. R. Nair, H. A. Wu, P. N. Jayaram, I. V. Grigorieva, and A. K. Geim. **Unimpeded Permeation of Water Through Helium-Leak-Tight Graphene-Based Membranes**. *Science*, **335**(6067):442–444, jan 2012. 88, 95

[155] Guixia Zhao, Jiaxing Li, Xuemei Ren, Changlun Chen, and Xiangke Wang. **Few-layered graphene oxide nanosheets as superior sorbents for heavy metal ion pollution management**. *Environmental Science and Technology*, **45**(24):10454–10462, 2011. 95, 97

[156] Yi You, Veena Sahajwalla, Masamichi Yoshimura, and Rakesh K Joshi. **Graphene and graphene oxide for desalination**. *Nanoscale*, **8**(1):117–119, 2016. 95

[157] O Leenaerts, B Partoens, and F M Peeters. **Adsorption of H2 O, N H3, CO, N O2, and NO on graphene: A first-principles study**. *Physical Review B - Condensed Matter and Materials Physics*, **77**(12):125416, mar 2008. 95

[158] F De Jong and D N Reinhoudt. **Stability and Reactivity of Crown-Ether Complexes**. In *Advances in Physical Organic Chemistry*, **17**, pages 279–433. Academic Press, 1980. 95, 98

[159] Frank C J M van Veggel, Willem Verboom, and David N Reinhoudt. **Metallomacrocycles: Supramolecular Chemistry with Hard and Soft Metal Cations in Action**. *Chemical Reviews*, **94**(2):279–299, mar 1994. 95

[160] George W Gokel, W Matthew Leevy, and Michelle E Weber. **Crown ethers: Sensors for ions and molecular scaffolds for materials and biological models**. *Chemical Reviews*, **104**(5):2723–2750, 2004. 95

[161] Jerald S Bradshaw, Krzysztof E Krakowiak, and Reed M Izatt. *Aza Crown Macrocycles*. Chemistry of Heterocyclic Compounds: A Series Of Monographs. John Wiley & Sons, Inc., Hoboken, NJ, USA, 1993. 98

[162] Ralph G Pearson. **Hard and Soft Acids and Bases**. *Journal of the American Chemical Society*, **85**(22):3533–3539, nov 1963. 98

[163] L a Berrueta, B Gallo, and F Vicente. **A review of solid phase extraction: Basic principles and new developments**. *Chromatographia*, **40**(7-8):474–483, apr 1995. 98

[164] Beata Zawisza, Rafal Sitko, Ewa Malicka, and Ewa Talik. **Graphene oxide as a solid sorbent for the preconcentration of cobalt, nickel, copper, zinc and lead prior to determination by energy-dispersive X-ray fluorescence spectrometry**. *Analytical Methods*, **5**(22):6425, 2013. 99

[165] Beata Zawisza, Anna Baranik, Ewa Malicka, Ewa Talik, and Rafał Sitko. **Preconcentration of Fe(III), Co(II), Ni(II), Cu(II), Zn(II) and Pb(II) with ethylenediamine-modified graphene oxide**. *Microchimica Acta*, **183**(1):231–240, 2016. 99

[166] Katarzyna Pytlakowska, Violetta Kozik, Marek Matussek, Michał Pilch, Barbara Hachuła, and Karina Kocot. **Glycine modified graphene oxide as a novel sorbent for preconcentration of chromium, copper, and zinc ions from water samples prior to energy dispersive X-ray fluorescence spectrometric determination**. *RSC Adv.*, **6**(49):42836–42844, 2016. 99

Il tuo indirizzo e-mail

vltmtt1@unife.it

Oggetto:

Dichiarazione di conformità della tesi di Dottorato

Io sottoscritto Dott. (Cognome e Nome)

Valt Matteo

Nato a:

Agordo

Provincia:

Belluno

Il giorno:

4 Marzo 1989

Avendo frequentato il Dottorato di Ricerca in:

Fisica

Ciclo di Dottorato

32

Titolo della tesi:

2D materials for room-temperature chemoresistive gas sensing

Titolo della tesi (traduzione):

Materiali bidimensionali per la sensoristica chemoresistiva gassosa a temperatura ambiente

Tutore: Prof. (Cognome e Nome)

Guidi Vincenzo

Settore Scientifico Disciplinare (S.S.D.)

FIS/01

Parole chiave della tesi (max 10):

Chemoresistive gas sensing, 2D materials, room-temperature

Consapevole, dichiara

CONSAPEVOLE: (1) del fatto che in caso di dichiarazioni mendaci, oltre alle sanzioni previste dal codice penale e dalle Leggi speciali per l'ipotesi di falsità in atti ed uso di atti falsi, decade fin dall'inizio e senza necessità di alcuna formalità dai benefici conseguenti al provvedimento emanato sulla base di tali dichiarazioni; (2) dell'obbligo per l'Università di provvedere al deposito di legge delle tesi di dottorato al fine di assicurarne la conservazione e la consultabilità da parte di terzi; (3) della procedura adottata dall'Università di Ferrara ove si richiede che la tesi sia consegnata dal dottorando in 2 copie di cui una in formato cartaceo e una in formato pdf non modificabile su idonei supporti (CD-ROM, DVD) secondo le istruzioni pubblicate sul sito: http://www.unife.it/studenti/dottorato alla voce ESAME FINALE – disposizioni e modulistica; (4) del fatto che l'Università, sulla base dei dati forniti, archivierà e renderà consultabile in rete il testo completo della tesi di dottorato di cui alla presente dichiarazione attraverso l'Archivio istituzionale ad accesso aperto "EPRINTS.unife.it" oltre che attraverso i Cataloghi delle Biblioteche Nazionali Centrali di Roma e Firenze; DICHIARO SOTTO LA MIA RESPONSABILITA': (1) che

la copia della tesi depositata presso l'Università di Ferrara in formato cartaceo è del tutto identica a quella presentata in formato elettronico (CD-ROM, DVD), a quelle da inviare ai Commissari di esame finale e alla copia che produrrò in seduta d'esame finale. Di conseguenza va esclusa qualsiasi responsabilità dell'Ateneo stesso per quanto riguarda eventuali errori, imprecisioni o omissioni nei contenuti della tesi; (2) di prendere atto che la tesi in formato cartaceo è l'unica alla quale farà riferimento l'Università per rilasciare, a mia richiesta, la dichiarazione di conformità di eventuali copie; (3) che il contenuto e l'organizzazione della tesi è opera originale da me realizzata e non compromette in alcun modo i diritti di terzi, ivi compresi quelli relativi alla sicurezza dei dati personali; che pertanto l'Università è in ogni caso esente da responsabilità di qualsivoglia natura civile, amministrativa o penale e sarà da me tenuta indenne da qualsiasi richiesta o rivendicazione da parte di terzi; (4) che la tesi di dottorato non è il risultato di attività rientranti nella normativa sulla proprietà industriale, non è stata prodotta nell'ambito di progetti finanziati da soggetti pubblici o privati con vincoli alla divulgazione dei risultati, non è oggetto di eventuali registrazioni di tipo brevettale o di tutela. PER ACCETTAZIONE DI QUANTO SOPRA RIPORTATO

Firma del dottorando

Ferrara, li 19/02/2020 (data) Firma del Dottorando Matteo Volt

Firma del Tutore

Visto: Il Tutore Si approva Firma del Tutore Vincenzo Guidi